Theory of Disperse Diblock Copolymers

THEORY OF DISPERSE DIBLOCK COPOLYMERS

BY

CHI TO LAI, B.Sc., M.Sc.

A THESIS
SUBMITTED TO THE DEPARTMENT OF PHYSICS & ASTRONOMY
AND THE SCHOOL OF GRADUATE STUDIES
OF MCMASTER UNIVERSITY
IN PARTIAL FULFILMENT OF THE REQUIREMENTS
FOR THE DEGREE OF
DOCTORATE OF SCIENCE

Doctorate of Science (2022) McMaster University
(Physics & Astronomy) Hamilton, Ontario, Canada

TITLE: Theory of Disperse Diblock Copolymers

AUTHOR: Chi To Lai
B.Sc., (Mathematics and Physics Honours)
McGill University, Montreal, Canada
M.Sc., (Physics and Astronomy)
McMaster University, Hamilton, Canada

SUPERVISOR: Prof. An-Chang Shi

NUMBER OF PAGES: xx, 130

Abstract

The equilibrium phase behavior of disperse diblock copolymers is studied using the self-consistent field theory. We first examine how dispersity affects the formation of complex spherical phases in conformationally asymmetric diblock copolymers. For disperse diblock copolymers with Poisson and Schulz-Zimm distributions, the Frank-Kasper σ phase appears at a lower degree of conformational asymmetry than what is predicted in monodisperse systems. We next present a general method of treating molecular weight distributions (MWDs) specified by a set of molecular weight fractions in numerical self-consistent field theory. The procedure is applied to MWDs with similar dispersity indices and different skewness obtained from experimental measurements. We find that consistent with experiments, the domain spacing and equilibrium morphology could vary with the skewness. Lastly, we investigate how the MWD shape characterized by the dispersity index and skewness affects the relative stability of complex spherical phases. The predicted set of complex phases could differ between MWDs with identical dispersity indices and different skewness. In particular, it is found that the formation of the C14 and C15 phases is favored for more positively-skewed distributions. Overall, the work underlines the importance of the MWD shape on the phase behavior of disperse diblock copolymers and the need of considering other statistical measures alongside the dispersity index, such as the

skewness.

Acknowledgements

I am very grateful to Prof. An-Chang Shi for being an extremely patient and supportive supervisor who provided guidance and encouragement whenever it was necessary. Under his supervision, I had numerous opportunities to travel aboard for conferences and international exchanges, which was invaluable both on an academic and personal growth. Many thanks to also Prof. Weihua Li for allowing me to visit his group at Fudan University in Shanghai, China during the summer of 2019. My brief stay at Beihang University in Beijing, China would not have been possible without the help of Prof. Jiajia Zhou as well. Furthermore, I would like to thank the members serving on my supervisory committee, Prof. Kari Dalnoki-Veress, Prof. Paul Higgs and Prof. Sung-Sik Lee.

I cannot express how thankful I am to my parents, Lai Kwok Dick and Mok Kwai Fong, for always being supportive of my choices and decisions. Additionally, I greatly appreciate the help from friends and colleagues, in particular Jiayu Xie and Yicheng Qiang. Lastly, the numerical calculations for the majority of the work would not have been possible if not for the computational resources offered by SHARCNET.

Notation and abbreviations

We present below the definitions of all notation and abbreviations used in the main body of the thesis.

DIS	disordered
LAM	lamellar
HEX	hexagonally-packed cylindrical
DGY	double gyroid
BCC	body-centered cubic
$\mathrm{S_{cp}}$	hexagonally close-packed spherical
RPA	random phase approximation
SST	strong segregation theory
UCA	unit-cell approximation
SZ	Schulz-Zimm
FK	Frank-Kasper
SCFT	self-consistent field theory
PI-PLA	poly(isoprene)-*b*-poly[(±)-lactide]
c	index for polymer chain type
α	index for monomer type
f	average volume fraction of A-monomers
χ	Flory-Huggins parameter
N	degree of polymerization or chain contour length
V	system volume
b	Kuhn or statistical segment length
$\mathcal{Z}$	partition function
n_c	number of type-c polymer chains

k_B	Boltzmann constant
T	temperature
β	k_BT
λ_{T}	thermal de Broglie wavelength
$\boldsymbol{R}(s)$	space curve describing chain configuration
$\hat{\phi}(\boldsymbol{r})$	monomer volume fraction operator
v_α	single α-monomer volume
v_0	reference volume
H	Hamiltonian
$\delta(x)$	Dirac delta function
I_α	bounds of integration over contour length of α-block
$\mathcal{P}$	Wiener measure
F	mean-field free energy
$\phi_\alpha(\boldsymbol{r})$	spatially-varying α-monomer volume fraction
$\omega_\alpha(\boldsymbol{r})$	auxiliary field of α-monomers
$\xi(\boldsymbol{r})$	Lagrange multipler field for incompressibility condition
Z_c	single-chain partition of type-c polymers
Q_c	normalized single-chain partition of type-c polymers
$q_c(\boldsymbol{r}, s)$, $q_c^\dagger(\boldsymbol{r}, s)$	forward and backward end-integrated propagators
$\bar{\phi}_c$	average volume fraction of type-c polymers
P_c	number fraction or probability of type-c polymers
v_c	single-chain volume of type-c polymers
$\langle x_c \rangle$	number-averged value of x_c
$\boldsymbol{\theta}$	vector of unit-cell lattice parameters
z^*	complex conjugate of z
$\boldsymbol{G}_{hkl}$	reciprocal lattice vector, $h\boldsymbol{b}_1(\boldsymbol{\theta}) + k\boldsymbol{b}_2(\boldsymbol{\theta}) + l\boldsymbol{b}_3(\boldsymbol{\theta})$
$\{\boldsymbol{b}_1(\boldsymbol{\theta}), \boldsymbol{b}_2(\boldsymbol{\theta}), \boldsymbol{b}_3(\boldsymbol{\theta})\}$	set of primitive wavevectors
$\widehat{f}(\boldsymbol{k})$	Fourier transform of $f(\boldsymbol{r})$
G	mean-field grand canonical free energy
μ_c	chemical potential of type-c polymers
z_c	activity of type-c polymers

$u_{\mathrm{fr}}\left(\lvert\boldsymbol{r}\rvert\right)$	finite-range interaction between unlike monomers
σ_{fr}	range of finite-range interaction
$g(\lvert\boldsymbol{r}\rvert; b)$	bonded potential for freely jointed chains
λ_c	relative chain length $N_c/\langle N_c\rangle$
$\mathrm{Pois}\left(\lambda_c; \mu\right)$	Poisson distribution with mean of μ
$\mathrm{SZ}\left(\lambda_c; k\right)$	SZ distribution with shape parameter k
$Đ(N_c)$	dispersity index
ε	conformational asymmetry parameter
w_c	mass fraction of type-c polymers
m_c	moles of type-c polymers
M_c	molecular mass of type-c polymers
L	domain spacing in an ordered structure
CDF_α	cumulative distribution function for α-block lengths
R_0	$\sqrt{\langle N_{\mathrm{A},c}\rangle b_{\mathrm{A}}^2 + \langle N_{\mathrm{B},c}\rangle b_{\mathrm{B}}^2}$
$\widetilde{\mu}_3$	skewness
$\phi_{j,c}(\boldsymbol{r})$	distribution of chain junctions
$\Phi_{\alpha,c}\left(\boldsymbol{r}\right)$	single α-monomer volume

Below, the notation and abbreviations found in the appendices of the thesis is defined.

Φ_{A}	assumed average A-volume fraction
d_α	deviation function or residual for auxiliary field $\omega_\alpha(\boldsymbol{r})$
$d\left(\theta_p\right)$	deviation function or residual for lattice parameter θ_p
$\Delta\omega_\alpha$	total deviation or residue for the auxiliary fields
$\Delta\theta_p$	total deviation or residue for the lattice parameters
M_λ	number of points in the coarse-graining procedure for the Poisson distribution

Contents

List of Figures

Chapter 1

Introduction

Polymers are chain-like macromolecules composed of many repeat units, or monomers, covalently linked together. When the monomers are all identical, the product is referred to as a homopolymer. A block copolymer is produced by joining two or more chemically distinct homopolymers together. In a mixture of different types of homopolymers, the chemical incompatibility between unlike monomers drives phase separation of the system on a macroscopic scale (see left side of Figure 1.1). For block copolymers, chemical incompatibility again promotes separation. However, molecular connectivity permits the separation to occur only on a length scale determined by to the size of the polymers, typically in the range of 10 to 100 nanometers [5]. Consequently, block copolymers are frustrated at the molecular level due to the inability to optimize the two competing factors simultaneously. The molecular frustration leads to the self-assembly of block copolymers, where the incompatible blocks segregate into different domains. Packing of the self-assembled polymeric domains results in the formation of ordered structures [6, 7, 8].

The simplest example of block copolymers is the linear AB-diblock copolymer where one end of an A-homopolymer or A-block is connected to the end of a B-block. The equilibrium phase behavior of diblock copolymers is mainly regulated by two parameters [6, 7]. The first is the relative length or volume fraction of one of the two blocks f. The second is the segregation strength, which is specified by the product χN. Here, χ refers to the Flory-Huggins parameter, and N is the degree of polymerization (or polymer chain length). Since the primary driving force for phase separation is the chemical incompatibility, self-assembly only occurs when the segregation strength is sufficiently strong. At lower values of χN, the tendency to phase separate is weak, and the melt is in a disordered state. Only when χN becomes large enough will ordered structures spontaneously appear. Starting from a symmetric block composition ($f = 0.5$), the structural motif of the equilibrium morphology is planar or lamellar, proceeding to cylindrical and lastly to spherical micelles as the block lengths become increasingly asymmetric [9] (see Figure 1.1). For the latter two, the core and corona are composed of the minority and majority blocks, respectively.

Qualitatively, the self-assembled morphology of block copolymers is determined by two factors, the A/B interfacial tension and the entropic chain-stretching energy. The more a polymer is extended, the fewer accessible chain configurations, leading to a decrease in entropy. The most common model for chain connectivity treats polymer chains as ideal Hookean springs connected in series [6, 5, 7]. The optimal arrangement of symmetric diblock copolymers ($f = 0.5$) is to pack along a flat interface. However, packing in the same fashion for the asymmetric counterparts will stretch the majority block more than the minority. As the asymmetry in block lengths grow, structures with greater interfacial curvature towards the minority component are preferred. Doing so relaxes the stretching of the majority blocks, which offsets the accompanying

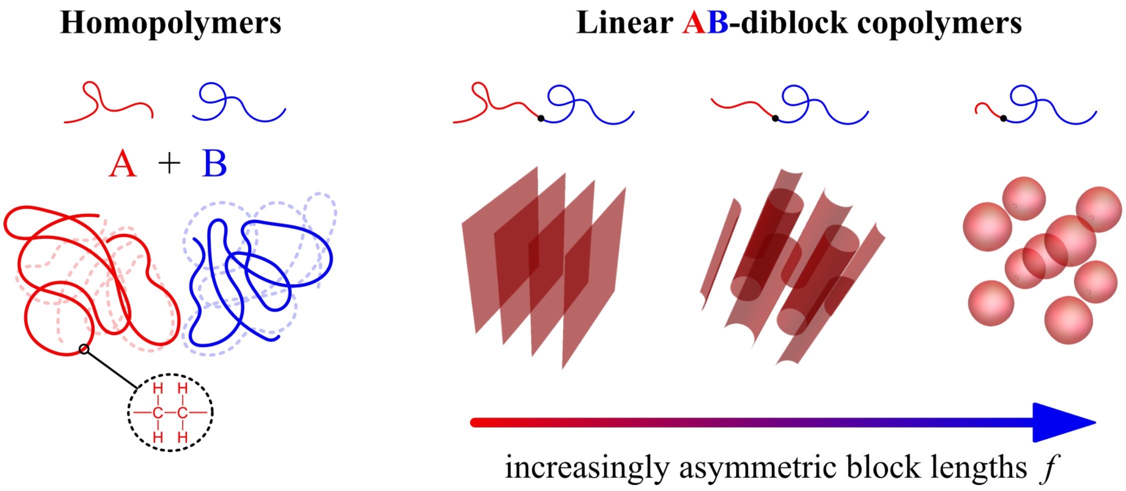

Figure 1.1: Schematic depicting on the left a phase-separated mixture of A- and B-homopolymers. On the right, the general progression of the equilibrium morphology in linear AB-diblock copolymers is illustrated. For clarity, only the surface dividing the A- and B-rich domains is shown for the three structures on the right.

cost of extending the minority blocks to a higher degree. This explains the general progression of equilibrium phases. The space-filling periodic arrangement of the cylinders and spheres are further determined by the competition of two opposing factors, commonly referred to as packing frustration [10, 11, 12, 8]. On one hand, minimization of interfacial area energy prefers structures adopting interfaces with constant mean curvature. On the other, minimizing the chain-stretching energy favors uniform chain-stretching or domain thickness. Both tendencies can be accommodated simultaneously by perfect cylinders and spheres. However, these ideal shapes cannot be packed to fill space uniformly. Voids will be present at the interstitial sites, as illustrated in Figure 1.2 for hexagonally-packed cylinders. Consequently, the ideal micelles will be deformed to resemble the enclosing Voronoi (or Wigner-Seitz) cells. Minimization of interfacial area tends to retain the ideal circular or spherical interfaces. However, a subset of the B-blocks in the corona would be required to stretch more excessively to fill the space at the interstitial sites, which is disfavored by uniform chain-stretching. The interstitial spaces are located at the six corners of the Voronoi cell shown in Figure 1.2. On the other extreme, optimal entropic stretching energy would instead prefer an interface that is a dilated copy of the Voronoi cell, which is depicted in Figure 1.2 for our example of cylinders. Adopting a polyhedral interface will result in deviations from constant mean curvature, producing excessive surface area [10]. This is of course unfavourable from the viewpoint of interfacial energy. The delicate balance between uniform domain thickness and interfacial curvature leads to an intermediate between the two extremes that resembles a shrunken version of the Voronoi cell with rounded edges.

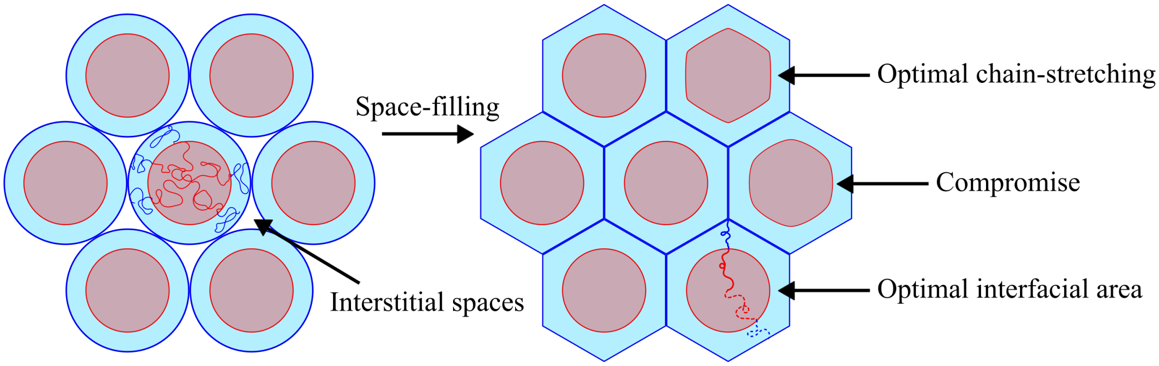

Figure 1.2: Schematic of packing frustration for hexagonally-packed cylindrical micelles composed of A-rich cores and B-rich coronas.

Since planar layers can fill space and are uniform both in curvature and thickness, the lamellar phase experiences no packing frustration [6, 8]. Minimization of packing frustration results in hexagonally close-packed (HEX) cylinders and body-centered cubic (BCC) spheres, respectively, when the A- and B-monomers are of equal size. However, a difference in monomer sizes, referred to as conformational asymmetry, has recently been found to lead to the emergence of complex spherical phases. In

2010, the Bates group experimentally observed an equilibrium Frank-Kasper (FK) σ phase in poly(isoprene)-*b*-poly[(±)-lactide] (PI-PLA) and poly(styrene-*b*-isoprene-*b*-styrene-*b*-ethylene oxide) [13]. Originating from the study of metallic alloys, the FK phases are topologically close-packed structures featuring 12-, 14-, 15- and 16-fold triangulated coordination polyhedras [14, 15, 16]. Characteristic of FK phases are low-symmetry unit cells containing multiple types of atoms with different shapes and sizes [16]. Four examples of FK phases are illustrated in Figure 1.3.

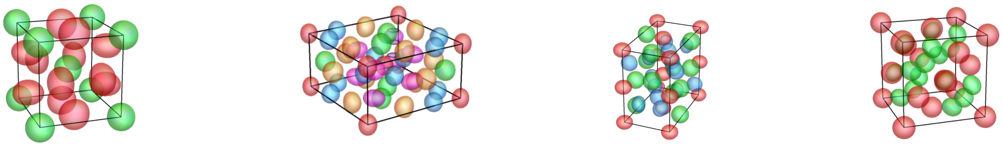

(a) A15 (b) σ (c) C14 (d) C15

Figure 1.3: Illustrations for four examples of Frank-Kasper phases. The colors denote different types of atoms (metallic alloys) or micellar cores (diblock copolymer self-assembly).

A theoretical calculation by Xie *et al.* revealed that conformational asymmetry is one factor that can stabilize the non-classical spherical phases [1]. Conformational asymmetry results in different in block elasticities, where stretching one component incurs a smaller entropic penalty than the other [6, 11]. Intuitively, when stretching ideal springs of unequal elasticity in series, springs that are easier to stretch will be extended more. By the same token, since the A- and B-blocks mimic the behavior of springs, it is entropically favourable to extend the component with the lower stretching cost to a greater degree. The tendency to stretch one block more than the other leads to an increased preference for the interface to curve towards the domains rich in the larger-sized monomers. As a result, higher degrees of conformational asymmetry enable the formation of spherical-packing phases at larger f (see Figure 1.4a). When the block lengths become comparable, the minority-rich cores will be large enough that the interfaces begin to heavily deform towards the shape of the surrounding Wigner-Seitz cell. It is argued that the tendency to form spherical domains with larger sphericity is why the complex spherical phases, such as the FK σ and A15, can then be stabilized [17, 18]. These structures have overall rounder Wigner-Seitz cells than the BCC and $\mathrm{S_{cp}}$ lattices. We note that the "Non-Sphere phases" in Figure 1.4a refers to any not belonging to the spherical-packing phases, such as the hexagonally-packed cylinders or lamellar.

The predicted role of conformational asymmetry in the formation of complex spherical phases was recently investigated experimentally by Schulze *et al.* [2]. The BCC structure was found to be the only spherical phase formed by nearly conformationally symmetric poly(ethylene-*alt*-propylene)-*b*-poly[(±)-lactide] diblock copolymers. At the same time, the phase sequence HEX $\leftrightarrow \sigma \leftrightarrow$ BCC predicted by Xie *et al.* was observed in conformationally asymmetric PI-PLA and poly(ethylethylene)-*b*-poly[(±)-lactide] diblock copolymers. The results of Schulze *et al.* confirm that conformational asymmetry is a key ingredient for stabilizing the novel FK phases. We can see from Figure 1.4 that the qualitative agreement between the experimental and theoretical works is excellent. However on the quantitative level, the FK σ phase exhibits a large window of stability in experiments. To theoretically reproduce the same level of stability, a larger degree of conformational asymmetry would be required. The discrepancy suggests that there are additional factors affecting the self-assembly of complex spherical phases. One possibility for the differences between theory and experiment is dispersity.

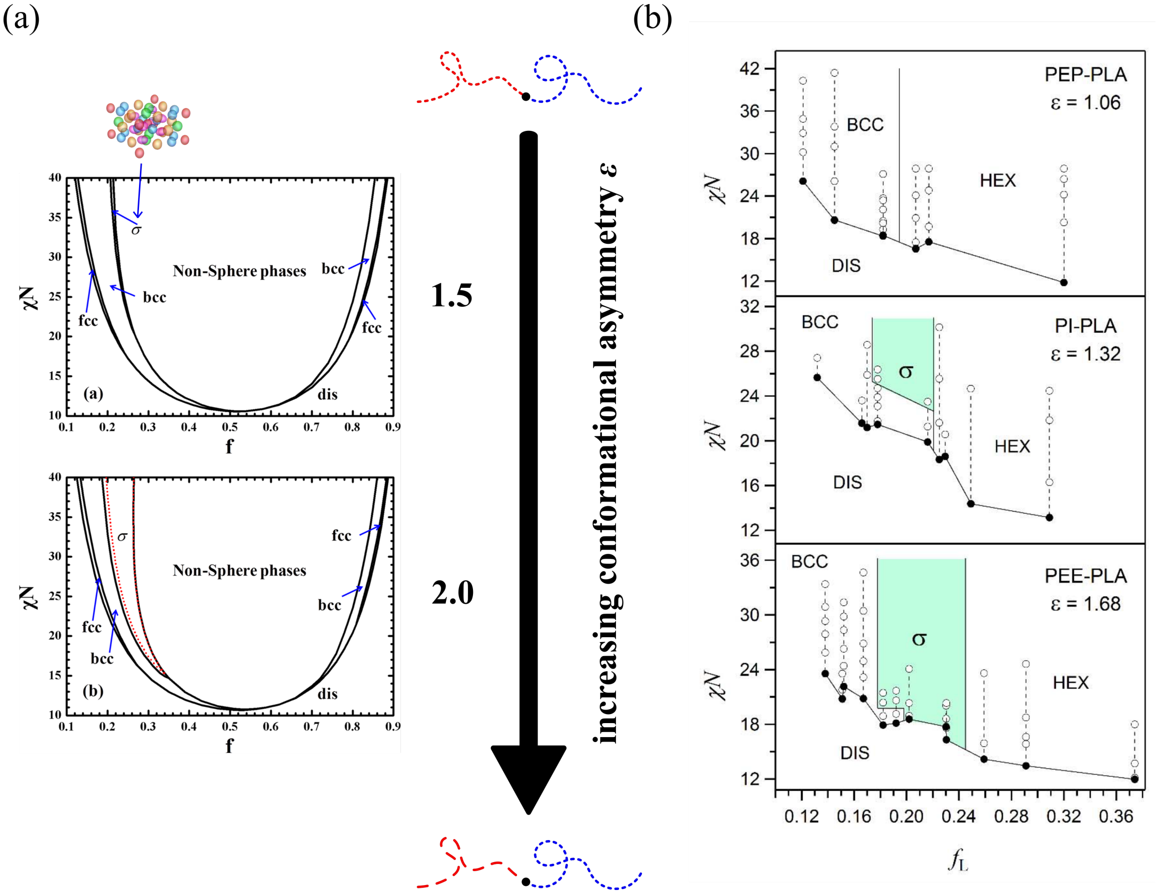

Figure 1.4: Phase diagrams as a function of segregation strength and block volume fraction for different degrees of conformational asymmetry from (a) mean-field calculations by Xie *et al.* [1] and (b) experiments by Schulze *et al.* [2]. Figures are taken from their respective references.

Dispersity refers to a distribution of the molecular weights and is inherent to virtually all synthetic polymers. An example of a molecular weight distribution (MWD) is illustrated in Figure 1.5a. The most common measure of dispersity in the literature is the dispersity index Đ [5, 7, 19], characterizing the width of the MWD. A polymer sample without dispersity is commonly referred to as monodisperse. Early theoretical works by Leibler *et al.* [20] and Hong *et al.* [21] examined the effects of increasing the dispersity index on the disordered phase and order-disorder transition

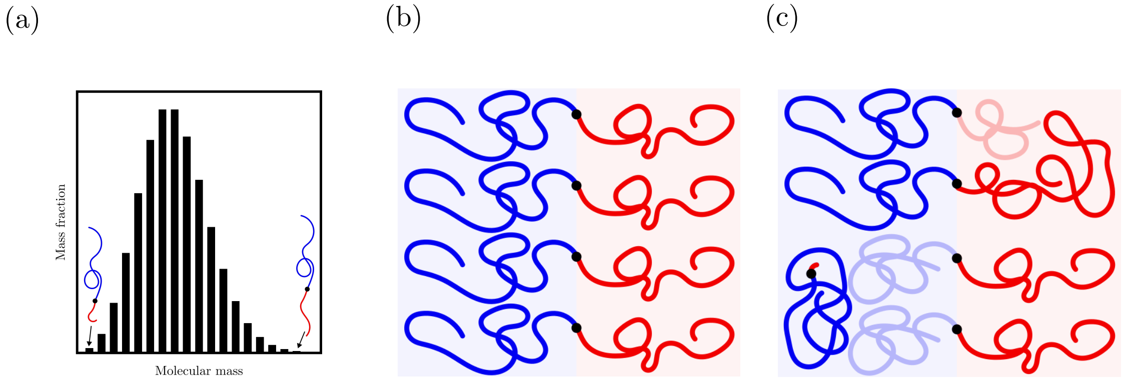

Figure 1.5: (a) Example of a molecular weight distribution. (b) and (c) are schematics illustrating chain packing in monodisperse and disperse diblock copolymers, respectively.

using the random phase approximation suitable for weak degrees of segregation. In both works, the scattering function for the disordered state was derived with the inclusion of dispersity given by the Schulz-Zimm (SZ) distribution. The SZ model is the most widely used MWD when probing the influence of increasing the dispersity index [19]. Several years later, Burger *et al.* investigated dispersity effects on both the ordered and disordered phases again using the RPA [22], incorporating composition fluctuation effects using the framework developed by Fredrickson *et al.* [23]. This collection of works reveal that disperse diblock copolymers would micro-phase separate at lower segregation strengths, and the domain spacing would be larger compared to monodisperse systems.

The first study using numerical mean-field theory on disperse diblock copolymers with the SZ distribution was performed by Sides *et al.* [24, 25]. While Sides *et al.* employed a quadrature method to numerically represent the chain length distribution, Cooke *et al.* alternatively carried out a perturbation expansion to examine the phase behavior of disperse diblock copolymers with narrow MWDs [26]. Matsen has further refined the method introduced by Sides *et al.* and examined the effects of macrophase separation [27], which were largely ignored by the earlier studies. The A-block dispersity effects of linear AB-diblock and BAB-triblock copolymers have also been recently investigated by Matsen [28]. Consistent with early works, these numerical studies found an increase in the domain spacing of the ordered structures. Additionally, the order-order phase boundaries were observed to shift collectively towards compositions richer in the monomers of the more disperse blocks. The predicted effects stem mainly from the reduction of entropic cost for chain-stretching. Disperse polymers can fill space more efficiently than their monodisperse counterparts by using longer chains to pervade the space furthest from the interface. Consequently, the interface will develop a tendency to bend towards the component with the greatest degree of dispersity. Two schematics that contrast chain packing in monodisperse and disperse diblock copolymers are shown in Figures 1.5b-c.

Aside from the SZ distribution, Lynd and coworkers examined the effects of A-block dispersity with an equilibrium polymerization distribution, derived from the kinetics of a reversible chain-growth polymerization process [29]. Lynd *et al.* found that the theoretical phase diagram remained largely unchanged from the SZ distribution. However, the domain size of the self-assembled structures varied substantially between the two different MWDs with identical dispersity indices. The results of Lynd *et al.* highlight that, to fully appreciate the effects of dispersity on the equilibrium behavior of block copolymers, one should consider more than the width of the MWD.

Detailed experimental investigations of dispersity effects on the phase behavior of block copolymers were scarce until the turn of the century. Prior to that, a number of experiments [30, 31, 32, 33] fitted the scattering data of the disordered phase to the expressions derived by Leibler *et al.* [20] and Hong *et al.* [21]. The inclusion of SZ-dispersity brought about better agreement between theoretical predictions and experimental results. In 1985, Hashimoto *et al.* compared the distribution of domain sizes found in a lamellar-forming sample of diblock copolymers to the distribution of molecular weights of the sample [34]. The experiments of Bendejacq and coworkers nearly two decades later on high dispersity diblock copolymers revealed that well-ordered structures from spontaneous assembly were not exclusive to samples with narrow MWDs [35], shattering a previously common belief. A series of experiments by Lynd and coworkers from 2005 to 2007 on polystyrene-*b*-polyisoprene and poly(ethylene-*alt*-propylene)-*b*-poly(lactic acid) diblock copolymers demonstrated the predicted effects of dispersity: enlarged domain spacing and changes in equilibrium morphology from increasing the dispersity index [36, 37]. Lynd *et al.* also examined in detail how the order-disorder transition is affected by dispersity in one of the two blocks [38]. Their experimental results indicated that the segregation strength at which the order-disorder transition takes place depended on whether dispersity was in the minority or majority component. For the former and latter, ordering occurred at lower and higher segregation strengths, respectively. Subsequent simulations by Beardsley *et al.* [39, 40] have confirmed the block-dependent effect of dispersity on the order-disorder transition observed in the experiments of Lynd and coworkers.

Developments in polymer synthesis and processing techniques have now progressed to the extent that the MWD of samples can be precisely designed with specific properties [41, 42]. For instance in 2018, the Fors group showed that the period of the lamellar phase can be regulated by the width and skewness of the distribution in thin films of poly(styrene)-*b*-poly(methyl methacrylate) [43, 41]. Whereas the dispersity index serves as a measure of the width, skewness characterizes the asymmetry of a distribution about its mean [44]. A subsequent investigation by the Fors group further demonstrated that the progression of equilibrium structures is different among polymer samples with MWDs of equal dispersity indices and unequal skewness [4, 41]. Most recently, the Dong group synthesized a library of oligomers composed of a dimethylsiloxane and lactic-acid block that enabled the construction of precise MWDs with varying dispersity indices and skewness [45]. A dependency of the lamellar domain size, as well as order-disorder transition temperature on the skewness was observed. For higher molecular weight block copolymers, a strategy for preparing distributions with programmable properties using automated chromatographic separation was reported by Zhang and coworkers in Ref. [46]. Using the proposed protocol, Zhang *et al.* demonstrated that the parameter space over f can be efficiently explored. A single parent sample of diblock copolymers was sufficient to construct a phase diagram that would otherwise require the preparation of many different samples.

The architecture of copolymers is unlimited and can lead to new exotic structures. Similarly, the shape of a MWD also represents an endless number of variations. As discussed above, the current state of synthesis and processing techniques allows samples with a particular width, skewness or even shape for the distribution to be prepared. A deeper understanding of dispersity effects is required for better harnessing such capabilities. Thus, the aim of the thesis is to investigate how dispersity, in particular the shape of a MWD and related statistical measures such as dispersity index and skewness, influences the phase behavior of diblock copolymers.

In the following chapter, we first present the mean-field theory used to study the equilibrium behavior of disperse polymeric systems. We proceed to examine how the relative stability of complex spherical phases in conformationally asymmetric diblock copolymers is affected by A-block dispersity in the third chapter. Previous theoretical [47, 48, 49] and experimental [50, 51, 52] works on disperse copolymers mainly considered binary mixtures, revealing that a plethora of FK phases can be accessed. Our focus will be on dispersity that is more inherent to synthetic polymers from common synthesis techniques, described by the SZ and Poisson distributions. In both cases, we find that increasing the dispersity (i.e. larger values of dispersity indices) enhances the stability of the complex phases. With the inclusion of dispersity, a lower degree of conformational asymmetry is required to access the σ phase than in monodisperse systems. Our results provide a plausible origin to to the quantitative discrepancy between theoretical predictions and the experimental observations of Schulz *et al.* [2].

In the fourth chapter, we investigate how dispersity beyond the commonly assumed SZ distribution affects the overall phase behavior of diblock copolymers. A general method is presented for modeling the MWDs of polymer samples procured experimentally. We apply the procedure to the MWDs from the experiments by the Fors group [43]. We find that the phase behavior varies between samples with distributions of different shapes. By design, the disperse samples have nearly identical dispersity indices and different skewness. The predicted trends in the equilibrium behavior are in good qualitative agreement with experimental observations. Since control over the shape of a MWD in synthetic polymers is greater than ever and continues to improve, we expect that our method will be valuable for future studies.

In the fifth chapter, we investigate how the shape of the MWD characterized by the dispersity index and skewness influences the relative stability of complex spherical phases. Increasing the dispersity index tends to improve the stability and encourage the formation of novel spherical phases. We furthermore identify that skewness is a vital parameter regulating the selection of accessible spherical packings. For distributions with identical dispersity indices, it is predicted that samples with unequal skewness exhibit different phase behavior. Our findings once again showcases the importance of considering other statistical quantities besides the dispersity index when studying the phase behavior of block copolymers. Lastly, summarizing remarks and outlooks are given in the concluding chapter.

Chapter 2

Theoretical framework

A number of theoretical approaches have been developed for the study of the phase behavior of block copolymers. Broadly speaking, one can divide the approaches into particle-based and field-based ones. In the particle-based approach, the relevant degrees of freedom are the positions and momenta or velocities of the particles. An example is the molecular dynamic simulations where the classical equations of motion are integrated numerically to determine the behavior of the system [53]. Alternatively, the field-based approaches describe the system using a collection of continuous fields, such as the densities of the particles.

At its heart, the problem of equilibrium statistical mechanics is to evaluate the partition function. For a field-based model, the partition function and the ensemble averages are defined in terms of functional integrals over the spatially varying fields. The evaluation of these functional integrals usually cannot be performed analytically. One would resort to various approximations. For polymeric systems, the most successful and widely-used approximation is the mean-field approximation in the form of the self-consistent field theory (SCFT). Since its inception by Edwards [54], there have been many contributions to the development of SCFT [55, 56, 57, 58, 24]. SCFT has found success in the study of phase behavior for a wide variety of polymeric systems [9, 59, 60, 61, 62, 63].

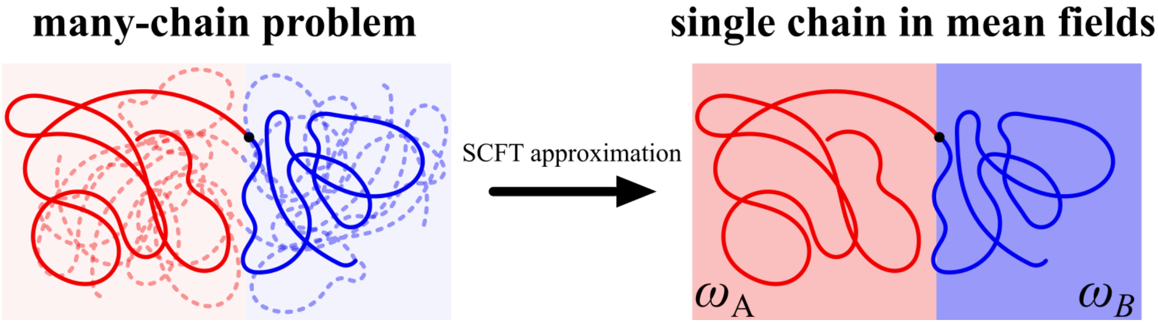

Figure 2.1: Self-consistent field theory reduces the many-chain problem to a single chain interacting with mean fields representing its interaction with other polymers.

The essence of SCFT is the assumption that the main contribution to the functional integrals, representing the partition function and ensemble averages, comes from a single set of fields maximizing the integrand. These fields satisfy a set of SCFT equations derived from the maximization condition. Intuitively, the SCFT approximation reduces the many-body problem to a problem of a single chain in mean fields (Figure 2.1). The fields represent the interactions between the polymers. Despite the enormous simplification afforded by the mean-field approximation, SCFT calculations are carried out numerically, barring a few limiting cases. One example is the random phase approximation (RPA), which is suitable for weakly-segregated systems. In 1980, Leibler employed the RPA and determined the spinodal or limit of stability against small perturbations in the densities for the homogeneous disordered phase in incompressible linear AB-diblock copolymers [56]. The RPA results of Leibler revealed that the disordered state transitions to the lamella and BCC spheres for $f = 0.5$ and $f \neq 0.5$, respectively, when χN is increased. Another analytic treatment of SCFT is strong-segregation theory (SST), applicable for strongly-segregated systems [24, 64, 6, 17]. For diblock copolymers, the assumptions of SST are that the A/B interface is infinitely narrow, and the chains are strongly stretched such that the chain trajectories are described by straight paths perpendicular from the interface. SST predicts that the equilibrium morphology proceeds from lamella to cylinders to spheres as block asymmetry grows from $f = 0.5$. While the RPA and SST provide many insights, the two approaches are approximations to the full SCFT. Thus, numerical calculations are also necessary, serving as a more direct means to studying the mean-field phase behavior without the need for additional approximations.

2.1 Continuous Gaussian chains

We consider a model system of incompressible diblock copolymers with disperse A-blocks and monodisperse B-blocks in a volume V. The connectivity of polymers is treated by the continuous Gaussian chain model [7, 6], in which chain conformations are described by a continuous space curve. We can view polymers as infinitely thin elastic threads composed of statistical segments. The segment length, which we will refer to interchangeable as the Kuhn length, is denoted by b. Each segment corresponds to a number of monomers. The number is selected such that on the scale of b, the chains obey random-walk statistics. Note that from hereafter, we will not distinguish the difference between monomers and statistical segments and use the terms number of monomers, degree of polymerization and contour length interchangeable. The system contains n_c polymer chains of type-c with an A-block length $N_{\mathrm{A},c}$ and therefore a total length of $N_c = N_{\mathrm{A},c} + N_{\mathrm{B}}$. Here, the common B-block length is denoted N_B.

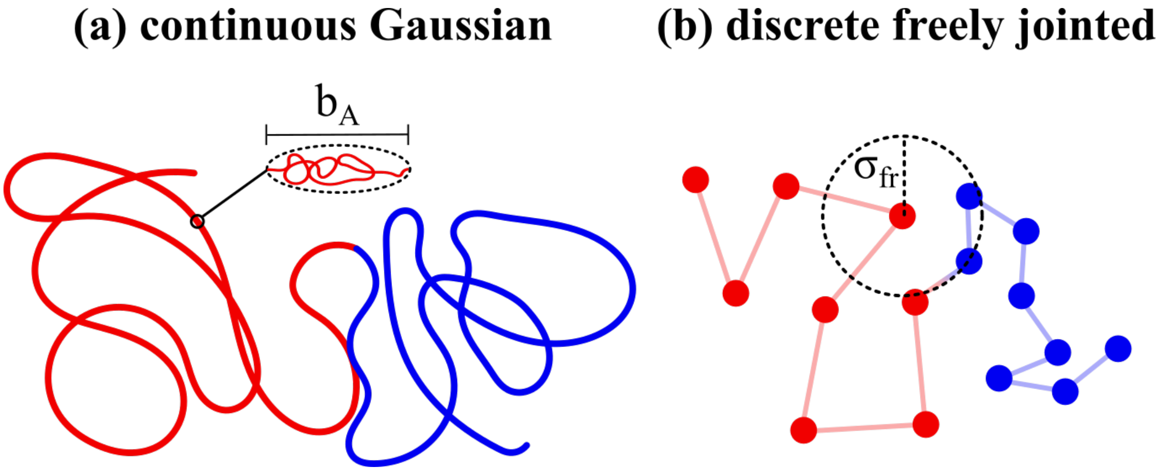

Figure 2.2: Schematic depiction of (a) continuous Gaussian chains and (b) discrete freely jointed chains with finite-range interactions.

The thermodynamics of the system is described by the partition function, which can be expressed as a functional integral over all possible chain conformations [6, 7],

$$\mathcal{Z} = \frac{1}{\prod_c n_c! \, (\lambda_{\mathrm{T},c})^{3n_c}} \prod_c \prod_i^{n_c} \int \mathcal{D}\boldsymbol{R}_{i,c}(s) \mathcal{P}_c \left[\boldsymbol{R}_{i,c}(s)\right] \exp\left(-\beta H[\hat{\phi}_\mathrm{A}(\boldsymbol{r}), \hat{\phi}_\mathrm{B}(\boldsymbol{r})]\right). \quad (2.1)$$

with $\beta = k_B T$ and $\lambda_{\mathrm{T},c}$ denoting the thermal de Broglie wavelengths of type-c polymers. The space curve $\boldsymbol{R}_{i,c}(s)$ describes the conformation of the i^{th} chain of type-c polymers. We write the microscopic monomer volume fraction operators as,

$$\begin{aligned} \hat{\phi}_\mathrm{A}(\boldsymbol{r}) &= \sum_c \sum_i^{n_c} v_\mathrm{A} \int_{I_{\mathrm{A},c}} ds \, \delta\left(\boldsymbol{R}_{i,c}(s) - \boldsymbol{r}\right), \\ \hat{\phi}_\mathrm{B}(\boldsymbol{r}) &= \sum_c \sum_i^{n_c} v_\mathrm{B} \int_{I_{\mathrm{B},c}} ds \, \delta\left(\boldsymbol{R}_{i,c}(s) - \boldsymbol{r}\right), \end{aligned} \quad (2.2)$$

where the bounds of integration are $I_{\mathrm{A},c} = [0, N_{\mathrm{A},c}]$ and $I_{\mathrm{B},c} = [N_{\mathrm{A},c}, N_c]$. The volume of a single α-monomer is denoted v_α. When the non-bonded interaction is taken to be of the contact Flory-Huggins type, we have,

$$H[\hat{\phi}_{\mathrm{A}}(\boldsymbol{r}), \hat{\phi}_{\mathrm{B}}(\boldsymbol{r})] = \frac{1}{\beta} \int d\boldsymbol{r} \, \frac{\chi}{v_0} \hat{\phi}_{\mathrm{A}}(\boldsymbol{r}) \hat{\phi}_{\mathrm{B}}(\boldsymbol{r}), \tag{2.3}$$

where χ is the Flory-Huggins parameter characterizing the chemical incompatibility, and v_0 is a reference volume. The value of χ is generally small and positive, in the range of $0 < \chi \ll 1$, which implies that the interactions between unlike monomers encourage segregation. For instance between polystyrene and poly(methyl methacrylate), $\chi \approx 0.02$ for temperatures of $100 - 200°\mathrm{C}$ [5]. The relationship between the Flory-Huggins parameter and temperature is often expressed empirically as,

$$\chi = \frac{A}{T} + B, \tag{2.4}$$

where the temperature-dependent and independent terms are referred to as the ‘enthalpic’ and ‘entropic’ part, respectively [5].

For continuous Gaussian chains, the Boltzmann factor associated with the bonded potential is given by the Wiener measure [65],

$$\mathcal{P}_c \left[\boldsymbol{R}_{i,c}(s) \right] = \exp \left(- \sum_{\alpha} \int_{I_{\alpha,c}} ds \, \frac{3}{2 b_\alpha^2} \left| \frac{d\boldsymbol{R}_{i,c}(s)}{ds} \right|^2 \right), \tag{2.5}$$

with b_α denoting the Kuhn length of α-monomers that is of order 1 nanometer.

To perform the particle-to-field transformation, we next insert into Eq. (2.1) an identity associated with the functional delta function,

$$1 = \int \mathcal{D}\phi_\alpha(\boldsymbol{r}) \int_{-i\infty}^{+i\infty} \mathcal{D}\omega_\alpha(\boldsymbol{r}) \exp \left\{ \frac{1}{v_0} \int d\boldsymbol{r} \, \omega_\alpha(\boldsymbol{r}) \left[\phi_\alpha(\boldsymbol{r}) - \hat{\phi}_\alpha(\boldsymbol{r}) \right] \right\}, \tag{2.6}$$

where $\phi_\alpha(\boldsymbol{r})$ and $\omega_\alpha(\boldsymbol{r})$ are the volume fraction and auxiliary field respectively, associated with α-monomers. Upon doing so, the partition function can be rewritten as,

$$\begin{aligned}\mathcal{Z} =& \frac{1}{\prod_c n_c! \left(\lambda_{\mathrm{T},c}\right)^{3n_c}} \int \mathcal{D}\phi_{\mathrm{A}}(\boldsymbol{r}) \int_{-i\infty}^{+i\infty} \mathcal{D}\omega_{\mathrm{A}}(\boldsymbol{r}) \int \mathcal{D}\phi_{\mathrm{B}}(\boldsymbol{r}) \int_{-i\infty}^{+i\infty} \mathcal{D}\omega_{\mathrm{B}}(\boldsymbol{r}) \int \mathcal{D}\xi(\boldsymbol{r}) \\ & \times \exp\left(-\beta F[\phi_{\mathrm{A}}(\boldsymbol{r}), \omega_{\mathrm{A}}(\boldsymbol{r}), \phi_{\mathrm{B}}(\boldsymbol{r}), \omega_{\mathrm{B}}(\boldsymbol{r}), \xi(\boldsymbol{r})]\right),\end{aligned} \tag{2.7}$$

where the dimensionless free energy density functional is given by,

$$\begin{aligned}\frac{v_0}{V}\beta F =& \frac{v_0}{V}\beta F[\phi_{\mathrm{A}}(\boldsymbol{r}), \omega_{\mathrm{A}}(\boldsymbol{r}), \phi_{\mathrm{B}}(\boldsymbol{r}), \omega_{\mathrm{B}}(\boldsymbol{r}), \xi(\boldsymbol{r})] \\ =& \frac{1}{V}\int d\boldsymbol{r} \left\{\chi\phi_{\mathrm{A}}(\boldsymbol{r})\phi_{\mathrm{B}}(\boldsymbol{r}) - \omega_{\mathrm{A}}(\boldsymbol{r})\phi_{\mathrm{A}}(\boldsymbol{r}) - \omega_{\mathrm{B}}(\boldsymbol{r})\phi_{\mathrm{B}}(\boldsymbol{r})\right. \\ & \left. - \xi(\boldsymbol{r})\left[1 - \phi_{\mathrm{A}}(\boldsymbol{r}) - \phi_{\mathrm{B}}(\boldsymbol{r})\right]\right\} - \sum_c \frac{n_c v_0}{V}\left(\ln Q_c + \ln Z_c^{(0)}\right).\end{aligned} \tag{2.8}$$

Here, the pressure field $\xi(\boldsymbol{r})$ was introduced as a Lagrange multiplier to enforce the incompressibility condition, and a factor of v_0 has been absorbed into its definition in writing Eq. (2.8). The single-chain partition function reads,

$$\begin{aligned}Z_c =& Z_c[\omega_{\mathrm{A}}(\boldsymbol{r}), \omega_{\mathrm{B}}(\boldsymbol{r})] \\ =& \int \mathcal{D}\boldsymbol{R}_c(s) \exp\left[-\sum_\alpha \int_{I_{c,\alpha}} ds\, \frac{3}{2b_\alpha^2}\left|\frac{d\boldsymbol{R}_c(s)}{ds}\right|^2 - \frac{1}{v_0}\int d\boldsymbol{r}\, \omega_\alpha(\boldsymbol{r})\hat{\phi}_\alpha(\boldsymbol{r})\right] \\ =& \int \mathcal{D}\boldsymbol{R}_c(s) \exp\left[-\sum_\alpha \int_{I_{c,\alpha}} ds\, \frac{3}{2b_\alpha^2}\left|\frac{d\boldsymbol{R}_c(s)}{ds}\right|^2 - \frac{v_\alpha}{v_0}\omega_\alpha\left(\boldsymbol{R}_c(s)\right)\right],\end{aligned} \tag{2.9}$$

with its normalized counterpart given by,

$$Q_c = Q_c[\omega_{\mathrm{A}}(\boldsymbol{r}), \omega_{\mathrm{B}}(\boldsymbol{r})] = \frac{Z_c[\omega_{\mathrm{A}}(\boldsymbol{r}), \omega_{\mathrm{B}}(\boldsymbol{r})]}{Z_c[0,0]} = \frac{Z_c}{Z_c^{(0)}}. \tag{2.10}$$

As a side-note, the constant terms involving the zero-field single-chain partition functions $Z_c^{(0)}$ that appear in Eq. (2.8) may be dropped since we will only be concerned with the differences in the free energy. One never needs to explicitly reference $Z_c^{(0)}$ either when evaluating the normalized partition function as we will see below. The auxiliary field $\omega_\alpha(\boldsymbol{r})$ may be interpreted as an inhomogeneous chemical potential field, appearing as the thermodynamically conjugate variable to $\phi_\alpha(\boldsymbol{r})$ in the free energy Eq. (2.8) [7].

It is more convenient computationally to re-express the single-chain partition function as,

$$Q_c = \frac{1}{V}\int d\boldsymbol{r}\, q_c(\boldsymbol{r}, N_c) = \frac{1}{V}\int d\boldsymbol{r}\, q_c^\dagger(\boldsymbol{r}, N_c), \tag{2.11}$$

where $q_c(\boldsymbol{r}, s)$ and $q_c^\dagger(\boldsymbol{r}, N_c)$ are the forward and backward end-integrated propagators, respectively. For continuous Gaussian chains, the forward end-integrated propagators satisfy the modified diffusion equations [7],

$$\frac{dq_c(\boldsymbol{r}, s)}{ds} = \frac{b_c(s)^2}{6}\nabla^2 q_c(\boldsymbol{r}, s) - \omega_c(\boldsymbol{r}, s) q_c(\boldsymbol{r}, s) \tag{2.12}$$

subject to the boundary condition $q_c(\boldsymbol{r}, 0) = 1$ with,

$$\omega_c(\boldsymbol{r}, s) = \frac{v_\alpha}{v_0}\omega_\alpha(\boldsymbol{r}) \quad \text{and} \quad b_c(s) = b_\alpha \quad \text{for}\, s \in I_{\alpha,c}. \tag{2.13}$$

Similarly, the backward end-integrated propagator is,

$$\frac{dq_c^\dagger(\boldsymbol{r}, s)}{ds} = \frac{b_c^\dagger(s)^2}{6}\nabla^2 q_c^\dagger(\boldsymbol{r}, s) - \omega_c^\dagger(\boldsymbol{r}, s) q_c^\dagger(\boldsymbol{r}, s), \tag{2.14}$$

again subject to the boundary condition $q_c^\dagger(\boldsymbol{r}, 0) = 1$ with,

$$\omega_c^\dagger(\boldsymbol{r}, s) = \frac{v_\alpha}{v_0}\omega_\alpha(\boldsymbol{r}) \quad \text{and} \quad b_c^\dagger(s) = b_\alpha \quad \text{for}\, N_c - s \in I_{\alpha,c}. \tag{2.15}$$

It is often convenient to define a new contour length variable by $\tilde{s} = \frac{v_\alpha}{v_0}s$ and introduce a reference Kuhn length b_0 as the unit of length, such that Eq. (2.12) can be rewritten as,

$$\frac{dq_c(\boldsymbol{r}, \tilde{s})}{d\tilde{s}} = \frac{\varepsilon_c(\tilde{s})^2}{6}\nabla^2 q_c(\boldsymbol{r}, \tilde{s}) - \widetilde{\omega}_c(\boldsymbol{r}, \tilde{s})q_c(\boldsymbol{r}, \tilde{s}). \tag{2.16}$$

Eq. (2.13) now becomes,

$$\widetilde{\omega}_c(\boldsymbol{r}, \tilde{s}) = \omega_\alpha(\boldsymbol{r}) \quad \text{and} \quad \varepsilon_c(\tilde{s}) = \sqrt{\frac{b_\alpha^2 v_0}{b_0^2 v_\alpha}} \quad \text{for}\, \tilde{s} \in \widetilde{I}_{\alpha,c}, \tag{2.17}$$

where $\widetilde{I}_{\mathrm{A},c} = [0, \frac{v_\mathrm{A}}{v_0}N_{\mathrm{A},c}]$ and $\widetilde{I}_{\mathrm{B},c} = [\frac{v_\mathrm{B}}{v_0}N_{\mathrm{A},c}, \frac{v_\mathrm{B}}{v_0}N_c]$. The parameter $\varepsilon_c(\tilde{s})$ measures the conformational asymmetry of the different blocks.

It may be more useful to write the free energy density defined by Eq. (2.8) in terms of the chain number fractions P_c. To do so, we invoke the relationship between the average chain volume fractions $\bar{\phi}_c$ and number fractions,

$$\bar{\phi}_c = \frac{n_c v_c}{V} = \frac{v_c}{\langle v_c\rangle}P_c, \tag{2.18}$$

where $v_c = v_\mathrm{A}N_{\mathrm{A},c} + v_\mathrm{B}N_{\mathrm{B},c}$ is the single-chain volume of type-c polymers and $\langle v_c\rangle =$

$\sum v_c P_c$ is its number-averaged value. We can then write,

$$\begin{aligned}\frac{v_0}{V}\beta F =& \frac{1}{V}\int d\boldsymbol{r}\, \{\chi\phi_{\mathrm{A}}(\boldsymbol{r})\phi_{\mathrm{B}}(\boldsymbol{r}) - \omega_{\mathrm{A}}(\boldsymbol{r})\phi_{\mathrm{A}}(\boldsymbol{r}) - \omega_{\mathrm{B}}(\boldsymbol{r})\phi_{\mathrm{B}}(\boldsymbol{r}) \\ & - \xi(\boldsymbol{r})\left[1 - \phi_{\mathrm{A}}(\boldsymbol{r}) - \phi_{\mathrm{B}}(\boldsymbol{r})\right]\} - \sum_c v_0 \frac{P_c}{\langle v_c\rangle}\left(\ln Q_c + \ln Z_c^{(0)}\right).\end{aligned} \tag{2.19}$$

2.1.1 SCFT approximation

We now apply the SCFT approximation to obtain the free energy of the system [7, 66, 67, 26]. The approximation amounts to minimizing the free energy density functional given by Eq. (2.19) with respect to the monomer volume fractions, auxiliary fields and Lagrange multipliers. Doing so will yield a set of self-consistency equations.

Minimizing with respect to the volume fractions leads to,

$$\begin{aligned}0 = \frac{\delta F}{\delta\phi_{\mathrm{A}}(\boldsymbol{r})} =& \frac{1}{V}\left[\chi\phi_{\mathrm{B}}(\boldsymbol{r}) - \omega_{\mathrm{A}}(\boldsymbol{r}) + \xi(\boldsymbol{r})\right], \\ 0 = \frac{\delta F}{\delta\phi_{\mathrm{B}}(\boldsymbol{r})} =& \frac{1}{V}\left[\chi\phi_{\mathrm{A}}(\boldsymbol{r}) - \omega_{\mathrm{B}}(\boldsymbol{r}) + \xi(\boldsymbol{r})\right].\end{aligned} \tag{2.20}$$

which can be rearranged to form the self-consistent equations,

$$\begin{aligned}\omega_{\mathrm{A}}(\boldsymbol{r}) = \chi\phi_{\mathrm{B}}(\boldsymbol{r}) + \xi(\boldsymbol{r}) \\ \omega_{\mathrm{B}}(\boldsymbol{r}) = \chi\phi_{\mathrm{A}}(\boldsymbol{r}) + \xi(\boldsymbol{r})\end{aligned}. \tag{2.21}$$

The functional derivative with respect to the auxiliary field $\omega_{\mathrm{A}}(\boldsymbol{r})$ is,

$$\begin{aligned}0 = \frac{\delta}{\delta\omega_{\mathrm{A}}(\boldsymbol{r})}\frac{v_0}{V}\beta F =& -\left(\frac{\phi_{\mathrm{A}}(\boldsymbol{r})}{V} + \sum_c v_0 \frac{P_c}{\langle v_c\rangle}\frac{1}{Q_c}\frac{\delta Q_c}{\delta\omega_{\mathrm{A}}(\boldsymbol{r})}\right) \\ =& -\left(\frac{\phi_{\mathrm{A}}(\boldsymbol{r})}{V} + \sum_c v_0 \frac{P_c}{\langle v_c\rangle}\frac{1}{Q_c}\frac{\delta Q_c}{\delta(v_{\mathrm{A}}\omega_{\mathrm{A}}(\boldsymbol{r})/v_0)}\frac{v_{\mathrm{A}}}{v_0}\right).\end{aligned} \tag{2.22}$$

Simplifying the above expression, and resolving the functional derivative yields the self-consistent equation,

$$\phi_{\mathrm{A}}(\boldsymbol{r}) = \sum_c \frac{P_c}{\langle v_c \rangle} \frac{1}{Q_c} \left[v_{\mathrm{A}} \int_{I_{\mathrm{A},c}} ds\, q_c(\boldsymbol{r}, s) q_c^{\dagger}(\boldsymbol{r}, N_c - s) \right]. \tag{2.23}$$

Similarly for $\omega_{\mathrm{B}}(\boldsymbol{r})$, we have,

$$\phi_{\mathrm{B}}(\boldsymbol{r}) = \sum_c \frac{P_c}{\langle v_c \rangle} \frac{1}{Q_c} \left[v_{\mathrm{B}} \int_{I_{\mathrm{B},c}} ds\, q_c(\boldsymbol{r}, s) q_c^{\dagger}(\boldsymbol{r}, N_c - s) \right]. \tag{2.24}$$

Lastly, we can recover the incompressibility condition by minimizing with respect to $\xi(\boldsymbol{r})$,

$$0 = \frac{\delta}{\delta \xi(\boldsymbol{r})} \frac{v_0}{V} \beta F = -\frac{1}{V} \left[1 - \phi_{\mathrm{A}}(\boldsymbol{r}) - \phi_{\mathrm{B}}(\boldsymbol{r}) \right]. \tag{2.25}$$

The solution of the self-consistent equations, Eqs. (2.21)-(2.25), is not unique and different SCFT solutions represent different phases of the system. A constant solution corresponds the homogeneous disordered phase, while spatially-varying solutions correspond to the ordered structures. In general, solving the self-consistent equations is analytically intractable. We instead resort to numerical methods which is detailed in the next section. An effective approach to numerical SCFT is to perform the calculation within one unit cell of an ordered phase. However, the free energy depends on the unit-cell lattice parameters, $\boldsymbol{\theta} = \{\theta_1, \theta_2, ..., \theta_m\}$ with $m \leq 6$ in three dimensions. A subsequent minimization over these parameters will be required. In other words, we are seeking solutions of Eqs. (2.21)-(2.25), denoted as $\{\phi'_\alpha, \omega'_\alpha, \xi'\}$, that also satisfy,

$$\begin{aligned}
0 =& \frac{d}{d\theta_p}\left(\frac{v_0}{V}\beta F[\phi_{\mathrm{A}}(\boldsymbol{r}), \omega_{\mathrm{A}}(\boldsymbol{r}), \phi_{\mathrm{B}}(\boldsymbol{r}), \omega_{\mathrm{B}}(\boldsymbol{r}), \xi(\boldsymbol{r})]\right)\Big|_{\{\phi'_\alpha, \omega'_\alpha, \xi'\}} \\
=& \frac{v_0}{V}\beta\left(\frac{\partial F}{\partial\theta_p} + \int d\boldsymbol{r} \sum_\alpha \left(\frac{\delta F}{\delta\omega_\alpha(\boldsymbol{r})}\frac{d\omega_\alpha(\boldsymbol{r})}{d\theta_p} + \frac{\delta F}{\delta\phi_\alpha(\boldsymbol{r})}\frac{d\phi_\alpha(\boldsymbol{r})}{d\theta_p}\right) + \frac{\delta F}{\delta\xi(\boldsymbol{r})}\frac{d\xi(\boldsymbol{r})}{d\theta_p}\right)\Big|_{\{\phi'_\alpha, \omega'_\alpha, \xi'\}} \\
=& \frac{v_0}{V}\beta\left(\frac{\partial F}{\partial\theta_p}\right)\Big|_{\{\phi'_\alpha, \omega'_\alpha, \xi'\}} = -\sum_c v_0 \frac{P_c}{\langle v_c\rangle}\frac{d\ln Q_c}{d\theta_p}\Big|_{\{\phi'_\alpha, \omega'_\alpha, \xi'\}}.
\end{aligned} \tag{2.26}$$

In going from the second to third line above, we have exploited the fact that $\{\phi'_\alpha, \omega'_\alpha, \xi'\}$ satisfy the mean-field equations and therefore $\frac{\delta F}{\delta\phi_\alpha(\boldsymbol{r})}\big|_{\phi'_\alpha} = \frac{\delta F}{\delta\omega_\alpha(\boldsymbol{r})}\big|_{\omega'_\alpha} = \frac{\delta F}{\delta\xi(\boldsymbol{r})}\big|_{\xi'} = 0$. The derivative of the single-chain partition function with respect to one particular unit-cell parameter is [68],

$$\frac{dQ_c}{d\theta_p} = -\sum_h\sum_k\sum_l \frac{d\left|\boldsymbol{G}_{hkl}\right|^2}{d\theta_p}\left[\sum_\alpha \frac{b_\alpha^2}{6}\int_{I_{\alpha,c}} ds\, \hat{q}_c(\boldsymbol{G}_{hkl}, s)\left[\hat{q}_c^\dagger(\boldsymbol{G}_{hkl}, N_c - s)\right]^*\right], \tag{2.27}$$

where z^* is the complex conjugate of z, and $\widehat{f}(\boldsymbol{k})$ denotes the (forward) Fourier transform of $f(\boldsymbol{r})$. The reciprocal lattice vector is given by,

$$\boldsymbol{G}_{hkl} = h\boldsymbol{b}_1(\boldsymbol{\theta}) + k\boldsymbol{b}_2(\boldsymbol{\theta}) + l\boldsymbol{b}_3(\boldsymbol{\theta}), \tag{2.28}$$

where $\{\boldsymbol{b}_1(\boldsymbol{\theta}), \boldsymbol{b}_2(\boldsymbol{\theta}), \boldsymbol{b}_3(\boldsymbol{\theta})\}$ are three primitive wavevectors. For periodic functions, we define the Fourier transform by,

$$\widehat{f}(\boldsymbol{k}) = \frac{1}{V}\int d\boldsymbol{r} f(\boldsymbol{r}) \exp\left(-i\boldsymbol{k}\cdot\boldsymbol{r}\right). \tag{2.29}$$

2.1.2 Numerical procedure

To iteratively solve the SCFT equations and simultaneously optimize the lattice parameters, we use the variable-cell Anderson mixing method [68] extended to disperse systems (see Appendix D). Within each iteration, the pseudo-spectral method [7] is employed to solve the modified diffusion equations, Eqs. (2.12) and (2.14). We furthermore adopt the Simpson's Rule [69] to numerically perform the integrals over space when evaluating the single-chain partition functions and free energy, as well as the integrals over the contour length s when calculating the monomer volume fractions from Eqs. (2.23)-(2.24). Details regarding the pseudo-spectral method and Simpson's Rule are given in Appendix B and C, respectively.

We begin a numerical SCFT calculation by first constructing an initial ansatz for the monomer volume fractions for the morphology of interest. Analytic expressions of the initial $\phi_\alpha(\boldsymbol{r})$ are given in Appendix A. From the volume fractions, Eq. (2.21) is used with $\xi(\boldsymbol{r}) = 0$ to obtain an initial ansatz for the auxiliary fields, denoted as $\omega_\alpha(\boldsymbol{r})|_1$. Whenever possible, we would use solutions from past calculations as initial conditions. Doing so results in faster convergence provided the difference in the parameters between the two calculations is not too large. We continue as follows:

1. Using the auxiliary fields $\omega_\alpha(\boldsymbol{r})|_m$ determined from the m^{th} iteration, calculate the end-integrated propagators, $q_c(\boldsymbol{r}, s)|_m$ and $q_c^\dagger(\boldsymbol{r}, s)|_m$ from Eqs. (2.12) and (2.14) via the pseudo-spectral method.

2. Compute the monomer volume fractions $\phi_\alpha(\boldsymbol{r})|_m$ from Eqs. (2.23)-(2.24) using $q_c(\boldsymbol{r}, s)|_m$ and $q_c^\dagger(\boldsymbol{r}, s)|_m$.

3. Compute $\hat{q}_c(\boldsymbol{G}_{hkl}, s)|_m$ and $\hat{q}_c^\dagger(\boldsymbol{G}_{hkl}, s)|_m$ by forward Fourier transforming $q_c(\boldsymbol{r}, s)|_m$

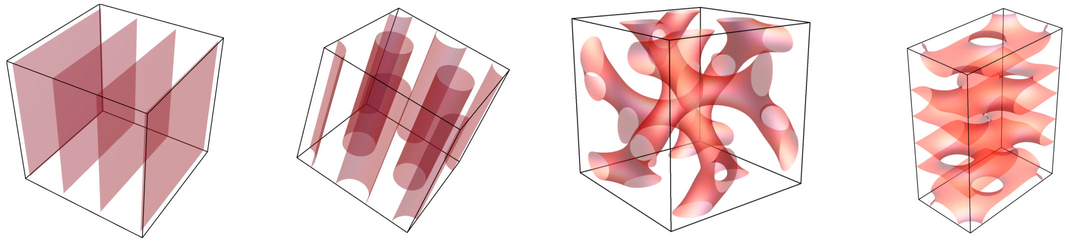

(a) LAM (b) HEX (c) G (d) HPL

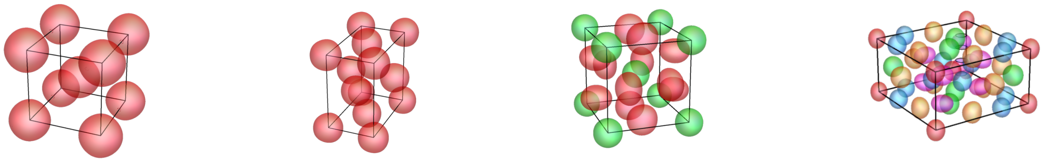

(e) BCC (f) S_{cp} (g) A15 (h) σ

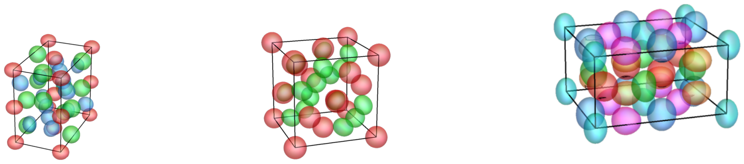

(i) C14 (j) C15 (k) $p\sigma$ (l) Z

(m) M (n) P

Figure 2.3: Schematics of the candidate phases considered in SCFT calculations, where the labels LAM, HEX, G, HPL, BCC and S_{cp} correspond to the lamellar, hexagonally-packed cylindrical, double-gyroid, hexagonally-perforated lamellar, body-centered cubic and hexagonally close-packed spherical phases, respectively.

and $q_c^\dagger(\boldsymbol{r}, s)|_m$.

4. Compute the stress $\frac{d}{d\theta_p}\left(\frac{v_0}{V}\beta F\right)|_m$ from Eq. (2.26) using $\hat{q}_c(\boldsymbol{G}_{hkl}, s)|_m$ and $\hat{q}_c^\dagger(\boldsymbol{G}_{hkl}, s)|_m$ for each lattice parameter θ_p

5. Compute the pressure field $\xi(\boldsymbol{r})$ via,

$$\xi(\boldsymbol{r})|_m = \frac{\omega_{\mathrm{A}}(\boldsymbol{r})|_m + \omega_{\mathrm{B}}(\boldsymbol{r})|_m - \chi}{2}. \tag{2.30}$$

6. Compute the output auxiliary fields using $\phi_\alpha(\boldsymbol{r})|_m$ and $\xi(\boldsymbol{r})|_m$ via Eq. (2.21),

$$\begin{aligned} \omega_{\mathrm{A}}^{(\mathrm{out})}(\boldsymbol{r})|_m &= \chi\phi_{\mathrm{B}}(\boldsymbol{r})|_m + \xi(\boldsymbol{r})|_m, \\ \omega_{\mathrm{B}}^{(\mathrm{out})}(\boldsymbol{r})|_m &= \chi\phi_{\mathrm{A}}(\boldsymbol{r})|_m + \xi(\boldsymbol{r})|_m. \end{aligned} \tag{2.31}$$

7. Compute the deviation functions or residuals for the auxiliary fields,

$$d\left(\boldsymbol{r};\omega_\alpha\right)|_m = \omega_\alpha^{\mathrm{out}}(\boldsymbol{r})|_m - \omega_\alpha(\boldsymbol{r})|_m. \tag{2.32}$$

   The residuals for the lattice parameters are set to,

$$d\left(\theta_p\right)|_m = \frac{d}{d\theta_p}\left(\frac{v_0}{V}\beta F\right)\bigg|_m. \tag{2.33}$$

8. Calculate the free energy density from Eq. (2.19) using $\omega_\alpha^{(\mathrm{out})}(\boldsymbol{r})|_m$, $\phi_\alpha(\boldsymbol{r})|_m$ and $\xi(\boldsymbol{r})|_m$.

9. Calculate the error of the free energy density and the residue errors from Eq. (D.24). If the desired accuracy is reached, a solution has been obtained. Otherwise, continue with the next step.

10. Apply either simple mixing or Anderson mixing to determine the input auxiliary fields and lattice parameters for the next iteration. For simple mixing, we use,

$$\begin{aligned} \omega_\alpha(\boldsymbol{r})|_{m+1} &= \omega_\alpha(\boldsymbol{r})|_m + \lambda_{\mathrm{SM}} d\left(\boldsymbol{r};\omega_\alpha\right)|_m, \\ \theta_p|_{m+1} &= \theta_i + \lambda_{\mathrm{SM}} d\left(\theta_i\right), \end{aligned} \tag{2.34}$$

    where we found $\lambda_{\mathrm{SM}} = 0.1$ offered a good balance between numerical stability and convergence speed.

11. Return to Step 1 to begin the $(m+1)^{\mathrm{th}}$ iteration.

Calculations proceed until the maximum difference in the free energy density between three consecutive iterations, and the residue errors [68] defined by Eqs (D.24)-(D.25) are less than 10^{-7} and 10^{-5}, respectively. The equilibrium phase is lastly determined by a comparison of the free energy of the candidate structures. We illustrate the set of candidate phases of our study in Figure 2.3. As a technical aside, the most computationally expensive part of the outlined procedure is the Fourier transforms associated with calculating the end-integrated propagators via the pseudo-spectral method and its Fourier representations (which is needed to evaluate the stress). Thus, it is worth mentioning that Qiang *et al.* have recently developed a method that greatly reduces the cost of the Fourier operations in what is referred to as crystallographic Fast Fourier Transform [70].

2.2 Continuous distributions of chain lengths

The distribution of polymers with different chains lengths may be specified by a continuous distribution $P(N_c)$ rather than discrete set of values given by P_c. Only one small modification to the SCFT equations derived above is needed to account for a continuous $P(N_c)$ (and N_c), $\sum_c \frac{P_c}{\langle v_c\rangle} \to \int dN_c \, \frac{P(N_c)}{\langle v(N_c)\rangle}$, where

$$\langle v(N_c)\rangle = \int dN_c \, v_c P(N_c). \tag{2.35}$$

Specifically, the free energy functional becomes,

$$\begin{aligned}\frac{v_0}{V}\beta F =& \frac{1}{V}\int d\boldsymbol{r}\, \chi\phi_{\mathrm{A}}(\boldsymbol{r})\phi_{\mathrm{B}}(\boldsymbol{r}) - \omega_{\mathrm{A}}(\boldsymbol{r})\phi_{\mathrm{A}}(\boldsymbol{r}) - \omega_{\mathrm{B}}(\boldsymbol{r})\phi_{\mathrm{B}}(\boldsymbol{r}) \\ & - \xi(\boldsymbol{r})\left[1-\phi_{\mathrm{A}}(\boldsymbol{r})-\phi_{\mathrm{B}}(\boldsymbol{r})\right] - \int dN_c \, v_0 \frac{P(N_c)}{\langle v(N_c)\rangle}\left[\ln Q_c + \ln Z_c^{(0)}\right].\end{aligned} \tag{2.36}$$

The monomer volume fractions from the self-consistent equations now reads,

$$\phi_\alpha(\boldsymbol{r}) = \int dN_c \frac{P(N_c)}{\langle v(N_c)\rangle}\frac{1}{Q_c}\left[v_\alpha \int_{I_{\alpha,c}} ds \, q_c(\boldsymbol{r},s) q_c^\dagger(\boldsymbol{r},N_c-s)\right]. \tag{2.37}$$

Lastly, the stress changes from Eq. (2.26) to,

$$\begin{aligned} 0 =& \frac{d}{d\theta_p}\left(\frac{v_0}{V}\beta F[\phi_{\mathrm{A}}(\boldsymbol{r}),\omega_{\mathrm{A}}(\boldsymbol{r}),\phi_{\mathrm{B}}(\boldsymbol{r}),\omega_{\mathrm{B}}(\boldsymbol{r}),\xi(\boldsymbol{r})]\right)\Bigg|_{\{\phi'_\alpha,\omega'_\alpha,\xi'\}} \\ =& \frac{v_0}{V}\beta\left(\frac{\partial F}{\partial\theta_p}\right)\Bigg|_{\{\phi'_\alpha,\omega'_\alpha,\xi'\}} = -\int dN_c \, v_0 \frac{P(N_c)}{\langle v(N_c)\rangle}\frac{d\ln Q_c}{d\theta_p}\Bigg|_{\{\phi'_\alpha,\omega'_\alpha,\xi'\}}. \end{aligned} \tag{2.38}$$

In deriving these three equations, we have assumed that the distribution $P(N_c)$ is normalized,

$$\int dN_c \, P(N_c) = 1. \tag{2.39}$$

2.3 Accounting for macro-phase separation

Since we are considering systems composed of multiple components, there is a possibility of macro-phase separation. A convenient treatment of multi-phase coexistence has been developed by Matsen [27] for disperse diblock copolymers within the SCFT framework. The essential idea is that the single-phase region will transition to a coexistence region when it is thermodynamically favorable for an infinitesimal amount of another phase to nucleate within the system. The point at which this happens is called the cloud point. The majority (parent) and minority phases are denoted the cloud and shadow phases, respectively [27]. At the cloud point, the shadow phase can take on any distribution of chain lengths, whereas the cloud phase must continue to obey the original distribution. Thermal equilibrium with the cloud phase requires that the chemical potential of the shadow phase must be,

$$\mu_c = -\frac{1}{\beta}\ln\left(\frac{P_c}{Q_c^{(\text{cloud})}}\right) \tag{2.40}$$

for polymer chains of type-c. The single-chain partition of type-c polymers in the cloud phase is denoted $Q_c^{(\text{cloud})}$.

We now apply the mean-field approximation in order to calculate the grand canonical free energy density,

$$\begin{aligned}\frac{v_0}{V}\beta G =& \frac{1}{V}\int d\boldsymbol{r}\,\chi\phi_{\mathrm{A}}(\boldsymbol{r})\phi_{\mathrm{B}}(\boldsymbol{r}) - \omega_{\mathrm{A}}(\boldsymbol{r})\phi_{\mathrm{A}}(\boldsymbol{r}) - \omega_{\mathrm{B}}(\boldsymbol{r})\phi_{\mathrm{B}}(\boldsymbol{r}) \\ & - \xi(\boldsymbol{r})\left[1-\phi_{\mathrm{A}}(\boldsymbol{r})-\phi_{\mathrm{B}}(\boldsymbol{r})\right] - \sum_c z_c\left(Q_c + Z_c^{(0)}\right),\end{aligned} \tag{2.41}$$

where,

$$z_c = \exp\left(-\beta\mu_c\right), \tag{2.42}$$

is often referred to as the activity [7]. Minimization of Eq. (2.41) yields a set of self-consistent equations identical to Eqs. (2.21)-(2.23), (2.25) and (2.26) except with the replacement,

$$\frac{P_c}{\langle v_c\rangle} \to \frac{z_c}{v_0}. \tag{2.43}$$

Explicitly, the self-consistent relations become,

$$\phi_{\mathrm{A}}(\boldsymbol{r}) = \sum_c \frac{z_c}{v_0}\left[v_{\mathrm{A}}\int_{I_{\mathrm{A},c}} ds\, q_c(\boldsymbol{r},s)q_c^{\dagger}(\boldsymbol{r},N_c - s)\right], \tag{2.44}$$

$$\phi_{\mathrm{B}}(\boldsymbol{r}) = \sum_c \frac{z_c}{v_0}\left[v_{\mathrm{B}}\int_{I_{\mathrm{B},c}} ds\, q_c(\boldsymbol{r},s)q_c^{\dagger}(\boldsymbol{r},N_c - s)\right], \tag{2.45}$$

while the stress becomes,

$$\frac{v_0}{V}\beta\left(\frac{\partial G}{\partial\theta_p}\right)\Bigg|_{\{\phi'_\alpha,\omega'_\alpha,\xi'\}} = -\sum_c z_c\frac{d\ln Q_c}{d\theta_p}\Bigg|_{\{\phi'_\alpha,\omega'_\alpha,\xi'\}}. \tag{2.46}$$

Since the chemical potentials were calculated from the cloud phase, its solution computed in the canonical ensemble beforehand can be inserted directly into Eq. (2.41) to evaluate its grand-canonical free energy. The first point where a solution can be found such that the grand canonical free energies of the cloud and shadow phases are equal is where the cloud point occurs.

Numerically, the same procedure outlined in Section 2.1.2 can be applied to locate a solution for the shadow phase, except with Eqs. (2.44)-(2.45) replacing Eqs. (2.23)-(2.24) and Eq. (2.46) replacing Eq. (2.26) when calculating the monomer volume fractions in Step 2 and the stress in Step 4, respectively. We can also accommodate a distribution of chain lengths given by a continuous function by making the substitution $\sum_c z_c \to \int dN_c\, z(N_c)$ in Eqs. (2.41) and (2.44)-(2.46) where,

$$\begin{aligned} z\left(N_c\right) &= \exp\left[-\beta\mu\left(N_c\right)\right], \\ \mu\left(N_c\right) &= -\frac{1}{\beta}\ln\left(\frac{P\left(N_c\right)}{Q^{(\mathrm{cloud})}\left(N_c\right)}\right). \end{aligned} \tag{2.47}$$

2.4 Discrete freely jointed chains

The derivation presented in the previous subsection is for polymers modeled as continuous Gaussian chains, and the inter-molecular interaction was assumed to be of a contact Flory-Huggins type. In this section, we will consider diblock copolymers modeled as discrete freely jointed chains (FJC) with a finite-range Flory-Huggins interaction between unlike monomers [71, 72]. Polymer chains are modeled as a collection of connected rigid rods of a fixed (bond) length which can freely rotate about (Figure 2.2b). Consequently, the length of a freely jointed chain is finite, whereas Gaussian chains can be stretched indefinitely. The inclusion of a non-bonded interaction with finite range is also necessary to avoid unphysical behavior when polymer chains become strongly stretched at large χN [71]. Rather than repeat the full derivation of the SCFT equations, we will highlight the differences and present the essential results.

For discrete FJCs, we write the microscopic volume fraction operators as,

$$\begin{aligned}\hat{\phi}_{\mathrm{A}}(\boldsymbol{r}) =&\sum_{c}\sum_{i}^{n_c} v_{\mathrm{A}} \sum_{s\in S_{\mathrm{A},c}} \delta\left(\boldsymbol{R}_s^{c,i}-\boldsymbol{r}\right), \\ \hat{\phi}_{\mathrm{B}}(\boldsymbol{r}) =&\sum_{c}\sum_{i}^{n_c} v_{\mathrm{B}} \sum_{s\in S_{\mathrm{B},c}} \delta\left(\boldsymbol{R}_s^{c,i}-\boldsymbol{r}\right),\end{aligned} \tag{2.48}$$

where $S_{\mathrm{A},c} = \{1, \ldots, N_{\mathrm{A},c}\}$ and $S_{\mathrm{B},c} = \{N_{\mathrm{A},c}+1, \ldots, N_c\}$.

The free energy density functional with the inclusion of finite-range interactions reads,

$$\begin{aligned}\frac{v_0}{V}\beta F =&\frac{1}{V}\int d\boldsymbol{r}\,\left[\int d\boldsymbol{r}'\,\phi_{\mathrm{A}}(\boldsymbol{r})\left[\chi u_{\mathrm{fr}}\left(|\boldsymbol{r}-\boldsymbol{r}'|\right)\right]\phi_{\mathrm{B}}(\boldsymbol{r}')\right] - \omega_{\mathrm{A}}(\boldsymbol{r})\phi_{\mathrm{A}}(\boldsymbol{r}) - \omega_{\mathrm{B}}(\boldsymbol{r})\phi_{\mathrm{B}}(\boldsymbol{r}) \\ &- \xi(\boldsymbol{r})\left[1-\phi_{\mathrm{A}}(\boldsymbol{r})-\phi_{\mathrm{B}}(\boldsymbol{r})\right] - \sum_c v_0\frac{P_c}{\langle v_c\rangle}\left(\ln Q_c + \ln Z_c^{(0)}\right),\end{aligned} \tag{2.49}$$

where the finite-range non-bonded potential between unlike monomers is assumed to have a Gaussian form,

$$u_{\mathrm{fr}}\left(|\boldsymbol{r}|\right) = \left(\frac{3}{2\pi\sigma_{\mathrm{fr}}^2}\right)^{3/2}\exp\left(\frac{-3|\boldsymbol{r}|^2}{2\sigma_{\mathrm{fr}}^2}\right). \tag{2.50}$$

The range of the interaction is denoted σ_{fr}, while its strength is characterized by Flory-Huggins parameter χ. By design, we have,

$$\begin{aligned}&\int d\boldsymbol{r}\,u_{\mathrm{fr}}\left(|\boldsymbol{r}|\right) = 1, \\ &\int d\boldsymbol{r}\,\left|\boldsymbol{r}\right|^2 u_{\mathrm{fr}}\left(|\boldsymbol{r}|\right) = \sigma_{\mathrm{fr}}^2.\end{aligned} \tag{2.51}$$

When the interaction range $\sigma_{\mathrm{fr}} \to 0$, the potential $u_{\mathrm{fr}}\left(|\boldsymbol{r}|\right)$ approaches a Dirac delta function, and we recover the contact Flory-Huggins interaction given by Eq. (2.3).

The bonded potential for discrete freely jointed chains is,

$$g(|\boldsymbol{r}|;b) = \frac{1}{4\pi b}\delta\left(|\boldsymbol{r}| - b\right), \tag{2.52}$$

where b denotes the natural length of the bond. The relationship between the normalized single-chain partition function and end-integrated propagators is still given by Eq. (2.11). However instead of the modified diffusion equations for the forward end-integrated propagators (see Eqs. (2.12)), we now have,

$$q_c(\boldsymbol{r}, s+1) = e^{-\psi_c(\boldsymbol{r},s)} \int d\boldsymbol{r}'\, g(|\boldsymbol{r} - \boldsymbol{r}'|; b_c(s)) q_c(\boldsymbol{r}', s), \tag{2.53}$$

with $q_c(\boldsymbol{r}, 1) = e^{-\omega_{\mathrm{A}}(\boldsymbol{r})}$,

$$\psi_c(\boldsymbol{r}, s) = \frac{v_\alpha}{v_0}\omega_\alpha(\boldsymbol{r}) \quad \text{for } s \in S_{\alpha,c}. \tag{2.54}$$

The bond length between the s^{th} and $(s+1)^{\mathrm{th}}$ monomer (where counting starts from the free A-block end) is denoted,

$$b_c(s) = \begin{cases} b_{\mathrm{AA}} & 1 \leq s \leq N_{\mathrm{A},c} \\ b_{\mathrm{AB}} & s = N_{\mathrm{A},c} + 1 \\ b_{\mathrm{BB}} & N_{\mathrm{A},c} + 1 < s \leq N_c \end{cases} . \tag{2.55}$$

Similarly for the backward end-integrated propagator, we have,

$$q_c^\dagger(\boldsymbol{r}, s+1) = e^{-\psi_c^\dagger(\boldsymbol{r},s)} \int d\boldsymbol{r}'\, g(|\boldsymbol{r} - \boldsymbol{r}'|; b_c^\dagger(s)) q_c^\dagger(\boldsymbol{r}', s), \tag{2.56}$$

with $q_c^\dagger(\boldsymbol{r},1)=e^{-\omega_{\rm B}(\boldsymbol{r})}$ and,

$$\psi_c^\dagger(\boldsymbol{r},s)=\frac{v_\alpha}{v_0}\omega_\alpha(\boldsymbol{r}) \quad \text{for}\, N_c-s\in S_{\alpha,c}. \tag{2.57}$$

The bond length connecting the $s^{\rm th}$ and $(s+1)^{\rm th}$ monomer (where counting starts from instead the free B-block end) is,

$$b_c^\dagger(s)=\begin{cases} b_{\rm BB} & 1\le s\le N_{{\rm B},c} \\ b_{\rm AB} & s=N_{{\rm B},c}+1 \\ b_{\rm AA} & N_{{\rm B},c}+1<s\le N_c \end{cases}. \tag{2.58}$$

The set of self-consistent equations defined by Eqs (2.23)-(2.24) and (2.21) become,

$$\phi_{\rm A}(\boldsymbol{r})=\sum_c \frac{P_c}{\langle v_c\rangle}\frac{1}{Q_c}\left[v_{\rm A}\exp\left[\frac{v_{\rm A}}{v_0}\omega_{\rm A}(\boldsymbol{r})\right]\sum_{s\in S_{{\rm A},c}} q_c(\boldsymbol{r},s)q_c^\dagger(\boldsymbol{r},N_c-s+1)\right], \tag{2.59}$$

$$\phi_{\rm B}(\boldsymbol{r})=\sum_c \frac{P_c}{\langle v_c\rangle}\frac{1}{Q_c}\left[v_{\rm B}\exp\left[\frac{v_{\rm B}}{v_0}\omega_{\rm B}(\boldsymbol{r})\right]\sum_{s\in S_{{\rm B},c}} q_c(\boldsymbol{r},s)q_c^\dagger(\boldsymbol{r},N_c-s+1)\right], \tag{2.60}$$

and,

$$\begin{aligned} \omega_{\rm A}(\boldsymbol{r}) &= \chi\int d\boldsymbol{r}'\, u_{\rm fr}\left(|\boldsymbol{r}-\boldsymbol{r}'|\right)\phi_{\rm B}(\boldsymbol{r}')+\xi(\boldsymbol{r}), \\ \omega_{\rm B}(\boldsymbol{r}) &= \chi\int d\boldsymbol{r}'\, u_{\rm fr}\left(|\boldsymbol{r}-\boldsymbol{r}'|\right)\phi_{\rm A}(\boldsymbol{r}')+\xi(\boldsymbol{r}) \end{aligned}. \tag{2.61}$$

Using the Fourier representation, Eq.(2.61) can be conveniently written in an almost identical form as Eq. (2.21),

$$\begin{aligned} \widehat{\omega_{\rm A}}\left(\boldsymbol{k}\right) &= \left[\chi\widehat{u_{\rm fr}}\left(|\boldsymbol{k}|\right)\right]\widehat{\phi_{\rm B}}\left(\boldsymbol{k}\right)+\widehat{\xi}\left(\boldsymbol{k}\right), \\ \widehat{\omega_{\rm B}}\left(\boldsymbol{k}\right) &= \left[\chi\widehat{u_{\rm fr}}\left(|\boldsymbol{k}|\right)\right]\widehat{\phi_{\rm A}}\left(\boldsymbol{k}\right)+\widehat{\xi}\left(\boldsymbol{k}\right), \end{aligned} \tag{2.62}$$

where $\widehat{u_{\mathrm{fr}}}\left(|\boldsymbol{k}|\right)$ is the Fourier transform of $u_{\mathrm{fr}}\left(|\boldsymbol{r}|\right)$,

$$\widehat{u_{\mathrm{fr}}}\left(|\boldsymbol{k}|\right) = \exp\left(-\frac{\sigma_{\mathrm{fr}}^2}{6}|\boldsymbol{k}|^2\right). \tag{2.63}$$

The self-consistent equation from minimizing the free energy functional Eq. (2.49) with respect to the pressure field $\xi(\boldsymbol{r})$ is unchanged from Eq. (2.25).

Lastly, the change in the free energy with respect to the lattice parameters θ_p or stress reads,

$$\begin{aligned}
0 =& \frac{d}{d\theta_p}\left(\frac{v_0}{V}\beta F\right) \\
=& \frac{v_0}{V}\beta\left(\frac{\partial F}{\partial\theta_p} + \int d\boldsymbol{r}\,\left(\frac{\delta F}{\delta\omega_\alpha(\boldsymbol{r})}\frac{d\omega_\alpha(\boldsymbol{r})}{d\theta_p} + \frac{\delta F}{\delta\phi_\alpha(\boldsymbol{r})}\frac{d\phi_\alpha(\boldsymbol{r})}{d\theta_p}\right) + \frac{\delta F}{\delta\xi(\boldsymbol{r})}\frac{d\xi(\boldsymbol{r})}{d\theta_p}\right) \\
=& \frac{v_0}{V}\beta\left(\frac{\partial F}{\partial\theta_p}\right) \\
=& \sum_h\sum_k\sum_l \frac{d\left[\chi\widehat{u_{\mathrm{fr}}}\left(|\boldsymbol{G}_{hkl}|\right)\right]}{d|\boldsymbol{G}_{hkl}|^2}\frac{d|\boldsymbol{G}_{hkl}|^2}{d\theta_p}\widehat{\phi_{\mathrm{A}}}\left(\boldsymbol{G}_{hkl}\right)\left[\widehat{\phi_{\mathrm{B}}}\left(\boldsymbol{G}_{hkl}\right)\right]^* \\
&- \sum_c v_0\frac{P_c}{\langle v_c\rangle}\frac{d\ln Q_c}{d\theta_p}.
\end{aligned} \tag{2.64}$$

We see that there is an additional contribution to $\frac{\partial F}{\partial\theta_p}$ not found in Eq. (2.26) coming from the finite-range nature of the non-bonded interactions. As noted earlier, $\chi u_{\mathrm{fr}}\left(|\boldsymbol{r}|\right)$ reduces to the contact Flory-Huggins potential in the limit $\sigma_{\mathrm{fr}} \to 0$. We accordingly see that Eq. (2.64) reduces to Eq (2.26) when the range of the interaction vanishes since $\chi\widehat{u_{\mathrm{fr}}}\left(|\boldsymbol{k}|\right)$ becomes a constant, and therefore $\frac{d[\chi\widehat{u_{\mathrm{fr}}}(|\boldsymbol{k}|)]}{d|\boldsymbol{k}|} \to 0$ as $\sigma_{\mathrm{fr}} \to 0$. The derivative of the single-chain partition for discrete freely jointed chains with respect to the lattice parameter θ_p is,

$$\frac{dQ_c}{d\theta_p} = \sum_{h=1}\sum_{k=1}\sum_{l=1}\sum_{s=1}^{N_c-1} \widehat{h}\left(|\boldsymbol{G}_{hkl}|; b_c(s)\right) \frac{d(|\boldsymbol{G}_{hkl}|^2)}{d\theta_p} \hat{q}_c(\boldsymbol{G}_{hkl}, s) \left[\hat{q}_c^\dagger(\boldsymbol{G}_{hkl}, N_c - s)\right]^*, \tag{2.65}$$

where,

$$\widehat{h}\left(|\boldsymbol{k}|; b\right) = \frac{b}{2|\boldsymbol{k}|} \times \left(\frac{x\cos x - \sin x}{x^2}\right)\Bigg|_{x=|\boldsymbol{k}|b}. \tag{2.66}$$

2.4.1 Numerical procedure

The numerical procedure to obtain SCFT solutions differs slightly between the discrete freely jointed and continuous Gaussian chains. There are two points worth mentioning before outlining the procedure. First, we employ the convolution theorem [73] to evaluate the double spatial integrals in Eq. (2.49) defining the free energy density. Second, we use the convolution theorem again to evaluate Eq. (2.53) to propagate $q_c(\boldsymbol{r}, s)$ to $q_c(\boldsymbol{r}, s+1)$ when solving for the end-integrated propagators. One forward and one backward Fourier transforms are required to numerically determine $q_c(\boldsymbol{r}, s+1)$ from $q_c(\boldsymbol{r}, s)$, which is the same number of Fourier operations as obtaining $q_c(\boldsymbol{r}, s+\Delta s)$ from $q_c(\boldsymbol{r}, s)$ for continuous Gaussian chains via the pseudo-spectral method. In the case of FJCs, the forward transform yields $\hat{q}_c(\boldsymbol{G}_{hkl}, s)$ and $\hat{q}_c^\dagger(\boldsymbol{G}_{hkl}, s)$, which are needed to evaluate the stress. In contrast, the forward Fourier transform results in an intermediate product that is necessary for the pseudo-spectral method (see Appendix B). A second transform has to be performed to obtain the Fourier representations of the propagators at each contour step for continuous Gaussian chains. Therefore, the extra computational cost for evaluating the stress to optimize the unit cell is extremely small for discrete FJCs.

We outline below the iterative procedure to obtain self-consistent solutions for FJCs with finite-range interactions:

1. Using the auxiliary fields $\omega_\alpha(\boldsymbol{r})|_m$ obtained from the m^{th} iteration as inputs, calculate the end-integrated propagators, $q_c(\boldsymbol{r},s)|_m$ and $q_c^\dagger(\boldsymbol{r},s)|_m$ iteratively from Eqs. (2.53) and (2.56). The Fourier transforms, $\hat{q}_c(\boldsymbol{G}_{hkl},s)|_m$ and $\hat{q}_c^\dagger(\boldsymbol{G}_{hkl},s)|_m$, are stored in memory.

2. Compute the monomer volume fractions $\phi_\alpha(\boldsymbol{r})|_m$ from Eqs. (2.59)-(2.60) using $q_c(\boldsymbol{r},s)|_m$ and $q_c^\dagger(\boldsymbol{r},s)|_m$ and subsequently its Fourier transforms $\widehat{\phi_\alpha}\left(\boldsymbol{k}\right)|_m$.

3. Compute the stress $\frac{d}{d\theta_p}\left(\frac{v_0}{V}\beta F\right)|_m$ from Eq. (2.64) using $\hat{q}_c(\boldsymbol{G}_{hkl},s)|_m$, $\hat{q}_c^\dagger(\boldsymbol{G}_{hkl},s)|_m$ and $\widehat{\phi_\alpha}\left(\boldsymbol{k}\right)|_m$.

4. Compute the pressure field $\xi(\boldsymbol{r})$ in real space via,

$$\xi(\boldsymbol{r})|_m = \frac{\omega_{\text{A}}(\boldsymbol{r})|_m + \omega_{\text{B}}(\boldsymbol{r})|_m - \chi}{2} - \lambda_\xi\left[1 - \phi_{\text{A}}(\boldsymbol{r})|_m - \phi_{\text{B}}(\boldsymbol{r})|_m\right], \tag{2.67}$$

   where $\lambda_\xi = 0.2$ was found to provide a good balance between numerical stability and convergence speed.

5. Forward Fourier transform $\xi(\boldsymbol{r})|_m$ to obtain $\widehat{\xi}\left(\boldsymbol{k}\right)|_m$.

6. Compute the output auxiliary fields in Fourier space via Eq. (2.62),

$$\begin{aligned}\widehat{\omega_{\text{A}}}^{(\text{out})}(\boldsymbol{k})|_m &= \left[\chi\widehat{u_{\text{fr}}}\left(|\boldsymbol{k}|\right)\right]\widehat{\phi_{\text{B}}}\left(\boldsymbol{k}\right)|_m + \widehat{\xi}\left(\boldsymbol{k}\right)|_m,\\ \widehat{\omega_{\text{B}}}^{(\text{out})}(\boldsymbol{k})|_m &= \left[\chi\widehat{u_{\text{fr}}}\left(|\boldsymbol{k}|\right)\right]\widehat{\phi_{\text{A}}}\left(\boldsymbol{k}\right)|_m + \widehat{\xi}\left(\boldsymbol{k}\right)|_m,\end{aligned} \tag{2.68}$$

7. Backward Fourier transform $\widehat{\omega_\alpha}^{(\text{out})}(\boldsymbol{k})|_m$ to obtain $\omega_\alpha^{\text{out}}(\boldsymbol{r})|_m$.

8. Continue with Steps 8 to 10 detailed in Section 2.1.2.
9. Return to Step 1 to begin the $(m+1)^{\text{th}}$ iteration.

We again consider solutions to be converged when the maximum difference in the free energy density between three consecutive iterations and the residue errors are less than 10^{-7} and 10^{-5}, respectively.

2.5 Modeling dispersity

The previous sections presented the SCFT framework to study the phase behavior of disperse diblock copolymers. Below, we discuss the molecular weight distributions (MWDs). Two MWDs are commonly used to describe dispersity of synthetic polymers. The first is the discrete Poisson distribution,

$$\mathrm{Pois}\left(x;\mu\right) = \frac{\mu^{x}\mathrm{e}^{-\mu}}{x!}, \quad x = 0, 1, 2, .. \tag{2.69}$$

with a mean of $\langle x \rangle = \sum_x xP(x) = \mu$. For our convenience, we rewrite the above in terms of $\lambda = x/\mu$ as,

$$\mathrm{Pois}\left(\lambda;\mu\right) = \frac{\mu^{\lambda\mu}}{(\lambda\mu)!}\mathrm{e}^{-\mu}, \quad \lambda = 0, \frac{1}{\mu}, \frac{2}{\mu}, ... \tag{2.70}$$

The Poisson distribution is suitable for describing the dispersity of synthetic polymers produced via living polymerizations [74]. Numerically, the summation cannot be carried out to infinite. We instead resort to a simple coarse-graining approximation detailed in Appendix E.

The second model is the continuous Schulz-Zimm (SZ) distribution,

$$\mathrm{SZ}\left(x;\mu,k\right)=\frac{1}{\mu}\frac{k^k}{\Gamma(x)}\left(\frac{x}{\mu}\right)^{k-1}\exp\left(-k\frac{x}{\mu}\right),\quad x\geq 0. \tag{2.71}$$

where $\Gamma(x)$ is the gamma function while μ and k are commonly referred to as the scale and shape parameter, respectively. It is more convenient to re-express Eq. (2.71) in terms of $\lambda = x/\mu$, yielding:

$$\mathrm{SZ}\left(\lambda;k\right)=\frac{k^k}{\Gamma(k)}\lambda^{k-1}\mathrm{e}^{-k\lambda},\quad \lambda\geq 0. \tag{2.72}$$

By construction, the mean is $\langle\lambda\rangle = 1$. The SZ distribution is often applicable to polymers synthesized using condensation or addition polymerizations [74]. Numerically, we employ the Gauss-Laguerre quadrature rule [75] to evaluate any integral over λ involving the SZ distribution. The use of the Gauss-Laguerre quadrature rule in polymeric SCFT was introduced by Sides and Fredrickson [24]. An illustration of the Poisson and SZ distributions is shown in Figure 2.4.

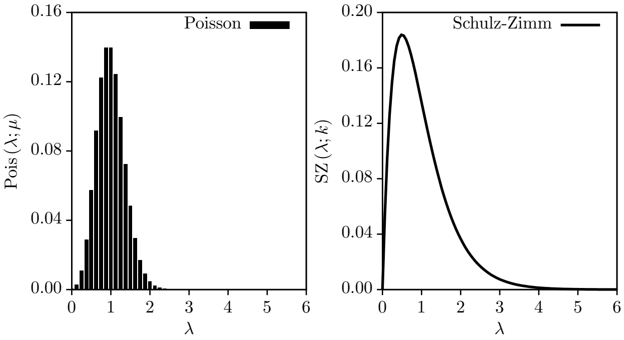

Figure 2.4: Plot of the (left) Poisson distribution Pois $(\lambda;\mu)$ with $\mu = 8$ and (right) Schulz-Zimm distribution SZ $(\lambda;k)$ with $k = 2$ as a function of λ.

A MWD could be characterized by its moments. Related to the second moment, the dispersity index is the most common measure of dispersity in polymer literature:

$$Đ\left(N_c\right) = \frac{\langle {N_c}^2 \rangle}{\langle N_c \rangle^2}. \tag{2.73}$$

When only one block is disperse (and the other is monodisperse), it may be more useful to consider the α-block dispersity index $Đ(N_{\alpha,c})$. For the Poisson distribution, the dispersity index is $Đ\left(\lambda\right) = (\mu + 1)/\mu$, while we have $Đ\left(\lambda\right) = (k + 1)/k$ for the SZ distribution. Recent experiments have shown that the phase behavior can depend on the asymmetry of the MWD about its mean [43, 4, 41, 45]. This property is captured by the skewness,

$$\widetilde{\mu}_3 = \frac{\langle (N_c - \langle N_c \rangle)^3 \rangle}{\langle (N_c - \langle N_c \rangle)^2 \rangle^{\frac{3}{2}}}, \tag{2.74}$$

which is related to the third moment.

Chapter 3

Effect of dispersity on the formation of complex spherical phases

In the present chapter, we examine the effects of dispersity on the formation of complex spherical packing phases in conformationally asymmetric AB-diblock copolymers. We quantify conformational asymmetry using the parameter,

$$\varepsilon = \sqrt{\frac{b_{\mathrm{A}}^2 v_{\mathrm{B}}}{b_{\mathrm{B}}^2 v_{\mathrm{A}}}}, \tag{3.1}$$

which comes from setting the reference Kuhn length as $b_0 = b_{\mathrm{A}}$ and the reference volume as $v_0 = v_{\mathrm{A}}$ in Eq. (2.17). We assume the A-blocks are disperse and model the polymers as continuous Gaussian chains with two different MWDs, namely the Poisson and Schulz-Zimm (SZ) (see Section 2.5), for the A-blocks. For both cases, we find that the stability of the Frank-Kasper σ phase increases with the degree of dispersity characterized by the dispersity index, Eq. (2.73). For the SZ distribution, a number of FK structures other than the σ phase could be accessed by increasing the conformational asymmetry. We also investigate the effects of macro-phase separation. The regions of two-phase coexistence involving the σ phase are narrow compared to the single-phase regions. By examining the spatial organization of polymer chains within the spherical structures, we determine that inter- and intra-domain chain segregation effects provide the mechanisms responsible for the enhanced stability and resulting appearance of the complex spherical phases. This is in agreement with previous theoretical studies on block copolymer blends [47].

3.1 Poisson distribution

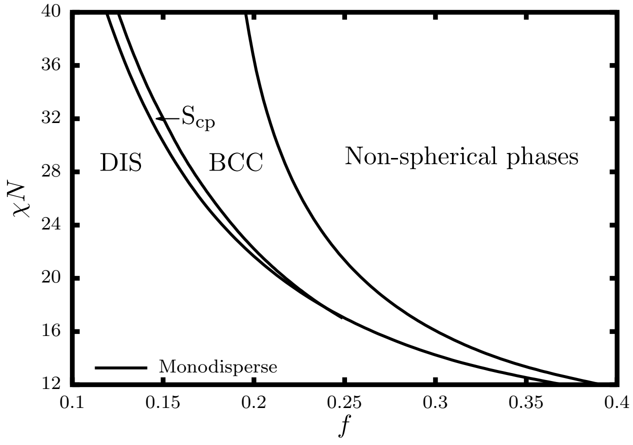

Figure 3.1: Phase diagram of a monodisperse system as a function of the A-volume fraction f and segregation strength χN with $\varepsilon = 1.32$. The labels, BCC, S_{cp} and DIS, correspond to the body-centered cubic spheres, close-packed spheres and homogeneous disordered phase, respectively.

The phase behavior of a monodisperse melt is first briefly considered, which serves as a useful reference when examining the effects of dispersity. In Figure 3.1, we plot the phase diagram of a diblock copolymer melt as a function of the A-volume fraction f and segregation strength χN. The conformational asymmetry parameter is set to $\varepsilon = \sqrt{b_{\mathrm{A}}^2 v_{\mathrm{B}}/b_{\mathrm{B}}^2 v_{\mathrm{A}}} = b_{\mathrm{A}}/b_{\mathrm{B}} = 1.32$, which nearly coincides with that of PI-PLA diblock copolymers [2]. We assume for convenience that the single-monomer volumes are equal, $v_{\mathrm{A}} = v_{\mathrm{B}} = v_0$. In agreement with Xie *et al.* [1], the complex spherical phases are absent since the selected conformational asymmetry $\varepsilon = 1.32$ is below the critical threshold of $\varepsilon \approx 1.5$. The phase behavior resembles largely to that of conformationally symmetric diblock copolymers [9] except the phase boundaries between different ordered phases shift to larger A-volume fractions due to more flexible A-blocks when $b_{\mathrm{A}} > b_{\mathrm{B}}$. There is a greater tendency for the interface to bend towards the A-rich domains in conformationally asymmetric diblock copolymers [11, 17, 24].

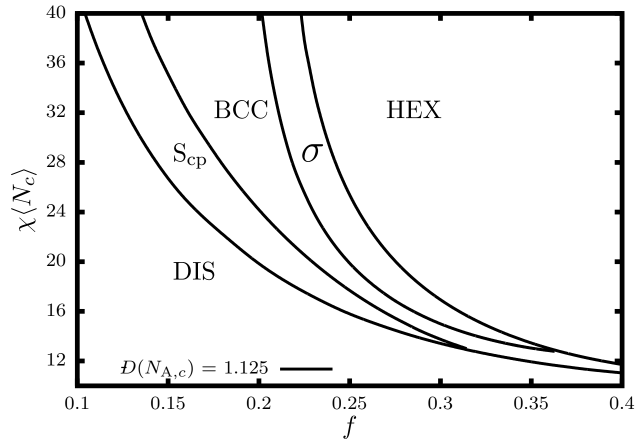

Figure 3.2: Phase diagram of the A-block disperse system as a function of the volume fraction of A-monomers f and average segregation strength $\chi\langle N_c\rangle$ with $\varepsilon = 1.32$ and $P_c = \mathrm{Pois}(\lambda_c; \mu)$. Note that effect of macro-phase separation is ignored here.

We now consider dispersity described by the Poisson distribution [see Eq. (2.70)]. In Figure 3.2, the phase diagram is plotted as a function of f and the number-averaged segregation strength $\chi \langle N_c \rangle$. The number fraction or probability of polymers with A-block length $N_{\mathrm{A},c} = \lambda_c N_{\mathrm{A,ref}}$ is given by $P_c = \mathrm{Pois}(\lambda_c; \mu)$ where $N_{\mathrm{A,ref}}$ denotes a reference contour length. The value of μ is set to 8, yielding a dispersity index of $Đ(N_{\mathrm{A},c}) = 1.125$. We moreover use the coarse-graining procedure outlined in Appendix E with $M_\lambda = 4$ to approximately represent the Poisson distribution in numerical calculations. For the time being, the possibility of macro-phase separation is also ignored. We defer examining both the effects of coarse-graining and macro-phase separation later and show that neither effects will have a significant impact on the phase behavior.

As seen in Figure 3.2, the emergence of the FK σ phase is predicted for $\chi \langle N_c \rangle \gtrsim 13$. For $\chi \langle N_c \rangle \gg 13$, a phase transition sequence of HEX $\to$ σ $\to$ BCC is found from the phase diagram as f is decreased. We note that the same sequence of ordered phases is observed in the experiments of Schulze *et al.* [2]. Since reducing packing frustration is vital for the formation of complex spherical phases, the predicted appearance of the σ phase is evidence that dispersity alleviates packing frustration, an idea proposed previously for blends [26, 27, 47]. In disperse systems, longer chains can be used to more efficiently fill the spaces furthest from the interface, which relaxes the stretching of the shorter chains. As a consequence, dispersity provides a means of lowering the critical ε threshold above which the self-assembly of complex spherical phases can occur, consistent with the experiments of Schulz *et al.*.

In Figure 3.3, we plot the difference in free energy density, Eq. (2.19), between the BCC and two other phases, HEX and σ, as a function of ε for a monodisperse and disperse melt with $P_c = \mathrm{Pois}(\lambda_c; \mu)$, respectively. We apply the same coarse-graining procedure with $M_\lambda = 4$ again to represent the Poisson distribution in calculations.

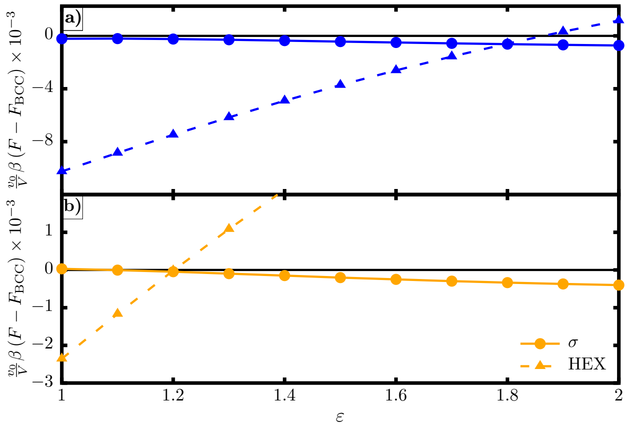

Figure 3.3: Difference in the free energy density between the BCC and HEX phases (dashed lines), as well as between the BCC and σ phases (solid lines) as a function of ε where the A-block lengths are a) monodisperse and b) distributed according to $P_c = \mathrm{Pois}\left(\lambda_c; \mu\right)$. The parameters are $\mu = 8$, $f = 0.25$ and $\chi N = \chi \left\langle N_c \right\rangle = 30$.

The critical value of ε above which the σ phase occurs can be read off directly from the plot. For monodisperse blocks, the conformational asymmetry parameter has to exceed $\varepsilon = 1.8$ for the σ phase to occur. With dispersity included, the formation of the σ phase takes place when $\varepsilon \geq 1.2$. Thus, a modest degree of dispersity ($Đ\left(N_{\mathrm{A},c}\right) = 1.125$) can lead to a 50% reduction in the critical value of ε for the appearance of the FK σ phase.

We next examine the effect of the coarse-graining approximation for the Poisson distribution (see Appendix E). The procedure amounts to replacing the exact distribution, which is non-zero for all $\lambda \geq 0$, with an approximant described by M_λ non-zero values of λ. We present the phase boundaries involving the σ phase for different values of M_λ in Figure 3.4a. First and foremost, the σ phase is predicted to occur at every level of coarse-graining considered. Its consistent appeareance suggests that the qualitative phase behavior is unaffected by our approximation. As M_λ increases, the HEX $\leftrightarrow$ σ phase boundary collectively shifts to larger values of f, while the BCC

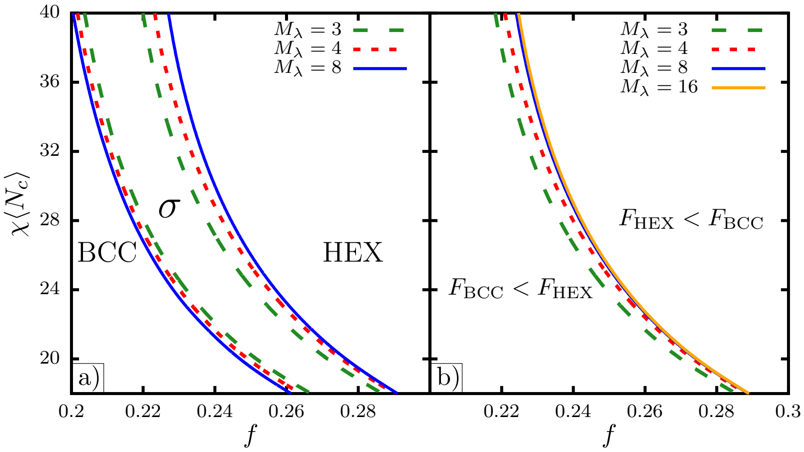

Figure 3.4: a) Phase boundaries involving the σ phase, and b) the locus of points where the free energy densities of the BCC and HEX phases are equal shown as a function of the volume fraction of A-monomers f and segregation strength $\chi\langle N_c\rangle$. The distribution of A-blocks lengths is given by $P_c = \mathrm{Pois}\,(\lambda_c;\mu)$ with $\mu = 8$ and $\varepsilon = 1.32$.

$\leftrightarrow \sigma$ boundary moves to lower volume fractions. In other words, the stability region of the σ phase slightly widens as the extent of the coarse-graining becomes finer. More importantly, we find that the shift in the phase boundaries from increasing $M_\lambda = 4$ to 8 is much less pronounced than the shift from a change involving smaller values of M_λ (i.e. $3 \rightarrow 4$). A similar trend is observed in Figure 3.4b, where we plot the locus of points for which the free energy of the hexagonally-packed cylinders is equal to that of the BCC phase. The illustrated curves would be the equilibrium phase boundaries, had the FK phases been excluded from the set of candidate structures. Since only the free energies of the HEX and BCC phases are needed for the comparison, we were able to perform the calculations for up to $M_\lambda = 16$. The shift in the curves shown in Figure 3.4b as M_λ increases from 3, 4, 8 to 16 becomes progressively smaller with each increment. Together, Figure 3.4a and 3.4b suggests that the difference between the exact phase boundaries and those calculated using the 8-point approximation will be less than the difference between $M_\lambda = 4$ and 8. For the latter, we find that the difference is on the order of $f \sim 10^{-3}$.

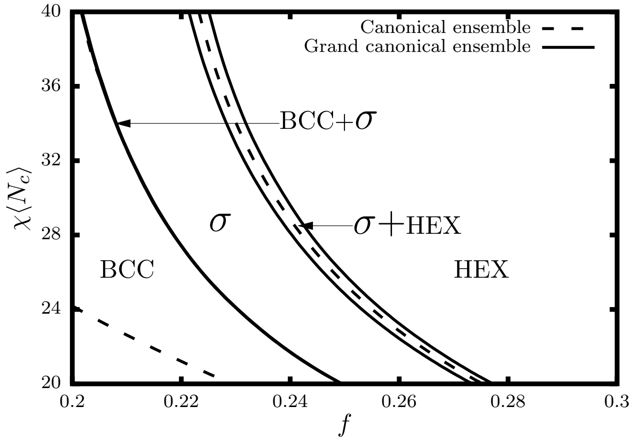

Figure 3.5: Phase diagram as a function of the volume fraction of A-monomers f and segregation strength $\chi \langle N_c \rangle$ of the A-block disperse system with $\varepsilon = 1.32$, $P_c = \text{Pois}\,(\lambda_c; \mu)$ and $\mu = 8$, with the effect of macro-phase separation included. Note that the two-phase coexistence between the BCC and σ phases is narrower than the lines indicating the phase boundaries.

3.1.1 Effect of macro-phase separation

Having demonstrated that our simple approximation scheme can produce qualitatively or quantitatively accurate results depending on the level of coarse-graining, we examine the effects of macro-phase separation. We show in Figure 3.5 the phase boundaries involving the σ phase with phase coexistence included using the framework outlined in Section 2.2. Here, we choose $M_\lambda = 4$ for computational convenience. The main concern of macro-phase separation is that the σ phase could be replaced by a coexisting state between the neighboring classical spherical phase and hexagonally-packed cylinders. From Figure 3.5, we see that that this is not the case. As expected, there are regions of phase coexistence that emerge. We find however that the sequence of equilibrium structures, HEX $\leftrightarrow \sigma \leftrightarrow$ BCC, remains unchanged from what was previously shown in Figure 3.2. Moreover, both the coexistence regions between the σ and HEX, as well as between the σ and BCC phases are negligibly small. The former spans less than half a percent in f, while the $\sigma +$BCC region is narrower than the lines denoting the phase boundaries. This is consistent with the results of Ref. [27], where the coexistence regions between two ordered phases are dwarfed by the neighboring single-phase regions when $Đ\left(N_{\mathrm{A},c}\right) \leq 1.2$. Furthermore, the two-phase region between adjacent spherical-packing phases is expected to be small regardless of the dispersity. The reason is that the free energy differences between various spherical phases are minute compared to between phases with different structural motifs, say spheres and cylinders. Lastly, the narrowness of the two-phase regions may be presumably the reason for no experimental reports of macro-phase separation in Ref. [2].

3.2 Schulz-Zimm distribution

We now consider the dispersity described by the Schulz-Zimm distribution, Eq. (2.72). As before, the conformational asymmetry parameter is set to $\varepsilon = 1.32$. The phase behavior of the system as a function of f and $\chi \left\langle N_c \right\rangle$ is shown in Figure 3.6, where the probability distribution of the A-block length $N_{\mathrm{A},c}$ is $P_c = \mathrm{SZ}\left(\lambda_c; k\right)$ for $k = 2$, 3 and 4, corresponding to dispersity indices of $Đ\left(N_{\mathrm{A},c}\right) = 1.25$, $1.\overline{33}$ and 1.50, respectively. Similar to Sides and Fredrickson [24], the 8-point Gauss-Laguerre quadrature is used to numerically evaluate Eqs. (2.23) and (2.36). The effect of macro-phase separation is ignored in the phase diagram. We also plot only the order-order phase boundaries as we are mainly concerned with how the relative stability between ordered structures changes with increasing degrees of dispersity.

As illustrated in Figure 3.6, the σ phase is an equilibrium structure for all three values of k. Compared with the case of the Poisson distribution, the σ phase occupies a significantly larger area of the phase diagram. Moreover, we see that the window of stability for the σ phase widens as $Đ\left(N_{\mathrm{A},c}\right)$ increases from 1.25 to 1.5. The observed trend indicates again that dispersity relieves packing frustration and also that the extent of the relief is greater at larger values of $Đ\left(N_{\mathrm{A},c}\right)$. In agreement with predictions, Zhang *et al.* found that the FK phases appeared over a narrower region of the phase diagram for less disperse samples of poly(dodecyl acrylate)-*block*-poly(lactide) [46]. Intuitively, a larger dispersity index would mean a greater variety of polymers with different chain lengths which could be used to fill space more efficiently. One other difference from the Poisson distribution is that the σ phase can directly transition to the S_{cp} phase by lowering f. The absence of the BCC phase at higher $Đ\left(N_{\mathrm{A},c}\right)$ has been predicted previously [12, 6, 26, 27]. The displacement of polymers with shorter A-blocks from the cores into the B-rich matrix relieves the packing frustration that favors the BCC over the S_{cp} lattice. We will shortly provide evidence supporting such behavior.

Next, we consider diblock copolymers with a larger degree of conformational asymmetry and demonstrate that dispersity could yield ordered phases that are metastable in monodisperse systems. In Figure 3.7a, we show the phase diagram for the SZ distribution with $Đ\left(N_{\mathrm{A},c}\right) = 1.5$ and $\varepsilon = 2$. While the σ phase is present as expected, three other FK phases, namely A15, C14 and C15, also emerge. The appearance of the C14 and C15 structures is in stark contrast with the behavior of monodisperse linear diblock copolymers. In the absence of dispersity, increasing ε leads to an enlarged region of stability for the σ phase once $\varepsilon \approx 1.5$ [1], with the A15 eventually

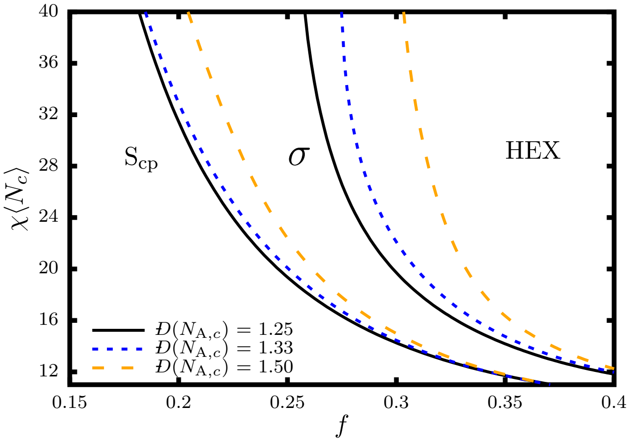

Figure 3.6: Phase diagram as a function of the volume fraction of A-monomers f and segregation strength $\chi\langle N_c\rangle$ of the A-block disperse system with $\varepsilon = 1.32$ and $P_c = \mathrm{SZ}(\lambda_c; k)$ for $k = 2$ (yellow), 3 (blue) and 4 (black).

occurring when $\varepsilon \gtrsim 2.1$ [76]. The same selection of FK phases in Figure 3.7a is likewise reported in binary blends of conformationally symmetric diblock copolymers [50]. In fact, we will see in the next subsection that the mechanisms for the formation of complex spherical phases in binary mixtures are also found in the disperse systems being considered.

3.3 Chain segregation effects

To better understand the impact of dispersity on the formation of complex spherical phases, we examine the spatial arrangement of polymer chains within the self-assembled structures. For the sake of clarity, we perform our analysis based on the FK A15 phase. Its unit cell is cubic, containing two non-equivalent spherical domains.

We first consider dispersity effects on the spatial organization of chain junctions. Figures 3.8a-d show plots of the normalized junction distribution $P_c q_c(\boldsymbol{r}, \lambda_c N_{\mathrm{A,ref}}) q_c^{\dagger}(\boldsymbol{r}, N_{\mathrm{B}})$ on the $z = 0$ plane for various values of λ_c corresponding to different A-block lengths.

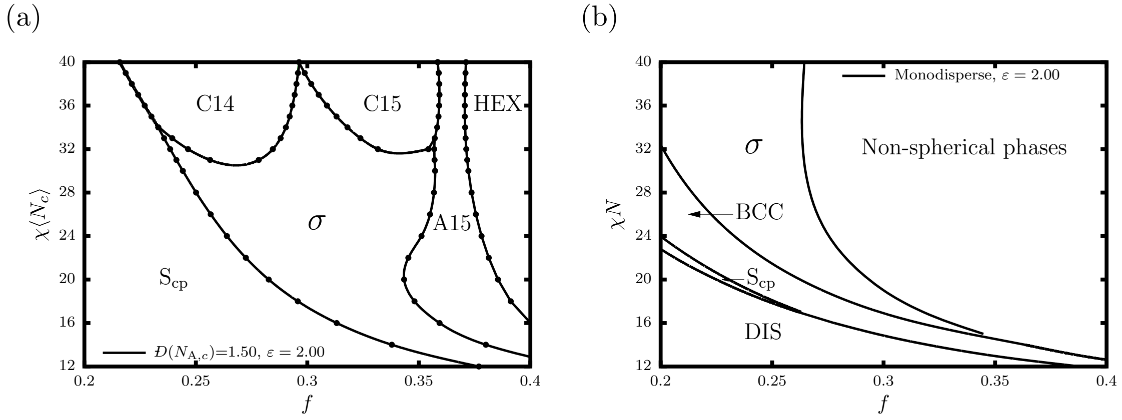

Figure 3.7: Phase diagram as a function of the volume fraction of A-monomers f and segregation strength $\chi \langle N_c \rangle$ of the (a) A-block disperse and (b) monodisperse systems with $\varepsilon = 2$. For (a), the distribution of polymers with different A-block lengths is $P_c = \mathrm{SZ}\left(\lambda_c; k\right)$ where $k = 2$. Including dispersity leads to the appearance of three other FK phases.

Here, P_c is given by the SZ distribution. For reference, we also include a plot of the A-volume fraction $\phi_{\mathrm{A}}(\boldsymbol{r})$ in Figure 3.8e. The white regions depict the A/B interface, which is defined as the isosurface with $\phi_{\mathrm{A}}(\boldsymbol{r}) = 0.5$. The behavior of chain junctions is largely dependent on the length of the A-block. The junction distribution belonging to polymers with very short A-blocks ($\lambda_c = 8.33 \times 10^{-2}$) is shown in Figure 3.8a. We find that junctions are dislodged from the A/B interface and most concentrated at the interstitial spaces within the B-matrix. As noted earlier, the BCC is generally preferred over the $\mathrm{S_{cp}}$ phase due to its lower degree of packing frustration. With the free polymer chains in the B-rich corona acting as fillers, packing frustration is released, and the preferred lattice becomes $\mathrm{S_{cp}}$ [12, 6, 26, 27]. For polymers with slightly longer A-blocks, Figure 3.8b shows that the junctions are now located at the A/B interface. The junctions moreover display a clear preference to reside in areas with higher interfacial curvature. In contrast, the junction distribution exhibits only subtle changes and is rather uniform at the interface for $\lambda_c = 1.133$ shown in

Figure 3.8c. We depict lastly how the junctions are distributed for polymers with the longest A-blocks ($\lambda_c = 5.383$) in Figure 3.8d. Unlike the molecules with shorter A-blocks, the longer chains tend to be situated in the regions with lower interfacial curvature. The same tendency is seen in the arrangement of junctions for the two non-equivalent spherical domains. We find that the junction distribution is lower in the smaller, rounder cores at the corners than in the polyhedral-like cores on the faces of the unit cell.

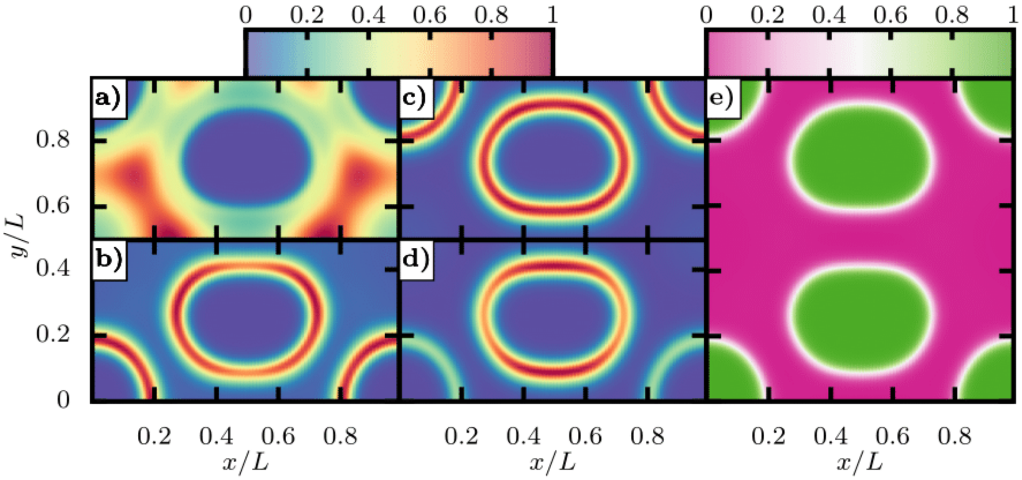

Figure 3.8: Normalized distribution of chain junctions, $P_c q_c(\boldsymbol{r}, \lambda_c N_{\mathrm{A,ref}}) q_c^\dagger(\boldsymbol{r}, N_{\mathrm{B}})$, where $P_c = \mathrm{SZ}(\lambda_c; k)$ for a) $\lambda_c = 8.33 \times 10^{-2}$, b) $\lambda_c = 0.45$, c) $\lambda_c = 1.133$, d) $\lambda_c = 5.383$ on the $z = 0$ plane of the A15 phase. The spatially-varying volume fraction of A-monomers $\phi_{\mathrm{A}}(\boldsymbol{r})$ is shown alongside in e). The parameters are $k = 2$, $f = 0.30$ and $\chi \langle N_c \rangle = 40$.

The behavior observed in Figure 3.8a-d is consistent with the notion of inter- and intra-domain chain segregation. In a study of binary blends of conformationally symmetric diblock copolymers by Liu *et al.* [47], the two segregation effects were identified to be responsible for the formation of a number of different FK phases. As detailed in

Ref. [47], chain segregation occurring at the interfaces facilitates the assembly of non-spherical domains, whereas inter-domain segregation encourages micelles of various sizes to form. We note that the extent of chain segregation will not be as pronounced here as what is seen in binary blends since the degrees of dispersity being considered are not as extreme (i.e. $Đ\,(N_{\mathrm{A},c}) = 1.125$ to 1.5).

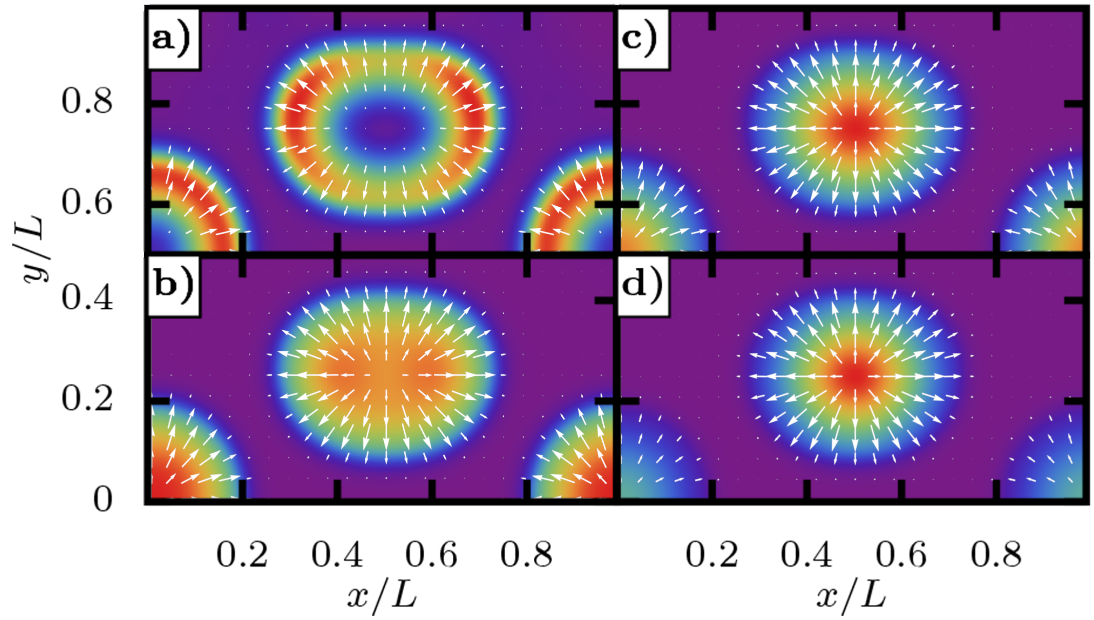

Figure 3.9: Spatial distribution of A-block chain ends where P_c is given by the Schulz-Zimm distribution for a) $\lambda_c = 0.45$, b) $\lambda_c = 1.133$, c) $\lambda_c = 2.163$, and d) $\lambda_c = 5.383$ on the $z = 0$ plane of the A15 phase. The white vectors depict the average orientation of the A monomers [3]. The parameters are $k = 2$, $f = 0.30$ and $\chi \langle N_c \rangle = 40$.

To further elucidate the influence of dispersity on the spatial organization of polymers, we consider the distribution of A-block chain ends $P_c q_c^{\dagger}(\boldsymbol{r}, N_c)$ and the mean local orientation of A-segments given by [3],

$$\begin{aligned} \boldsymbol{t}_{\mathrm{A},c}\left(\boldsymbol{r}\right) &= \left\langle \sum_{i}^{n_c} v_{\mathrm{A}} \int_{I_{\mathrm{A},c}} ds\, \boldsymbol{T}_{i,c}\left(s\right) \delta\left(\boldsymbol{R}_{i,c}(s) - \boldsymbol{r}\right) \right\rangle \\ &= \frac{P_c}{\langle v_c \rangle Q_c} \frac{b_{\mathrm{A}}}{6} \left[v_{\mathrm{A}} \int_{I_{\mathrm{A},c}} ds\, q_c(\boldsymbol{r}, s) \nabla q_c^{\dagger}(\boldsymbol{r}, N_c - s) - q_c^{\dagger}(\boldsymbol{r}, N_c - s) \nabla q_c(\boldsymbol{r}, s) \right]. \end{aligned} \tag{3.2}$$

Here, the vector $\boldsymbol{T}\left(s\right)$ represents to the orientation of the s^{th} segment (directed from A- to B-end). For the same parameters as Figure 3.8, we show the distribution of free A-block ends as the density plots for different values of λ_c in Figure 3.9. The overlaying vectors indicate the projection of $\boldsymbol{t}_{\mathrm{A},c}\left(\boldsymbol{r}\right)$ onto the $z = 0$ plane. We see that the ends of polymers with shorter A-blocks are located closest to the interface. From where their free ends are concentrated, the mean segment orientation suggests that the A-blocks extend radially outwards towards the nearby B-matrix. As λ_c increases, the mass of chain ends moves deeper into the center of the micelles. From the centers, the longer molecules tend to extend out to the flatter parts of the interface where the concentration of their chain junctions is higher. The observed behavior is again consistent with the idea of intra-domain segregation. Polymers with longer A-blocks are partitioned to the domain interiors, filling the space furthest from the interface. Shorter chains placed closer to the interface are allowed to relax. There are also signs of inter-domain segregation. The free A-block ends of the longer molecules are located almost exclusively within the larger domains.

In the current chapter, we examined how dispersity impacts the formation of complex spherical phases in conformationally asymmetric diblock copolymers. The A-block dispersity was given by either the Poisson or SZ distributions. For both cases, we found that the FK σ phase can occur at a lower degree of conformational asymmetry than in monodisperse systems. Our findings help reconcile some of the discrepancies between theoretical predictions and the experimental results of Schulze *et al.* [2]. We observed that increasing the dispersity (i.e. larger dispersity indices) would enhance the stability of the complex phases. For the SZ distribution in particular, a variety of FK phases other than the σ phase becomes accessible when ε is increased. We also investigated the effects of macro-phase separation, which revealed that the coexistence regions between two spherical phases are negligible. Lastly, the spatial arrangement of polymer chains within the self-assembled structures was examined. We found that the formation of non-classical packings arises from inter- and intra-domain chain segregation effects. The result is consistent with earlier theoretical works on binary mixtures by other authors [47].

Chapter 4

Effect of molecular weight distribution shape on phase behavior of diblock copolymers

In the previous chapter, we assumed that the dispersity is described by the commonly used Poisson and SZ distributions. In this chapter, we will investigate the phase behavior of diblock copolymers with experimentally measured molecular weight distributions (MWDs). We first present a general procedure to treating distributions specified by many molecular weights in numerical SCFT calculations. The method is subsequently applied to the samples from the experiments of the Fors group [4]. The MWDs of these samples were prepared specifically to have nearly identical A-block dispersity indices $Đ(N_{\mathrm{A},c})$ and different skewness. For a given A-volume fraction f, we predict that the equilibrium structure can depend on the skewness, consistent with the experiments. The results highlight the importance of the MWD shape on the self-assembly process.

4.1 Modeling experimental molecular weight distributions

Disperse synthetic polymer samples may contain thousands of different molecular weights. Each molecular weight corresponds to a particular degree of polymerization, or equivalently, chain contour length N_c. A large number of N_c poses a problem for numerical SCFT calculations. As discussed in Section 2.1.2, the most computationally expensive step is solving the forward and backward end-integrated propagators $q_c(\boldsymbol{r}, s)$ and $q_c^\dagger(\boldsymbol{r}, s)$. Since the propagators need to be determined for each polymer type c, the computation time would grow with the number of polymeric species. To make matters worse, the system will generally include polymers that are much longer than the mean value, resulting in longer computing time because the number of steps from discretizing the chain contour length is proportional to N_c. To circumvent such problems, we present below a general approach to handling distributions that contain a large number of possible molecular weights in numerical SCFT, using an example from experimental data courtesy of the Fors group [4].

An experimental MWD is specified by the data set $\{M_c, w_c\}_{c=1}^{M^{(\mathrm{src})}}$ where w_c is the weight or mass fraction of polymer chains with molecular weight M_c,

$$w_c = \frac{\text{mass of type}\, c\, \text{polymers}}{\text{total mass of mixture}} = \frac{m_c M_c}{\sum_{c'} m_{c'} M_{c'}}, \tag{4.1}$$

where m_c is the number of moles. The corresponding number fractions are given by,

$$\begin{aligned} P_c^{(\mathrm{src})} =& \frac{m_c \times N_{\mathrm{Avog}}}{\sum_{c'} m_{c'} \times N_{\mathrm{Avog}}} = \frac{m_c}{\sum_{c'} m_{c'}} = \frac{m_c}{\sum_{c''} m_{c''} M_{c''}} \frac{\sum_{c''} m_{c''} M_{c''}}{\sum_{c'} m_{c'}} \\ =& \frac{w_c}{M_c} \left(\frac{\sum_{c'} m_{c'}}{\sum_{c''} m_{c''} M_{c''}} \right)^{-1} = \frac{w_c}{M_c} \left(\sum_{c'} \frac{m_{c'}}{\sum_{c''} m_{c''} M_{c''}} \right)^{-1} \\ =& \frac{w_c / M_c}{\sum_{c'} w_{c'} / M_{c'}}, \end{aligned} \tag{4.2}$$

with N_{Avog} denotes the Avogardo's number. To convert from molecular mass to relative degree of polymerization or chain length $\lambda_c^{(\mathrm{src})}$, we use the relationship:

$$\lambda_c^{(\mathrm{src})} = \frac{M_c}{\langle M_c \rangle} = \frac{N_c}{\langle N_c \rangle}. \tag{4.3}$$

We assume that the degree of polymerization is proportional to the molecular weight with the proportionality constant being independent of molecular weight in writing Eq. (4.3). As a minor technical detail, the data values are arranged in increasing order of $\lambda_c^{(\mathrm{src})}$, i.e. $\lambda_c^{(\mathrm{src})} \leq \lambda_{c+1}^{(\mathrm{src})}$.

For discrete distributions, the SCFT equations involving the number fractions P_c can be generally expressed as,

$$\sum_c g(\lambda_c) P_c, \tag{4.4}$$

where $g(\lambda_c)$ is some function of λ_c. The above equation can be re-written for convenience as,

$$\sum_{c=1}^{M^{(\mathrm{src})}} g\left(\lambda_{c'}^{(\mathrm{src})}\right) P_{c'}^{(\mathrm{src})} = \int_1^{M^{(\mathrm{src})}} dc\, g\left(\lambda^{(\mathrm{src})}(c)\right) P^{(\mathrm{src})}(c), \tag{4.5}$$

where,

$$
\begin{aligned}
\lambda^{(\mathrm{src})}(c) &= \sum_{c'=1}^{M^{(\mathrm{src})}} \lambda_{c'}^{(\mathrm{src})} \mathcal{I}(c;c'), \\
P^{(\mathrm{src})}(c) &= \sum_{c'=1}^{M^{(\mathrm{src})}} P_{c'}^{(\mathrm{src})} \mathcal{I}(c;c'),
\end{aligned}
\tag{4.6}
$$

with the step function $\mathcal{I}(c;c')$ being,

$$
\mathcal{I}(c;c') = \begin{cases} 1 & |c-c'| \leq \frac{1}{2} \\ 0 & \text{otherwise} \end{cases} . \tag{4.7}
$$

We next take the crucial step of approximating $\lambda^{(\mathrm{src})}(c)$ and $P^{(\mathrm{src})}(c)$ that are defined by the data set $\left\{\lambda_c^{(\mathrm{src})}, P_c^{(\mathrm{src})}\right\}_{c=1}^{M^{(\mathrm{src})}}$ with the functions, $\lambda(c)$ and $P(c)$, respectively. The two functions, $\lambda(c)$ and $P(c)$, are determined via polynomial regression on the data sets $\left\{c, \lambda_c^{(\mathrm{src})}\right\}_{c=1}^{M^{(\mathrm{src})}}$ and $\left\{c, P_c^{(\mathrm{src})}\right\}_{c=1}^{M^{(\mathrm{src})}}$, respectively. The step amounts to writing,

$$
\int_1^{M^{(\mathrm{src})}} dc\, g\left(\lambda^{(\mathrm{src})}(c)\right) P^{(\mathrm{src})}(c) \approx \int_1^{M^{(\mathrm{src})}} dc\, g(\lambda(c))\, P(c) . \tag{4.8}
$$

Ideally, the replacements would satisfy $\lambda(c) = \lambda_c^{(\mathrm{src})}$ and $P(c) = P_c^{(\mathrm{src})}$ for any integer c. For the example data, we show $\lambda(c)$ and $P(c)$ from regression in Figures 4.1a and 4.1b, respectively. We found that a higher quality fit for $P(c)$ can be more easily obtained by using two separate polynomial functions joined together at a common value of c as opposed to a single polynomial for the whole data set.

To estimate the quality of the continuous approximation, we calculate the first three moments directly from the data and via right-hand side of Eq. (4.5) using the polynomials from linear regression, as tabulated in Table 4.1. The relative difference across the moments is less than 1%. Similar to our treatment of the continuous SZ

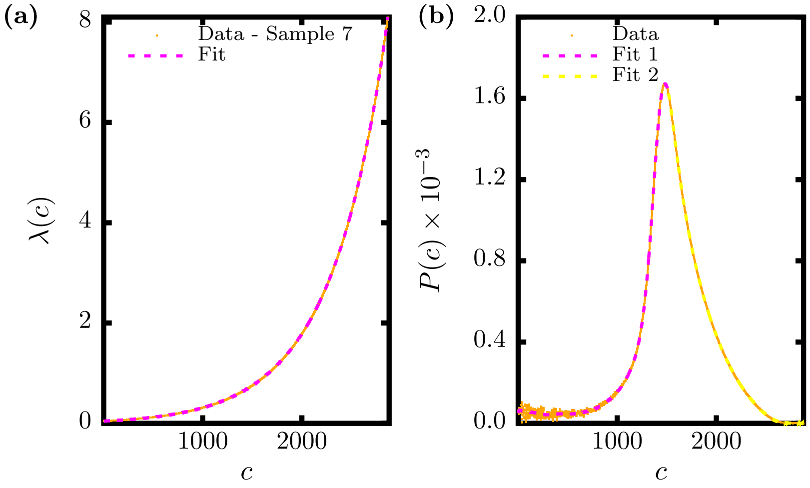

Figure 4.1: Polynomial fits for the data of Sample 7: (a) $\lambda(c)$ using $\left\{c, \lambda_c^{(\mathrm{src})}\right\}_{c=1}^{M^{(\mathrm{src})}}$ and (b) $P^{(\mathrm{src})}(c)$ using $\left\{c, P_c^{(\mathrm{src})}\right\}_{c=1}^{M^{(\mathrm{src})}}$.

Sample 7	$\langle\lambda_c\rangle$	$\langle\lambda_c^2\rangle$	$\langle\lambda_c^3\rangle$
(1) Data	1.	1.442	2.94
(2) Integral	1.	1.44	2.926
(3) Gauss-Legendre quadrature	0.982	1.432	2.932

Table 4.1: The first three moments of Sample 7 (1) calculated directly from the data $\left\{\lambda_c^{(\mathrm{src})}, P_c^{(\mathrm{src})}\right\}_{c=1}^{M^{(\mathrm{src})}}$, as well as from integrating the polynomial fits $\lambda(c)^n P(c)$ (2) exactly and (3) using the Gauss-Legendre quadrature.

distribution in Section 3.2, we will use the Gauss-Legendre quadrature to evaluate expressions in the form of Eq. (4.5). For an $M^{(\mathrm{gl})}$-point quadrature, we have,

$$\int_{1}^{M^{(\mathrm{src})}} dc\, g\left(\lambda\left(c\right)\right) P\left(c\right) \approx \sum_{c}^{M^{(\mathrm{gl})}} g\left(\lambda_c^{(\mathrm{gl})}\right) P_c^{(\mathrm{gl})}, \tag{4.9}$$

where the relative chain lengths representing the abscissas reads,

$$\lambda_c^{(\mathrm{gl})} = \lambda\left(\frac{M^{(\mathrm{gl})}-1}{2} x_c^{(\mathrm{gl})} + \frac{M^{(\mathrm{gl})}+1}{2}\right). \tag{4.10}$$

Here, $x_c^{(\mathrm{gl})}$ is the c^{th} root of the Legendre polynomial of order $M^{(\mathrm{gl})}$, denoted as $\mathcal{P}\left(x; M^{(\mathrm{gl})}\right)$. The associated number fractions are given by,

$$P_c^{(\mathrm{gl})} = P\left(\frac{M^{(\mathrm{gl})}-1}{2} x_c^{(\mathrm{gl})} + \frac{M^{(\mathrm{gl})}+1}{2}\right) \times \left[\frac{2}{1-\left(x_c^{(\mathrm{gl})}\right)^2}\left(\frac{d}{dx}\mathcal{P}\left(x; M^{(\mathrm{gl})}\right)\Big|_{x_c^{(\mathrm{gl})}}\right)^{-2}\right], \tag{4.11}$$

noting that the quadrature weight corresponding to term in the square brackets above has been included in the definition of $P_c^{(\mathrm{gl})}$. We calculate the first three moments using the 16-point quadrature illustrated Figure 4.2 and tabulate the results in Table 4.1. The relative difference from the exact values computed from the data is less than 2%. For completeness, the set of values for $\left\{\lambda_c^{(\mathrm{gl})}, P_c^{(\mathrm{gl})}\right\}$ is explicitly given in Table F.3 of Appendix F. The outlined procedure effectively reduces the representation of the MWD with thousands of species to a small number of points in numerical calculations.

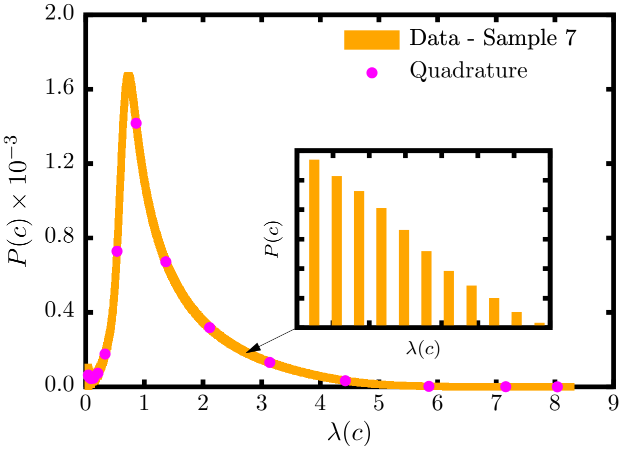

Figure 4.2: Plot of the relative chain lengths and corresponding number fractions (without including the quadrature weights) from a 16-point Gauss-Legendre quadrature in magenta, alongside the experimental values for Sample 7 in orange.

4.2 Effect of skewness

We apply our numerical procedure to three samples, 4, 7 and 15, from the experiments by the Fors group, in order to examine how MWDs with equal dispersity indices and differing skewness affect the phase behavior of diblock copolymers. The polynomial fits for $\lambda(c)$ and $P(c)$, as well as the moments calculated from the data and Gauss-Legendre quadrature for Sample 4 and 15 are given in Appendix F. Sample 4 is regarded experimentally as monodisperse, while Sample 7 and 15 correspond to the MWDs with positive and negative skewness, respectively. In Figure 4.3a, we plot the phase diagram as a function of the A-volume fraction f and number-averaged segregation strength $\chi \langle N_c \rangle$ for the distribution of A-block lengths describing Sample 4, 7 and 15 in green, orange and blue, respectively. Following the experiments, we assume the B-block length is uniform across all molecules. The Kuhn lengths are also taken to be identical, $b_{\mathrm{A}} = b_{\mathrm{B}} = b$. For ease of comparison, we include the experimental phase diagram from Ref. [4] as Figure 4.3b.

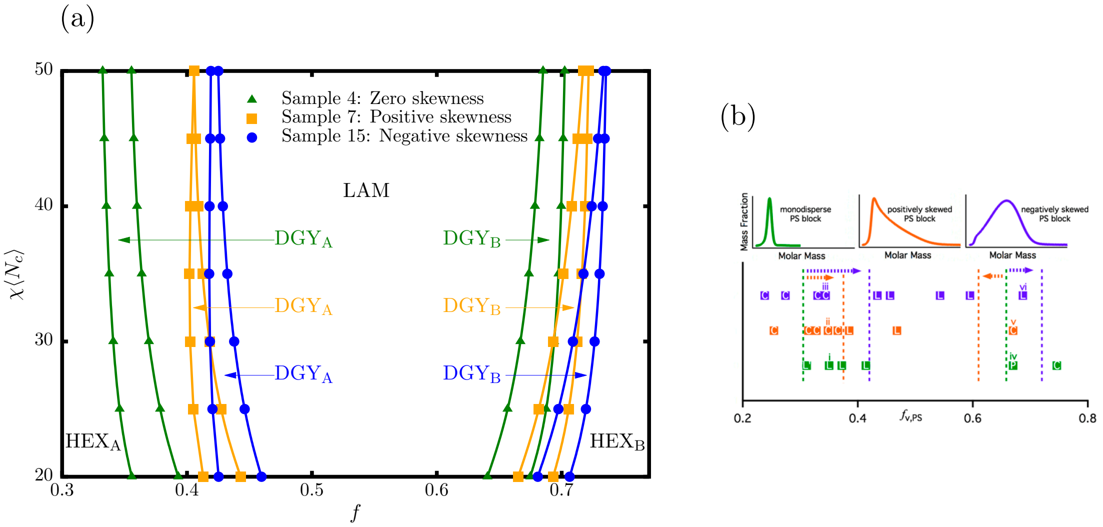

Figure 4.3: (a) Phase diagram as a function of the number-averaged segregation strength $\chi\langle N_c\rangle$ and A-volume fraction f where the distributions of A-block lengths are sourced from the data of Sample 4 (green), Sample 7 (orange) and Sample (15). (b) Experimental phase diagram borrowed from Ref. [4].

We find that the same sequence of equilibrium phases $\mathrm{HEX_A} \rightarrow \mathrm{DGY_A} \rightarrow \mathrm{LAM} \rightarrow \mathrm{DGY_B} \rightarrow \mathrm{HEX_B}$ is predicted as f increases for all three samples. The suffix α refers to the minority domain being composed of α-monomers. This is to be compared with the experimental sequence $\mathrm{HEX_A} \rightarrow \mathrm{LAM} \rightarrow \mathrm{HEX_B}$ [4]. It is noted that the gyroid phase is missing from the experiments [4]. The number of samples prepared experimentally to the explore the parameter space of f is quite small. Considering the narrow window of the gyroid phase, the discrepancy could be simply a matter of insufficient number of sampling points. Gentekos *et al.* also reported a hexagonally-perforated lamellar phase for the monodisperse samples on the $f > 0.5$ side of the phase diagram. We found that the perforated lamella does not appear as an equilibrium morphology in the phase space of interest. There may be two possible explanations for the disagreement. First, experimentally observed perforated lamellar phases in monodisperse diblock copolymers are often metastable states that will anneal to the stable double gyroid structure [77]. A second possible reason could be that the hexagonally-perforated lamella corresponds instead to a lamellar phase coexisting with hexagonally close-packed cylinders. For instance, the scattering data of the disperse sample reported to exhibit perforated lamellar morphology was noted to be also consistent with a coexisting LAM+HEX state in the experiments of Lynd *et al.* [38]. Given that Sample 4 is designed experimentally to be the most monodisperse out of the three being considering, we suspect the former to be more likely the case.

Besides the lack of the double gyroid phase, the agreement between the experimental and theoretical results is qualitatively good for the portion of the phase diagram where $f < 0.5$. SCFT predicts that the phase boundaries collectively move to higher A-volume fractions relative to the monodisperse sample for both the positively- and negatively-skewed distributions (Sample 7 and 15), with the shift being greater for the latter. From Figure 4.3b, we see the same behavior is seen experimentally in Ref. [4]. The shift in the phase boundaries arising from A-block dispersity has been observed in other theoretical [26, 78, 27, 29] and experimental works [36]. Non-uniformity in the block lengths lowers the entropic cost of extending the disperse blocks. Thus, stretching the A-blocks become easier, and by relation, stretching the B-blocks become more difficult. The A/B interface will develop a tendency to adopt configurations that are curved towards the A-domains as to relax the stretching of the B-component. For example in Figure 4.3a, hexagonally-packed cylinders are preferred by Sample 7 and 15 at A-volume fractions ($0.35 \lesssim f \lesssim 0.40$) where the planar lamellar phase would normally occur in the monodisperse system. The effect of dispersity is similar to that of conformational asymmetry when $\varepsilon > 1$ discussed in Chapter 3.

The reduced entropic penalty for chain-stretching will also lead to larger domain sizes. In Figure 4.4a, we plot the equilibrium lamellar period L_{LAM} as a function of f for the three samples at an average segregation strength of $\chi \langle N_c \rangle = 50$. We indeed find that the domain spacing of the lamellar phase formed by the disperse Sample 7 and 15 is consistently larger than the monodisperse counterpart. The same trend is observed experimentally by the Fors group [4]. Comparing the periods between only the skewed samples with experiments is difficult given how similar the values are.

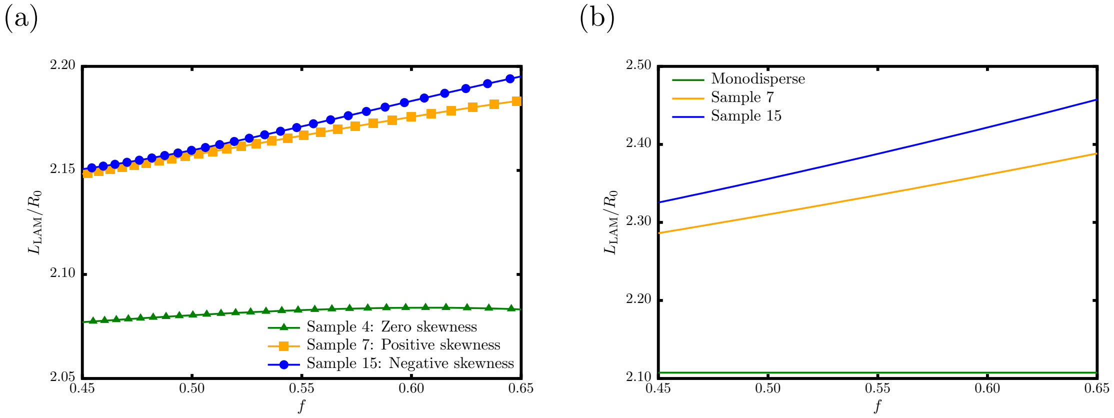

Figure 4.4: Equilibrium lamellar period L_{LAM}/R_0 as a function of the A-monomer volume fraction obtained via (a) numerical SCFT and (b) Eq. (4.18) from strong-segregation theory where $R_0 = \sqrt{\langle N_c \rangle} b$ and $\chi \langle N_c \rangle = 50$ for Sample 4 (green), Sample 7 (orange) and Sample 15 (blue).

4.2.1 Analysis via strong-segregetion theory

To estimate the reduction to the entropic stretching energy due to dispersity, we briefly appeal to strong segregation theory (SST) [24, 64, 6, 17], which is an analytic treatment of SCFT suitable at large segregation strengths. Within SST, the dimensionless free energy per chain can be written as a sum of three terms,

$$F_{\text{SST}} = F^{(\text{int})} + F_{\text{A}}^{(\text{str})} + F_{\text{B}}^{(\text{str})} \tag{4.12}$$

where $F^{(\mathrm{int})}$ is the interaction energy associated with the contacts between unlike monomers occurring in the narrow interfacial regions. The entropic costs of stretching the A- and B-blocks are denoted $F_{\mathrm{A}}^{(\mathrm{str})}$ and $F_{\mathrm{B}}^{(\mathrm{str})}$, respectively. Restricting our analysis to the lamellar phase, the interfacial energy reads,

$$F^{(\mathrm{int})} = \frac{2b\left\langle N_c \right\rangle}{L}\sqrt{\frac{\chi}{6}}, \tag{4.13}$$

where L denotes the period. The entropic stretching terms are given by the theory of polymer brushes [78, 79],

$$F_{\mathrm{A}}^{(\mathrm{str})} = \frac{f\pi^2 L^2}{32b^2\left\langle N_c \right\rangle}\mathcal{S}_{\mathrm{A}}, \tag{4.14}$$

and

$$F_{\mathrm{B}}^{(\mathrm{str})} = \frac{(1-f)\pi^2 L^2}{32b^2\left\langle N_c \right\rangle}\mathcal{S}_{\mathrm{B}}. \tag{4.15}$$

Here, $\mathcal{S}_\alpha$ represents the reduction factor to the stretching energy arising from α-block dispersity,

$$\mathcal{S}_\alpha = \int d\lambda_\alpha \left[1 - \mathrm{CDF}_\alpha\left(\lambda_\alpha\right)\right]^3. \tag{4.16}$$

The cumulative distribution function for the probability distribution of the relative α-block lengths, which we denote $\overline{P}_\alpha\left(\lambda_\alpha\right)$, is,

$$\mathrm{CDF}_\alpha\left(\lambda_\alpha\right) = \int_{\min \lambda_\alpha}^{\lambda_\alpha} d\lambda'_\alpha \overline{P}_\alpha\left(\lambda'_\alpha\right), \tag{4.17}$$

where $\lambda_\alpha^{\min}$ is the minimum value which $\overline{P}_\alpha\left(\lambda_\alpha\right)$ is defined for. The factor $\mathcal{S}_\alpha$ characterizes how disperse blocks can packed in a more efficient manner such as by using longer chains to pervade the spaces more distant from the A/B interface [79]. For monodisperse blocks, the reduction factor evaluates to $S_\alpha = 1$. Lastly, we determine the equilibrium period by minimizing the free energy Eq. (4.12), which results in,

$$\frac{L_{\mathrm{LAM}}}{R_0} = \frac{(L_{\mathrm{mono}}/R_0)}{\left(f\mathcal{S}_{\mathrm{A}} + (1-f)\mathcal{S}_{\mathrm{B}}\right)^{1/3}}, \tag{4.18}$$

where L_{mono} is the optimal period for a pure system given by the classic expression [64]:

$$\frac{L_{\mathrm{mono}}}{R_0} = 2\left(\frac{8\chi\left\langle N_c\right\rangle}{3\pi^3}\right)^{\frac{1}{6}}. \tag{4.19}$$

To calculate cumulative distribution function from the sample data, we use the following integral relationship,

$$\int dc\, P(c) = \int d\lambda\, P(c(\lambda))\,\frac{dc(\lambda)}{d\lambda}, \tag{4.20}$$

to write Eq. (4.17) in terms of the polynomial fit $P(c)$,

$$\mathrm{CDF}_{\mathrm{A}}(\lambda_{\mathrm{A}}) = \int_{\lambda_1^{(\mathrm{src})}}^{\lambda_{\mathrm{A}}} d\lambda'\,\overline{P}_{\mathrm{A}}(\lambda') = \int_{\lambda_1^{(\mathrm{src})}}^{\lambda_{\mathrm{A}}} d\lambda'\, P(c(\lambda'))\,\frac{dc(\lambda')}{d\lambda}. \tag{4.21}$$

The inverse function $c(\lambda)$ can be determined by fitting the data set $\left\{\lambda_c^{(\mathrm{src})}, c\right\}_{c=1}^{M^{(\mathrm{src})}}$. We calculate S_{A} for the samples with positive and negative skewness to be 0.52 and 0.43, respectively.

In Figure 4.4b, we plot the equilibrium lamellar domain size given by Eq. (4.18) for the two disperse samples alongside the monodisperse system. Although L_{LAM} predicted by SST is systemically larger than what numerical SCFT calculates presumably due to the over-estimated degree of chain-stretching, the general trends are the same. The domain spacing is larger for the negatively-skewed than positively-skewed distribution, which we can attribute from Eq. (4.18) to the entropic cost of stretching the A-blocks being lower for Sample 15 ($S_{\mathrm{A}} = 0.43 < 0.52$). The larger reduction in stretching energy predicted by SST also implies that the tendency for the interface to curve towards the disperse A-blocks will be greater in Sample 15 than 7. This explains why the shift in the phase boundaries to higher A-volume fractions is more pronounced for Sample 15 in Figure 4.3a.

There is an additional effect that our SST analysis does not incorporate that may change the tendency of adopting curved interfaces. The effect is when polymers with extremely asymmetric block compositions become dislodged from the A/B interface and reside completely in the domain of its majority segments. Similar behavior was seen in the previous chapter (see Figure 3.8). For $f < 0.5$, short A-block, long B-block molecules will be susceptible to being dislocated from the interface and situated in the B-matrix. This can drive the system to form interfaces with higher curvature towards the minority A-domain. The effect would be stronger in Sample 15 than 7. In a negatively-skewed distribution, there will be a larger population of shorter A-block polymers by virtue of its longer tail on the left side of the mean ($\lambda < 1$). This is consistent with the LAM $\rightarrow$ DGY$_{\mathrm{A}}$ $\rightarrow$ HEX$_{\mathrm{A}}$ transitions observed in Sample 15 than 7 with a larger f. Similarly for $f > 0.5$, long A-block, short B-block polymers will have a propensity to detach from the interface, swelling the A-matrix and promoting the interface to curve towards the B-domains [36, 80, 25]. The effect is expected to be more pronounced in Sample 7. A greater abundance of longer A-block chains is available in a positively-skewed distribution that would have a longer tail on the right side of the mean ($\lambda > 1$).

4.3 Inclusion of B-block dispersity

One other discrepancy between the experimental and our theoretical results is the location of the phase boundaries relative to the monodisperse sample for $f > 0.5$. SCFT continues to predict a shift of the order-order transitions to larger values of f regardless of the skewness. We see the same trend is also observed by the Fors group for Sample 15 from Figure 4.3b. However, the LAM → HEX_B transition is experimentally reported to occur at a lower f for the positively-skewed than monodisperse sample. There are a few possible explanations for the disagreement. For one, the number of samples used to probe the parameter space of $f > 0.5$ is sparser than $f < 0.5$, which would make precisely resolving the phase boundary more difficult. Another possibility could be that the B-blocks have a small degree of dispersity, which is an opportunity to explore its effects in the current section. Up until now, we have only considered dispersity occurring in the A-blocks.

Since we do not expect the B-block dispersity to be large in keeping with experiments, the Poisson distribution is employed to model its dispersity. We choose $\mu = 8$ which yields $Đ(N_{\text{B},c}) = 1.125$. The overall dispersity index $Đ(N_c)$ differs slightly from monodisperse B-blocks and remains within the experimental range of 1.02-1.21 [4]. We furthermore assume that the distribution of the two blocks are independent of one another. Therefore, the number fraction of polymers with A- and B-block lengths, $N_{\text{A},c} = \lambda_{\text{A},c} N_{\text{A,ref}}$ and $N_{\text{B},c} = \lambda_{\text{B},c} N_{\text{B,ref}}$, respectively, will be given by the joint probability,

$$P_c = P_{\text{A},c} \times P_{\text{B},c}. \tag{4.22}$$

The set of values $\{P_{\alpha,c}\}$ characterizes the distribution of α-block lengths.

We plot in Figure 4.5 the phase diagram analogous to Figure 4.3a except with the introduction of B-block dispersity. In the same fashion as Section 3.1, the Poisson distribution is numerically represented using the coarse-graining scheme detailed in Appendix E with $M_\lambda = 4$. As a technical aside, the values of $\lambda_{\mathrm{B},c}$ after coarse-graining are further rounded in order to ensure that the number of steps discretizing the contour length is an integer for both the A- and B-blocks when using a common step size. We tabulate the values for $\lambda_{\mathrm{B},c}$ and $P_{\mathrm{B},c}$ in Table 4.2 for completeness. Due to numerous chain compositions ($M^{(\mathrm{gl})} \times M_\lambda \gtrsim 60$), we consider only the lamellar and cylindrical phases in the calculation to assess the effects of introducing B-block dispersity.

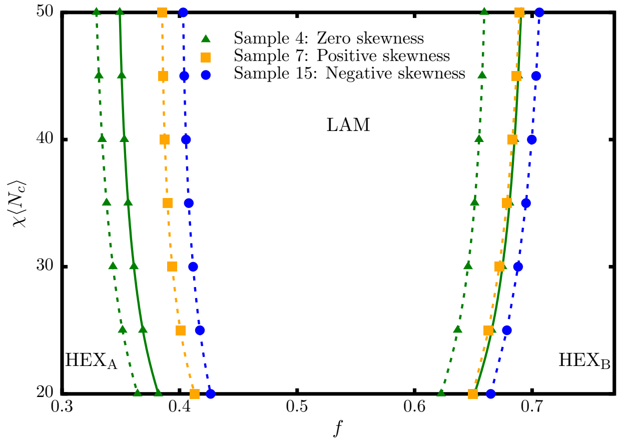

Figure 4.5: Phase diagram as a function of the number-averaged segregation strength $\chi \langle N_c \rangle$ and A-volume fraction f where the distributions of A-block lengths are sourced from the data of Sample 4 (green), Sample 7 (orange) and Sample 15 (blue), while the B-block lengths are assumed to obey the Poisson distribution $\mathrm{Pois}(\lambda; \mu)$ with $\mu = 8$ (dashed lines) and monodisperse (solid lines).

$\lambda_{\mathrm{B},c}$	1.6	1.2	0.7	0.3
$P_{\mathrm{B},c}$	0.1046	0.4387	0.4140	0.0427

Table 4.2: Values for the relative B-block lengths $\lambda_{\mathrm{B},c}$ and the corresponding probabilities $P_{\mathrm{B},c}$, from the coarse-graining procedure applied to the Poisson distribution $\mathrm{Pois}\,(\lambda;\mu)$ with $\mu = 8$.

With disperse B-blocks, the phase boundaries as a whole migrate to smaller A-volume fractions compared to what is seen in Figure 4.3a. We do find that the LAM → $\mathrm{HEX}_{\mathrm{B}}$ for the positively-skewed sample now takes places at values of f lower than the monodisperse sample assuming uniform B-blocks. To be consistent, the same phase transition will also move to smaller A-volume fractions when B-block dispersity is included for Sample 4. This unfortunately leaves us with the same discrepancy as before. The change to the order-order transition curves from introducing B-block dispersity agrees with our earlier SST analysis. The increased tendency to curve the interface towards the A-domains stems from the enhanced reduction in the stretching energy due to the lowered cost of extending the disperse A-blocks. When both the A- and B-blocks are disperse, the entropic penalty for stretching either blocks will be reduced, albeit to different extents. The preference to stretch one block more than the other and form interfaces more curved towards the A-domains will therefore decrease, restoring the phase boundaries to lower values of f.

In the current chapter, we examined the phase behavior of diblock copolymers with experimentally determined MWDs . A general procedure for treating experimental MWDs in numerical SCFT was first provided. Since current polymer synthesis and processing techniques offer precise control over the width, skewness and even shape of a MWD [41, 42, 46], we anticipate that the outlined method will be useful for future studies on dispersity. The protocol was applied to samples from the experiments by the Fors group [4]. By design, the average molecular weight and dispersity indices of the samples are nearly identical, whereas the skewness varies. We find that samples with positive and negative skewness can produce different equilibrium phases at a given A-volume fraction. Qualitatively, the predicted differences in the phase behavior between the samples agrees well with the experimental results of the Fors group [4]. The findings here emphasize the importance of the MWD shape and the need for other statistical measures to complement the dispersity index when studying the phase behavior of disperse block copolymers.

Chapter 5

Effect of skewness on the formation of complex spherical phases

In this chapter, we investigate how the shape of a MWD affects the formation of complex spherical phases in diblock copolymers, focusing on the interplay between the dispersity index and skewness. For computational convenience, the polymers are modeled as discrete freely jointed chains (FJCs) instead of continuous Gaussian chains. Some of the numerical advantages offered by the FJC model were discussed in Section 2.4.1. We first examine differences in the phase behavior between the two chain models for both monodisperse and disperse systems. In monodisperse systems, the FK σ phase is predicted to occur at a lower degree of conformational asymmetry for FJCs. When dispersity is introduced, chain segregation favoring the formation of complex phases occurs in both chain models. We will explore the phase behavior of spherical phases for a variety of MWD shapes. The skewness, Eq. (2.74), is identified to be a key parameter regulating the equilibrium selection of spherical packings. In particular, we find that MWDs with larger positive skewness render the C14 and C15 phases accessible. Decreasing the skewness subsequently favors the formation of the A15 and σ phases. We lastly examine the roles played by polymers with different chain lengths in the self-assembly of spherical phases.

5.1 Schulz-Zimm distribution revisited

We start by considering monodisperse diblock copolymers modeled as FJCs. This facilitates a brief discussion on some of the differences from the continuous Gaussian chain model. In Figure 5.1, we plot the phase diagram as a function of the segregation strength χN and A-volume fraction f with the conformational asymmetry set to $\varepsilon = 2$. From hereinafter, the range of the non-bonded interaction will be assumed to be the same as the Kuhn length of the A-monomers, $\sigma_{\mathrm{fr}} = b_{\mathrm{A}}$. We adjust the length of the B-block while keeping $N_{\mathrm{A}} = 12$ to tune f. This is opposed to fixing the total degree of polymerization, $N = N_{\mathrm{A}}/f$, as f is changed. For the FJC model, the distinction will yield slightly different results since the free energy [see Eq (2.49)] depends on both χ and N, rather than only on the product χN. We find the sequence of equilibrium phases is identical to that predicted for continuous Gaussian chains. As f decreases, one encounters HEX$\rightarrow \sigma \rightarrow$ BCC $\rightarrow$ $\mathrm{S_{cp}}$ $\rightarrow$ DIS. However, the BCC region is narrower here, while in exchange the σ phase spans a larger range of f. The enlarged σ-phase region is related to the fact that the complex phases start to form at a lower degree of conformational asymmetry for FJCs. In monodisperse systems, the σ phase occurs when $\varepsilon \gtrsim 1.5$ for continuous Gaussian chains [47], whereas its appearance can be before $\varepsilon = 1.5$ for discrete FJCs. Increasing ε beyond the critical value at which the σ phase initially appears will widen its window of stability. Therefore, we can expect that the σ-phase region will be larger for FJCs at the same degree of conformational asymmetry.

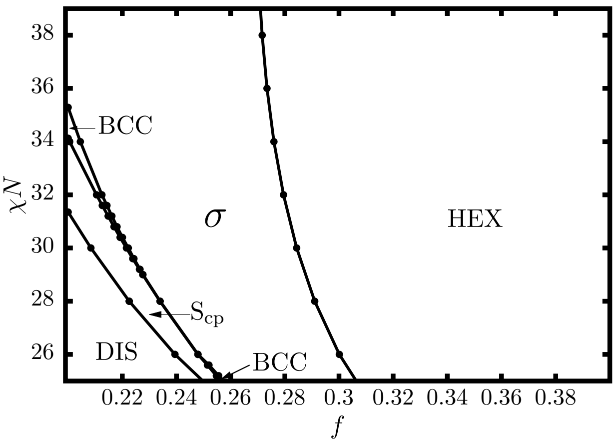

Figure 5.1: Phase diagram for monodisperse freely jointed chains as a function of the segregation strength χN and A-volume fraction f with A-block length $N_{\mathrm{A}} = 12$ and $\varepsilon = 2$.

We plot the free energy density difference between the BCC and two other phases (HEX and σ) as a function of ε for monodisperse continuous Gaussian and discrete FJCs in Figure 5.2a and b, respectively. The formation of the σ phase indeed takes place at a smaller value of $\varepsilon = 1.5$ for FJCs than $\varepsilon = 1.8$ for Gaussian chains. In Figure 5.3, we plot the spatially-varying A-volume fraction for the lamellar phase as a function of the x-position for continuous Gaussian (blue) and FJCs (orange) at two different values of ε. Due to the finite range of the non-bonded interactions [see Eq. (2.50)], the A/B interface is wider for FJCs, consistent with Ref. [71]. The greater overlap of unlike monomers indicates that the segregation between the A- and B-blocks is weaker than in continuous Gaussian chains at a given value of $\chi \langle N_c \rangle$. While we have performed the analysis for only the lamellar phase, the same effect applies to other phases. Consequently, the phase boundaries of monodisperse FJCs resemble largely those of Gaussian chains except shifted to higher values of $\chi \langle N_c \rangle$ [71].

The progression from lamellar to cylinders and lastly to spheres will occur at block compositions closer to $f = 0.5$. Since spherical phases can already form at larger values of f, a lower value of ε is needed to access the σ phase for FJCs with finite-range interactions.

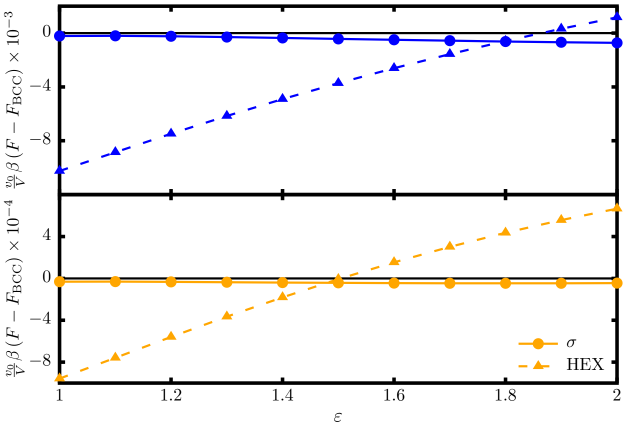

Figure 5.2: Difference in the free energy density between the BCC and HEX phases (dashed lines), as well as between the BCC and σ phases (solid lines) as a function of ε where polymers are modeled as (top) continuous Gaussian and (bottom) discrete freely jointed chains. The parameters are $f = 0.25$ and $\chi N = 30$.

We next consider the phase behavior of FJCs with A-block dispersity described by the SZ distribution. The results allow for a comparison of the effects of dispersity with continuous Gaussian chains. It also serves as a reference point later when investigating the formation of complex spherical phases for other MWDs. In Figure 5.4, we show the phase diagram as a function of the average segregation strength $\chi \langle N_c \rangle$ and f. The mean and shape parameter of the SZ distribution is $\langle N_{\mathrm{A},c} \rangle = 12$ and $k = 1.5$, respectively, which corresponds to a dispersity index of $Đ(N_{\mathrm{A},c}) = 1.5$. Similar to Section 3.2, we treat the chain-length distribution using the four-point Gauss-Laguerre quadrature in numerical calculations. The number fractions of polymers with A-block

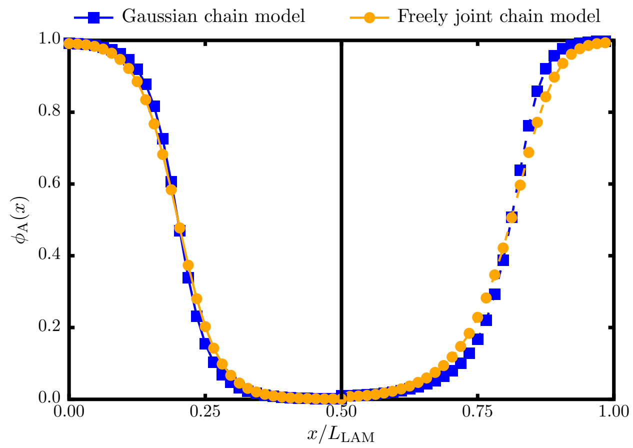

Figure 5.3: Spatially-varying volume fraction of A-monomers $\phi_{\mathrm{A}}(x)$ for the lamellar phase as a function of the normalized position x/L_{LAM} at $\chi \langle N_c \rangle = 30$ for continuous Gaussian (blue) and freely jointed chains (orange). The conformational asymmetry parameter is $\varepsilon = 1.0$ (left) and $\varepsilon = 2.0$ (right).

lengths $N_{\mathrm{A},c} = \lambda_c \langle N_{\mathrm{A},c} \rangle$ are $P_c = P_{\mathrm{SZ},4}(c)$, which are tabulated in Table 5.1 for reference. For simplicity, we also carry out the calculations in the canonical ensemble, ignoring the possibility of phase separation. The effects of using the quadrature rule and ignoring macro-phase separation were discussed earlier in Chapter 3. We again tune f by only changing the B-block length. Upon adding dispersity, FK phases other than the σ phase, namely A15, C14 and C15, become accessible. The appearance of these non-classical packings due to dispersity was observed for continuous Gaussian chains (see Figure 3.7a). In fact, the variety of complex structures is identical for the two chain models. We find that the phase behavior of the spherical phases in both monodisperse and disperse systems is fairly similar between the continuous Gaussian and discrete FJC models.

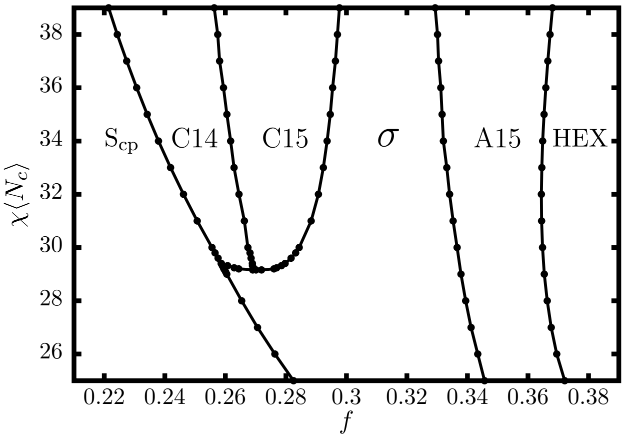

Figure 5.4: Phase diagram of disperse freely jointed chains as a function of the segregation strength $\chi\langle N_c\rangle$ and A-volume fraction f with $\varepsilon = 2$. The number fraction of different types of polymer chains is given by the $P_{\mathrm{SZ},4}(c)$.

c	0	1	2	3
$N_{\mathrm{A},c}$	56	27	11	2
P_c	5.07×10^{-3}	0.176	0.624	0.195

Table 5.1: Values of the A-block length $N_{\mathrm{A},c}$ and number fraction $P_c = \mathrm{SZ}(\lambda_c;\mu)\,W_c$ for each polymer type c for the four-point approximation of the SZ distribution $P_{\mathrm{SZ},4}(c)$. Here, the weights associated with the abscissas λ_c from the Gauss-Laguerre quadrature rule are denoted W_c.

5.1.1 Spatial distribution of polymer chains

We saw in Chapter 3 that chain segregation provide the mechanisms of the formation of complex spherical phases in continuous Gaussian chains. We can confirm that the same effects are present in discrete FJCs by examining how the polymers are spatially distributed within the self-assembled domains. For clarity, our analysis is again performed on the A15 phase. In Figure 5.5, we plot the spatial distribution of chain junctions on the $z = 0$ plane for the four different A-blocks at $f = 0.35$ and $\chi\langle N_c\rangle = 30$. Strictly speaking, discrete chains do not have a chain junction defined in the same way as continuous chains. Instead as a proxy, we take the average between the spatially-varying volume fractions of the only A- and B-monomers sharing a bond together along the backbone:

$$\phi_{j,c}\left(\boldsymbol{r}\right) = \frac{\Phi_{\mathrm{A},c}\left(\boldsymbol{r}\right) + \Phi_{\mathrm{B},c}\left(\boldsymbol{r}\right)}{2}. \tag{5.1}$$

Here, the monomer volume fractions are given by,

$$\begin{aligned} \Phi_{\mathrm{A},c}\left(\boldsymbol{r}\right) =& \frac{P_c}{\langle v_c \rangle} \frac{1}{Q_c} \left[v_{\mathrm{A}} \exp\left[\omega_{\mathrm{A}}(\boldsymbol{r})\right] q_c(\boldsymbol{r}, N_{\mathrm{A},c}) q_c^{\dagger}(\boldsymbol{r}, N_{\mathrm{B}}+1) \right], \\ \Phi_{\mathrm{B},c}\left(\boldsymbol{r}\right) =& \frac{P_c}{\langle v_c \rangle} \frac{1}{Q_c} \left[v_{\mathrm{B}} \exp\left[\omega_{\mathrm{B}}(\boldsymbol{r})\right] q_c(\boldsymbol{r}, N_{\mathrm{A},c}+1) q_c^{\dagger}(\boldsymbol{r}, N_{\mathrm{B}}) \right]. \end{aligned} \tag{5.2}$$

We notice that the distribution of junctions varies with the chain length and largely resembles what was seen earlier for disperse Gaussian chains (see Figure 3.8). The junctions of polymers with the shortest A-blocks are mainly located at the interstitial sites in the B-rich matrix, as shown in Figure 5.5d. We see from Figure 5.5c that the junction of shorter A-block chains found in the interfacial regions are more concentrated in the areas where the interface is more curved. For the longer molecules depicted in Figure 5.5a-b, the chain junctions tend to aggregate at the flatter parts of the interface. The junction distribution is also higher in the larger, more polyhedral-like than the smaller, rounder A-rich domains.

The spatial distribution of the chain junctions confirms that the same inter- and intra-domain segregations observed in disperse Gaussian chains are also present in FJCs. As mentioned before, inter-domain segregation, seen here more predominately for the longer chains, facilitate the assembly of micelles with different sizes. Segregation within individual domains favors non-spherical cores to form [47]. Before continuing, we briefly note that the regions where the junction distribution is highest are thicker than those predicted for Gaussian chains due to the combination of two reasons. One is due to the interfacial width being greater in FJCs, which was seen in Figure 5.3. The other is due to the proxy taken to be the junction distribution.

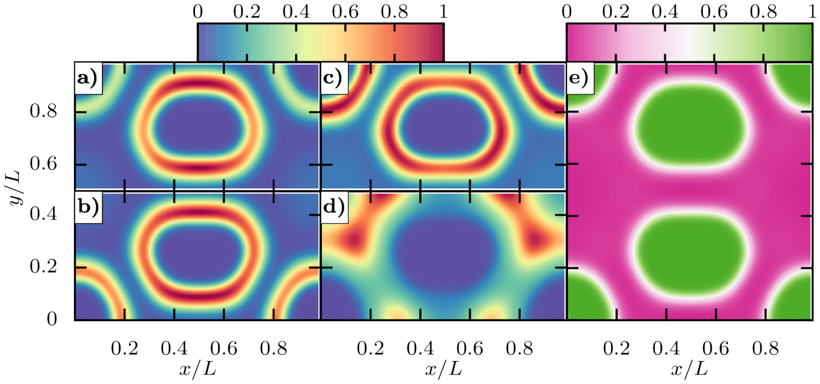

Figure 5.5: Density plots of the normalized junction distributions (Eq. 5.1) for polymers with A-block length (a) $N_{\mathrm{A},0} = 56$, (b) $N_{\mathrm{A},1} = 27$, (c) $N_{\mathrm{A},2} = 11$ and (d) $N_{\mathrm{A},3} = 2$ on the $z = 0$ plane for an equilibrium A15 phase. The spatially-dependent volume fraction of A-monomers $\phi_{\mathrm{A}}(\boldsymbol{r})$ is shown alongside in (e). The parameters are $\varepsilon = 2$, $P_c = P_{\mathrm{SZ},4}(c)$, $f = 0.35$ and $\chi \langle N_c \rangle = 30$.

5.2 The effects of dispersity index and skewness

Recent works have shown that the shape of a MWD can have a considerable impact on the equilibrium behavior of polymeric systems. The MWD shape can be described by its moments. The first moment μ_1 is the average molecular weight, while the second moment μ_2 quantifies the width of the MWD. The third moment describes the asymmetry of the peak in MWDs. Commonly, only the dispersity index, $Đ = \mu_2/\mu_1^2$, is used. However, the importance of $\widetilde{\mu}_3$ is gradually being recognized. As discussed in the previous chapter, experiments by Gentekos *et al.* demonstrated that the domain spacing [43, 41] and morphology [4, 41] of the equilibrium phase can depend on the skewness. It is noted that skewness offers information on the tail of the distribution and how the probability behaves around the mean [44]. For a uni-modal distribution, a positive value of skewness indicates that the tail is located to the right, and the mass of the distribution is concentrated to the left of mean. The opposite is true for a negative skewness.

We will examine below how the MWD shape affects the formation of spherical packing phases. In particular, we focus on the interplay between the dispersity index and skewness. Starting with the (approximate) SZ distribution, we will selectively adjust each of the populations of polymers to explore a variety of MWD shapes with different skewness and dispersity indices. To ensure that the number fractions sum to unity, a replacement distribution is considered,

$$\widetilde{P}_{\mathrm{SZ},4}(c;R,P_R)=\begin{cases} P_R & c=R \\ \frac{1-P_R}{1-P_{\mathrm{SZ},4}(R)}P_{\mathrm{SZ},4}(c) & c\neq R \end{cases}. \tag{5.3}$$

Here, the index R denotes the type of polymers with its number fraction replaced by the new value P_R. Using Eq. (5.3), one can vary the probability of one specific component, while preserving the relative amounts of the others, i.e.,

$$\frac{\widetilde{P}_{\mathrm{SZ},4}(c;R,P_R)}{\widetilde{P}_{\mathrm{SZ},4}(c';R,P_R)}=\frac{P_{\mathrm{SZ},4}(c)}{P_{\mathrm{SZ},4}(c')}, \tag{5.4}$$

for c, $c' \neq R$.

We start by examining the phase behavior when the population of polymers at the tails of the distribution is removed. Doing so leads to significant changes to the MWD shape. In particular, the dispersity index changes from its original value of $Đ(N_{\mathrm{A},c})=1.50$ to 1.41 and 1.25 upon excluding the longest and shortest components,

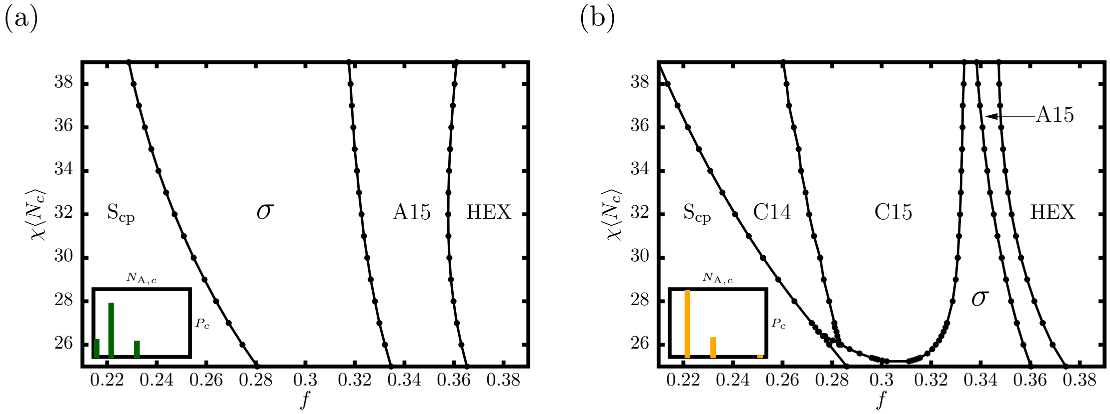

Figure 5.6: Phase diagrams as a function of the segregation strength $\chi\langle N_c\rangle$ and A-volume fraction f with $\varepsilon = 2$. The number fractions of chains with differing A-block lengths are given by (a) $\widetilde{P}_{\mathrm{SZ},4}(c; 0, 0)$ and (b) $\widetilde{P}_{\mathrm{SZ},4}(c; 3, 0)$. Insets show the corresponding distribution of A-block lengths.

respectively. The skewness similarly is altered from $\widetilde{\mu}_3 = 1.33$ to 0.83 and 1.98, respectively.

We first consider the case where the longest chains ($R = 0$) are absent. Figure 5.6a gives the phase diagram as a function of $\chi\langle N_c\rangle$ and f where the A-block lengths follow the distribution $\widetilde{P}_{\mathrm{SZ},4}(c; 0, 0)$. We again tune the length of the common B-block to adjust f. A noticeable change occurs in the phase behavior when the longest molecules are excluded. For the same range of parameters, both the C14 and C15 phases are replaced by the σ phase. This difference is caused remarkably by only removing a population of chains that is less than 1% of the total number of chains in the system. We see from Figure 5.7 that the re-scaled probabilities of the three other components are almost visually indistinguishable to the original values $P_{\mathrm{SZ},4}(c)$. The stark contrast in the phase behavior from excluding such a small population of chains reflects the special role played by polymers with the longest A-blocks.

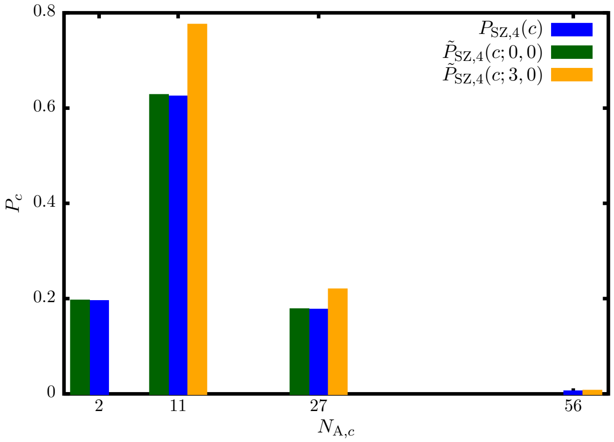

Figure 5.7: Probability weights P_c as a function of A-block lengths, $N_{\mathrm{A},c}$ for the distributions, $P_{\mathrm{SZ},4}(c)$ (blue), $\widetilde{P}_{\mathrm{SZ},4}(c;0,0)$ (green), $\widetilde{P}_{\mathrm{SZ},4}(c;3,0)$ (yellow).

Next, we examine the effect of removing the shortest molecules from the distribution. Different from the longest component, the shortest chains represent nearly 20% of the total number of chains, and there is a visible difference between the parent and re-scaled probabilities given by $\widetilde{P}_{\mathrm{SZ},4}(c;3,0)$. We plot in Figure 5.6b the phase diagram as a function of $\chi \langle N_c \rangle$ and f where the A-block lengths follow the distribution $\widetilde{P}_{\mathrm{SZ},4}(c;3,0)$. As expected, the change in the phase behavior is opposite to what was seen when excluding the longest chains. The C14 and C15 phases occupy a larger portion of the phase diagram, appearing at lower segregation strengths and over a wider span of f. The expansion comes at the expense of the σ and A15 phases. We find however that the sequence of spherical packings A15 $\rightarrow \sigma \rightarrow$ C15 $\rightarrow$ C14 $\rightarrow$ $\mathrm{S_{cp}}$ as f decreases remains unchanged from the parent distribution seen in Figure 5.4.

The difference in the phase behavior between Figures 5.6a and 5.6b implies that larger values of skewness favors the assembly of the C14 and C15 structures. Large positive skewness implies a (minor) population of very long polymers at the tail of the distribution, which should be most beneficial for the self-assembly of the C14 and C15 phases. Among the considered FK phases, both feature the largest volume differences between the symmetrically non-equivalent Voronoi cells and by extension, the enclosed A-rich domains (see Figure 5.8). The role of the longer chains is similar to that of homopolymers blended with diblock copolymers, where the C14 and C15 phases have also been observed experimentally [52] and theoretically [48, 49]. The homopolymers residing in the interior of the A-rich cores relieve the need of stretching diblock copolymers anchored to the A/B interface to fill the space most distant from the interfacial region. Polymers with longer A-blocks can efficiently pervade the same space. Inter-domain segregation of the homopolymers or longer diblock copolymers will subsequently facilitate the formation of different sized micelles.

Before continuing, we note that the mean chain length $\langle N_c \rangle$ will vary slightly when excluding either the shortest or longest polymers from the system. While the phase behavior exhibited by FJCs does depend on the total chain length, the differences between Figures 5.6a and 5.6b cannot simply be attributed to the shift of $\langle N_c \rangle$. For the shortest common B-block length we considered, the change is less than 10% (ranging from $\langle N_c \rangle = 27$ to 29) and decreases with increasing N_{B}. As a rough comparison, the topology of the phase diagram is identical between $N = 40$ and 80, with the shift in the phase boundaries being approximately 1% in f for monodisperse melts [71].

To further probe the interplay between skewness and dispersity and discern their importance on the variety of accessible spherical phases, we next adjust each of the probabilities P_c, fixing instead the segregation strength to $\chi \langle N_c \rangle = 30$. In Figure 5.9a, we show the phase diagram as a function of the number fraction of the longest polymers P_0 and A-volume fraction f. The A-block lengths obey the distribution $\widetilde{P}_{\mathrm{SZ},4}(c; 0, P_0)$. Consistent with earlier results, only the σ and A15 morphology

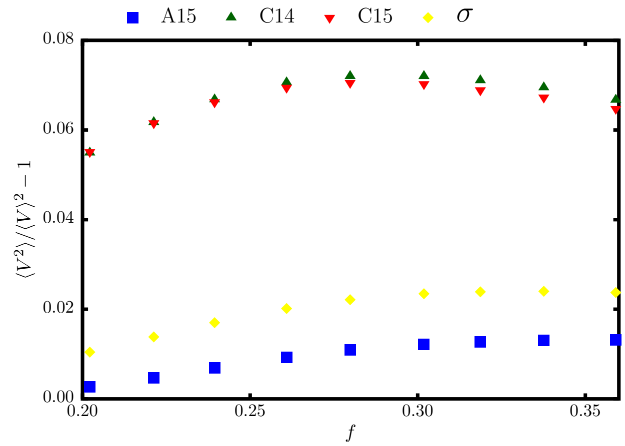

Figure 5.8: Mean micelle volume deviations for different complex spherical phases as a function of the A-volume fraction f. Here, $\langle V^n\rangle = \left(\sum V^n_{\mathrm{mi}} M_{\mathrm{mi}}\right) / \left(\sum M_{\mathrm{mi}}\right)$, and V^n_{mi} denotes the volume of the micelles with a multiplicity of M_{mi}. The parameters are $P_c = P_{\mathrm{SZ},4}(c)$, $\varepsilon = 2$ and $\chi \langle N_c\rangle = 30$. The different types of micelles for C14 and C15 phases feature the greatest disparity in volume.

are present when $P_0 \lesssim 0.01$. Upon increasing P_0, both the C14 and C15 phases emerge, while the σ-phase region gradually recedes and disappears. Interestingly, the behavior featured by the spherical phases is not monotonic in P_0. Continuing to add the longest molecules for $P_0 \gtrsim 0.07$ re-introduces the σ phase into the phase diagram and narrows the window of stability for C15 phase. We also find that the $\mathrm{S_{cp}}$ phase can appear over a region where the A-volume fraction exceeds 30% at larger values of P_0. Its occurrence is remarkable considering the close-packed spheres are only found within a narrow window centered about $f \in [0.1, 0.2]$ in monodisperse melts for $\chi N \approx 30$ [71]. We will discuss its origins in the upcoming sections.

We plot in Figure 5.9b the phase diagram analogous to Figure 5.9a except the probability of the second longest polymers P_1 is varied instead. The A-block length distribution is $\widetilde{P}_{\mathrm{SZ},4}(c; 1, P_1)$. Unlike in the absence of the longest component, the C14 and C15 alongside the σ phase can occur when $P_1 = 0$. We find that there are no

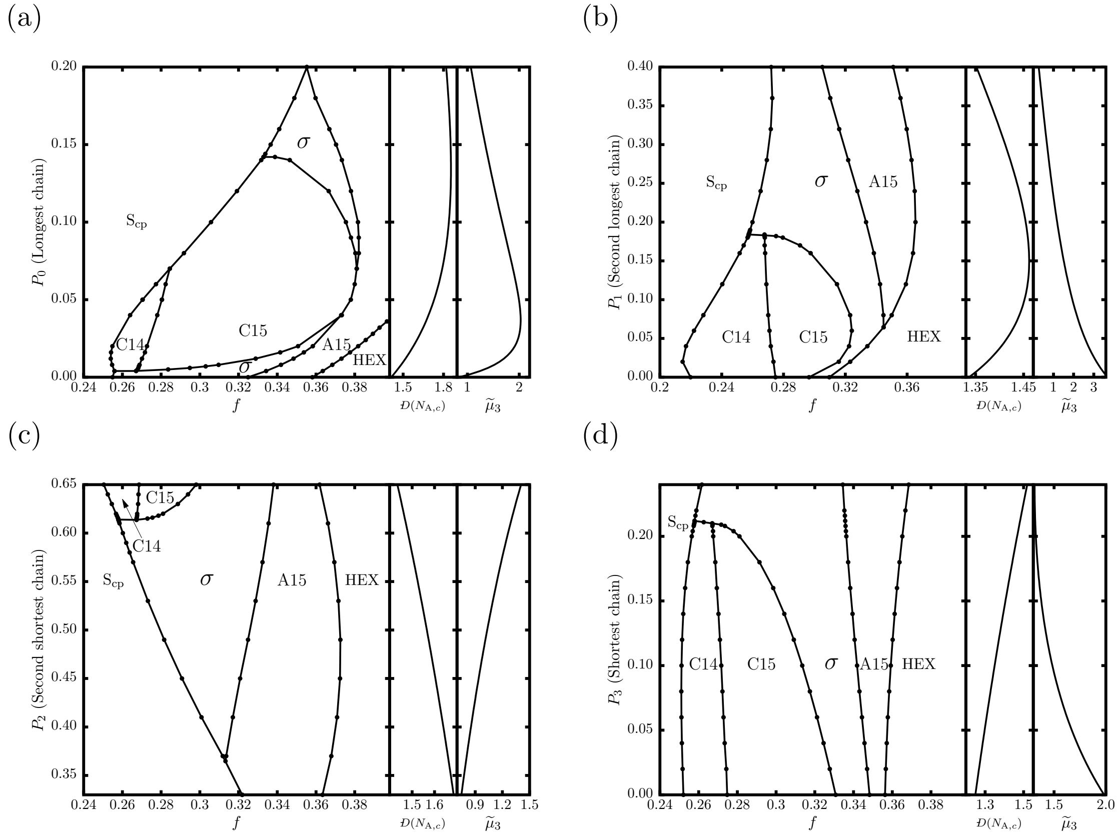

Figure 5.9: Phase diagrams as a function of the A-volume fraction f and probability P_c with $\varepsilon = 2$ and $\chi \langle N_c \rangle = 30$. The number fractions of polymer chains with different A-block lengths P_c are given by (a) $\widetilde{P}_{\mathrm{SZ},4}(c; 0, P_0)$, (b) $\widetilde{P}_{\mathrm{SZ},4}(c; 1, P_1)$, (c) $\widetilde{P}_{\mathrm{SZ},4}(c; 2, P_2)$ and (d) $\widetilde{P}_{\mathrm{SZ},4}(c; 3, P_3)$. To the right of each phase diagram, the dispersity index and skewness are shown as function of P_c.

A-volume fractions where the C14 and C15 phases can be stabilized once P_1 exceeds roughly 0.18. Instead, the only non-classical packings predicted are the A15 and σ.

Figure 5.9c depicts the phase behavior as a function of f and the number fraction of polymers with the second shortest A-blocks P_2. The distribution of A-block lengths is described by $\widetilde{P}_{\mathrm{SZ},4}(c; 2, P_2)$. Near the top of the phase diagram where P_2 nearly coincides with its original value ($P_{\mathrm{SZ},4}(2) \approx 0.65$), the C14 and C15 phases are featured over a narrow region. Both cease to appear as equilibrium phases once $P_2 \lesssim 0.61$.

When further decreasing P_2 beyond ~ 0.35, the σ phase also becomes inaccessible. It is interesting to note that in this vicinity where the only predicted complex phase is the A15, the distribution $\widetilde{P}_{\mathrm{SZ},4}(c;2,P_2)$ is fairly flat in that $P_1 \approx P_2 \approx P_3 \approx 0.3$. Lastly, we show the phase diagram as a function of f and number fraction of the shortest polymers P_3 in Figure 5.9d. The A-block lengths obey $\widetilde{P}_{\mathrm{SZ},4}(c;3,P_3)$. The equilibrium behavior shares some similarities with what is seen in Figure 5.9b. We see that both the C14 and C15 phases can occur when P_3 is zero. The window of stability for the two phases shrinks as the population of the shortest molecules grows, eventually vanishing at $P_3 \approx 0.21$.

5.2.1 Relationship with dispersity index

Alongside each phase diagram shown in Figure 5.9, we plot the A-block dispersity index $Đ(N_{\mathrm{A},c})$ and skewness $\widetilde{\mu}_3$ as a function of P_c. As seen in Figure 5.9a, selectively changing the number fraction of the longest chains results in a dispersity index and skewness that are non-monotonic in P_0. Both quantities initially increase and subsequently decrease as P_0 runs from 0 to 0.2. The same applies for $Đ(N_{\mathrm{A},c})$ when varying the population of polymers with the second longest A-blocks in Figure 5.9b. However, the skewness monotonically decreases with P_1. For Figures 5.9c and 5.9d, both $Đ(N_{\mathrm{A},c})$ and $\widetilde{\mu}_3$ are monotonic functions of the respective number fractions. In particular, the dispersity index increases with P_2 whereas the skewness decreases. The opposite is true for P_3.

From Figure 5.9a, we see that the C15 phase, and the C14 to a lesser extent, is present for nearly the whole range of A-block dispersity index. Despite the change in $Đ(N_{\mathrm{A},c})$ being less than 2% over the interval $0.1 \leq P_0 \leq 0.2$, there is notable variation in the phase behavior. The C15 phase becomes absent once $P_0 \gtrsim 0.14$. A similar result is found in Figure 5.9b. We find that despite the range of $Đ(N_{\mathrm{A},c})$ for $P_1 \leq 0.19$ and $P_1 \geq 0.19$ is roughly the same, the predicted complex spherical phases are very different. For $0 \leq P_1 \leq 0.19$, the C14, C15, A15 and σ phases are present, whereas the σ and A15 are the only non-classical phases found when $P_1 \gtrsim 0.19$. We can conclude from Figures 5.9a and 5.9b that the dispersity index $Đ(N_{\mathrm{A},c})$ does not correlate well with the emergence of the complex phases.

There is a stronger correlation between the A-block dispersity index and equilibrium behavior when the number fraction of the shorter polymers is selectively adjusted. We see in Figure 5.9c that the C14 and C15 phases are present for the lowest values of $Đ(N_{\mathrm{A},c})$ and disappear when the dispersity index increases by decreasing P_2. Similarly in Figure 5.9d, both structures can appear for nearly the whole range of P_3 barring $P_3 \geq 0.21$ where $Đ(N_{\mathrm{A},c})$ is lowest. When considering only the results of Figures 5.9c and 5.9d, it may be tempting to think that lower degrees of dispersity encourage the assembly of the C14 and C15 phases.

5.2.2 Relationship with skewness

Next, the relation between skewness and the formation of complex spherical phases is explored. We again start with Figure 5.9a. Over the interval $0.01 \lesssim P_0 \lesssim 0.14$ where the C14 and C15 phases form, $\widetilde{\mu}_3$ has larger values. Only the A15 and σ phases are predicted for both $P_0 \gtrsim 0.01$ and $P_0 \lesssim 0.14$ where the skewness has smaller values (similar to both intervals). The situation is more straightforward in Figures 5.9b-5.9d where $\widetilde{\mu}_3$ is a monotonic function of the respective number fractions. In all three cases, we observe that the C14 and C15 phases are found whenever $\widetilde{\mu}_3$

is greatest. In Figures 5.9b and 5.9d where $\widetilde{\mu}_3$ is a decreasing function, the two structures are accessible at lower values of P_1 and P_3. On the other hand, the skewness monotonically increases with P_2 for Figure 5.9c. The regions occupied by the C14 and C15 morphology are located at higher number fractions where again the distribution is most positively-skewed.

The relation between the skewness and relative stability of the non-classical phases can be made more transparent by re-casting the y-axis from the number fractions to the skewness instead. Doing so leads to the phase diagrams shown in Figure 5.10. As noted above, the skewness of the A-block length distribution $\widetilde{P}_{\mathrm{SZ},4}(c;0,P_0)$ is not monotonic in P_0. The skewness increases and decreases when moving along the portions of the y-axis below and above the dotted line in Figure 5.10a, respectively. In all four cases, we observe that the C14 and C15 morphology are found at larger values of $\widetilde{\mu}_3$. The region occupied by the two phases is in the middle for Figure 5.10a, whereas its location is at the top of the phase diagram for Figures 5.10b-5.10d. When the phase behavior is shown as a function of skewness, we also notice that the A15-region tends to widen over f when $\widetilde{\mu}_3$ decreases. We therefore find that strongly positively-skewed distributions favors the formation of the C14 and C15 phases, while decreasing the skewness gives way to the A15 and σ phases. This is consistent with the work of Liu *et al.* on binary blends [47]. A larger asymmetry in the chain lengths between the two components (with the longer polymers being the minority) would result in a wider range of blend compositions where the C14 and C15 phases could appear. On the other hand, only the σ phase is expected for lower ratios of chain lengths.

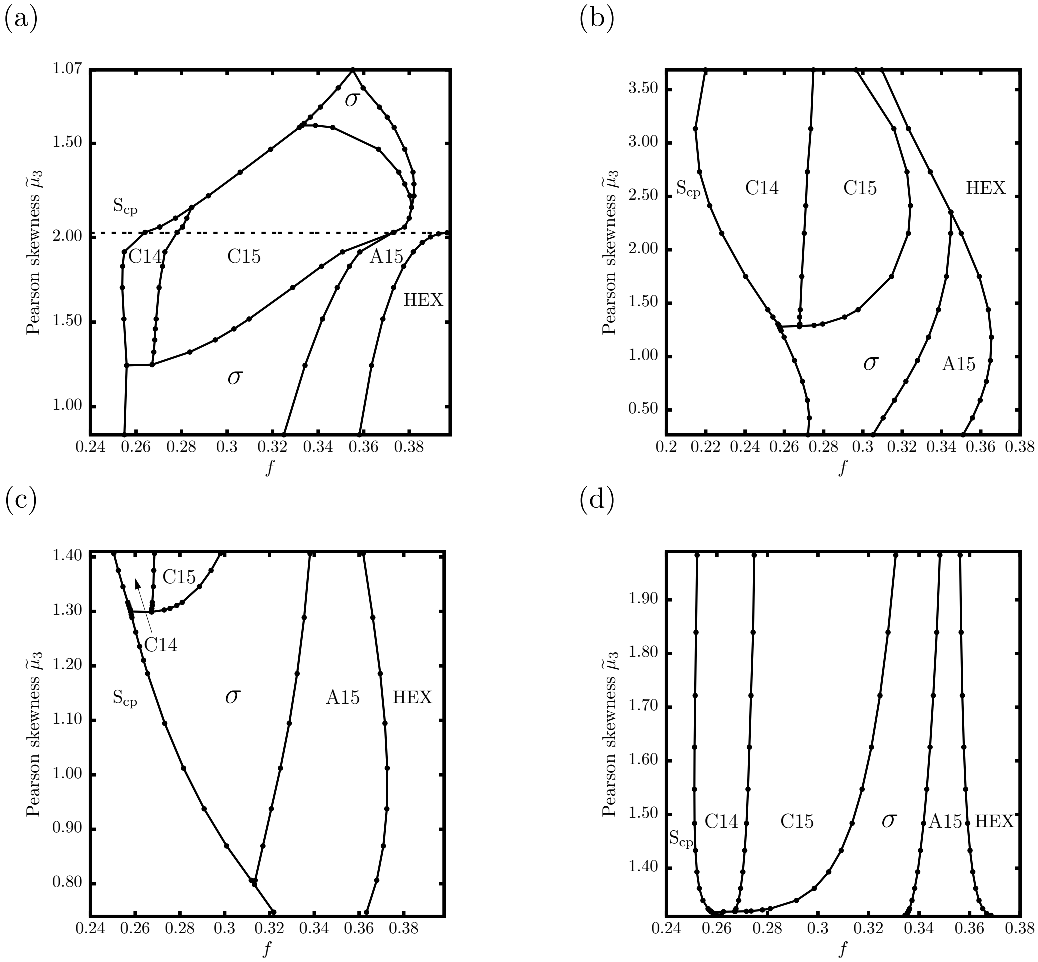

Figure 5.10: Phase diagrams as a function of the A-volume fraction f and skewness $\widetilde{\mu}_3$ with $\varepsilon = 2$ and $\chi \langle N_c \rangle = 30$. The number fraction of polymer chains with A-block length $N_{\mathrm{A},c}$ is given by (a) $\widetilde{P}_{\mathrm{SZ},4}(c; 0, P_0)$, (b) $\widetilde{P}_{\mathrm{SZ},4}(c; 1, P_1)$, (c) $\widetilde{P}_{\mathrm{SZ},4}(c; 2, P_2)$ and (d) $\widetilde{P}_{\mathrm{SZ},4}(c; 3, P_3)$.

5.3 Variations in the A-block lengths

In this subsection, we investigate the impact of adjusting the A-block lengths $N_{\mathrm{A},c}$ on the phase behavior. The results yield more insights on the roles played by polymers with different chain lengths in the self-assembly of spherical phases. In Figure 5.11a, we show the phase diagram as a function of the number fraction P_0 and

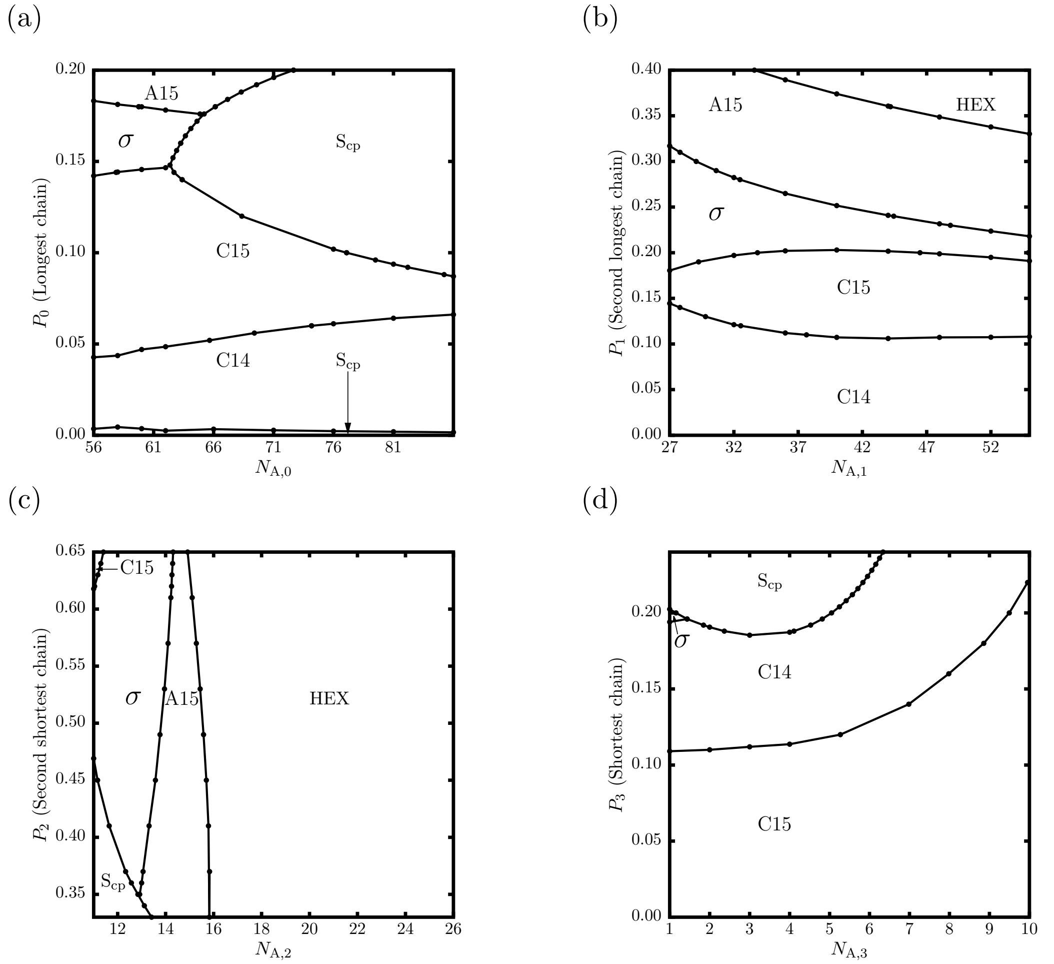

Figure 5.11: Phase diagrams as a function of the A-block length $N_{\mathrm{A},c}$ and A-monomer volume fraction f with $\varepsilon = 2$ and $\chi \langle N_c \rangle = 30$. The number fraction of polymer chains with differing A-block lengths P_c is given by (a) $\widetilde{P}_{\mathrm{SZ},4}(c; 0, P_0)$, (b) $\widetilde{P}_{\mathrm{SZ},4}(c; 1, P_1)$, (c) $\widetilde{P}_{\mathrm{SZ},4}(c; 2, P_2)$ and (d) $\widetilde{P}_{\mathrm{SZ},4}(c; 3, P_3)$.

A-block length $N_{\mathrm{A},0}$ of the longest component. The distribution of A-block lengths is $\widetilde{P}_{\mathrm{SZ},4}(c; 0, P_0)$. Note that the common B-block length is fixed to $N_{\mathrm{B}} = 36$ for the calculation. Additionally, the ranges of A-block lengths are restricted such that the order, $N_{\mathrm{A},0} > N_{\mathrm{A},1} > N_{\mathrm{A},2} > N_{\mathrm{A},3}$, is preserved. For $N_{\mathrm{A},0} \lesssim 62$, we find the sequence of complex phases C14 → C15 → σ → A15 as P_0 increases is identical to what is seen in Figures 5.4 and 5.6b when increasing f. At smaller values of P_0, the equilibrium behavior is fairly insensitive to the exact makeup of the longest molecules, presumably due to its low concentration.

Remarkably, a $\mathrm{S_{cp}}$ phase is predicted to be accessible for $P_0 \gtrsim 0.08$ where the A-volume fraction can exceed 40%. Its appearance at nearly symmetric values of f could be understood by examining the spatial arrangement of polymers. The junction distributions of polymers with different A-block lengths are illustrated in Figures 5.12a-d at $N_{\mathrm{A},0} = 86$ and $P_0 = 0.20$. We show alongside the spatially-dependent volume fractions $\phi_{\mathrm{A},c}(\boldsymbol{r})$ in Figures 5.12e-h. The behavior of the chain junctions is very different from what is seen in Figure 5.5. When P_0 is large, the cores for both types of micelles are almost made up entirely of the A-blocks from the longest component. The second longest polymers are only located at the edges of the A-domains. We observe that the degree of inter-domain segregation is much weaker compared to Figures 5.5a-b. As seen in Figure 5.12d, the shortest molecules are dispersed fairly uniform throughout the B-matrix as opposed to being concentrated at the interstitial regions. Even the polymers with the second shortest A-blocks shown in Figure 5.12c are found in the interstices at concentrations nearly equal with the interfacial regions. We will see below that when there are many dislodged polymers within the B-matrix, the $\mathrm{S_{cp}}$ lattice will be favored.

In Figure 5.11b, we depict the phase behavior as a function of $N_{\mathrm{A},1}$ and probability of second longest molecules P_1. The A-block lengths follow the distribution $\widetilde{P}_{\mathrm{SZ},4}(c; 1, P_1)$ while the common B-block length is $N_\mathrm{B} = 32$. We see that the four FK phases can be realized at any A-block length $N_{\mathrm{A},1}$ by selecting an appropriate value for P_1. In fact, the same phase sequence C14 → C15 → σ → A15 as P_1 increases is

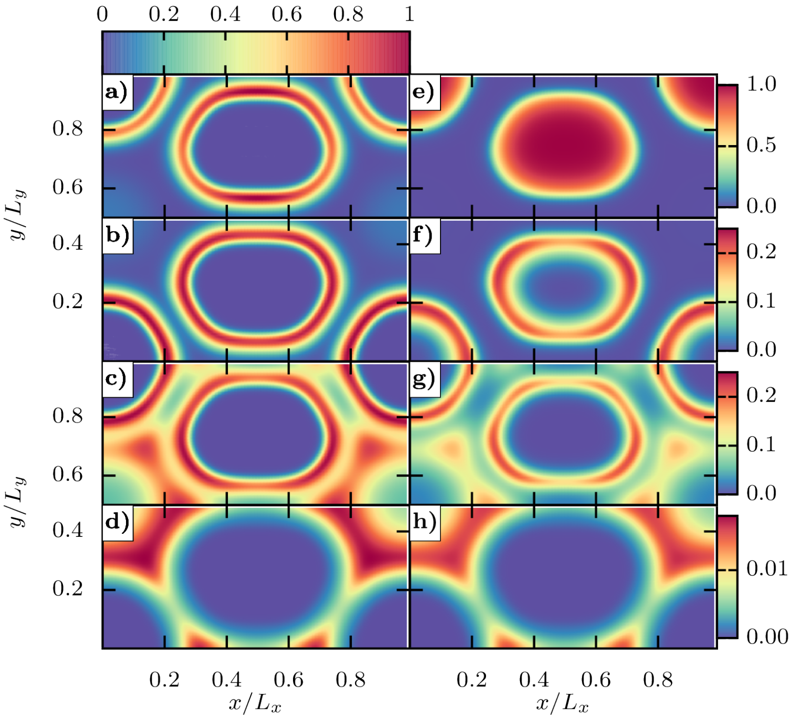

Figure 5.12: Density plots of the (a)-(d) normalized junction distributions (Eq. 5.1) and (e)-(h) A-volume fraction $\phi_{\mathrm{A},c}(\boldsymbol{r})$ for polymer chains with A-block length (a)/(e) $N_{\mathrm{A},0} = 86$, (b)/(f) $N_{\mathrm{A},1} = 27$, (c)/(g) $N_{\mathrm{A},2} = 11$ and (d)/(h) $N_{\mathrm{A},3} = 2$ on the $z = 0$ plane for an A15 phase. The parameters are $\varepsilon = 2$, $P_0 = 0.2$ and $P_c = \widetilde{P}_{\mathrm{SZ},4}(c; 0, P_0)$.

encountered regardless of $N_{\mathrm{A},1}$. We find that the preferred spherical packing shows a stronger dependency on P_1 than $N_{\mathrm{A},1}$. Even at the largest probabilities, the phase boundaries remain fairly horizontal. Consequently, the phase behavior is nearly the same at the two extreme ends, $N_{\mathrm{A},1} = 27$ and 56. At the latter, we may view the second longest chains as effectively replaced by the longest polymers, being almost identical in composition ($N_{\mathrm{A},0} - N_{\mathrm{A},1} = 57 - 56 = 1$). This suggests that the roles served by the two longest components are similar, provided the difference between $N_{\mathrm{A},0}$ and $N_{\mathrm{A},1}$ is not as extreme as what was examined in Figure 5.12. The overlap in roles was also observed earlier when analyzing the spatial arrangement of polymers within the spherical domains (see Figure 5.5).

Figure 5.11c depicts the phase behavior as a function of $N_{\mathrm{A},2}$ and the number fraction of the second shortest polymers P_2. The distribution of A-block lengths is given by $\widetilde{P}_{\mathrm{SZ},4}(c; 2, P_2)$, and the shared B-block is $N_{\mathrm{B}} = 32$. At a glance, we notice that a large area of the phase diagram is occupied by hexagonally-packed cylinders. In fact, the HEX phase is always preferred regardless of any changes to the distribution once $N_{\mathrm{A},2} \gtrsim 16$. For $N_{\mathrm{A},2} \lesssim 16$, we see a familiar phase sequence of HEX $\rightarrow$ A15 $\rightarrow \sigma$ for nearly the whole range of P_2. Further decreasing $N_{\mathrm{A},2}$ can induce either a $\sigma \rightarrow$ C15 and $\sigma \rightarrow \mathrm{S}_{\mathrm{cp}}$ transition at the higher and lower values of P_2, respectively. We find that the A-block length $N_{\mathrm{A},2}$ plays a greater role in determining the phase behavior here, dictating whether spherical or cylindrical micelles will be favored. This is in contrast with Figures 5.11a and 5.11b where the phase behavior was more strongly dependent on the probabilities of the longer chains. The sensitivity of the phase behavior to $N_{\mathrm{A},2}$ can be attributed to the fact that P_2 represents the largest population in the distribution. It is therefore not surprising that changes to the block composition of the polymers belonging to P_2 would affect the equilibrium behavior the most (out of the four components).

Lastly, we plot the phase behavior as a function of the relative population P_3 and A-block length $N_{\mathrm{A},3}$ of the shortest polymers in Figure 5.11d. The A-block lengths obey the distribution $\widetilde{P}_{\mathrm{SZ},4}(c; 3, P_3)$, and the common B-block length is $N_{\mathrm{B}} = 36$. Changing either P_3 or $N_{\mathrm{A},3}$ will influence the availability of short A-block chains that can be dislodged from the interface and placed into the B-rich matrix for different reasons. Longer A-blocks result in a larger enthalpic penalty for situating the short polymers in the matrix due to the greater number of unfavourable A/B contacts per molecule, reducing their tendency to become displaced from the interface. On the other hand, increasing P_3 directly makes more of the polymers with short A-blocks available to be placed in the B-domain. As the fraction of shortest chains becomes larger, we find the phase sequence proceeds as C15 → C14 → $\mathrm{S_{cp}}$. The same was seen in Figures 5.4 and 5.6b as f decreases by increasing the common B-block length. Both increasing P_3 or N_B enrich the fraction of free polymer chains residing in the B-rich matrix. By the same effect, it is also possible to induce the C15 → C14 and C14 → $\mathrm{S_{cp}}$ transitions by decreasing the A-block length $N_{\mathrm{A},3}$ at the larger examined values of P_3.

From Figures 5.4 and 5.11d, we can deduce that the availability of short polymers that can be dislodged and placed into the B-matrix should favor, in decreasing order, $\mathrm{S_{cp}} > \mathrm{C14} > \mathrm{C15} > \sigma > \mathrm{A15}$. When the amount of dislodged chains is low, the interstitial spaces that causes packing frustration have to be filled by stretching chains originating from the interface. One measure that characterizes such manner of stretching is the mean stretching moment $\mathcal{I}(X)$ [17, 81]. A calculation by Reddy *et al.* using the diblock foam model [81] ranks from least to most optimal stretching, $\mathcal{I}\,(\mathrm{C15}) \gtrsim \mathcal{I}\,(\mathrm{C14}) > \mathcal{I}\,(\sigma) > \mathcal{I}\,(\mathrm{A15}) > \mathcal{I}\,(\mathrm{BCC})$. The ranking nicely coincides with the progression of equilibrium spherical phases as the likelihood of finding short A-block polymers in the B-matrix is reduced. Based solely on considerations of optimal stretching, it may be possible that the A15 phase is eventually followed by the BCC at higher values of f where the fraction of dislodged chains is even lower, providing that spherical micelles remains preferred over cylinders. It is therefore interesting to mention that in a study by Qiang *et al.* [82] on dendron-like AB-type block copolymers, the phase sequence σ → A15 → BCC is predicted as f increases. Despite the σ

and A15 phases spanning an extremely wide window over f (~ 0.15 to 0.7), neither the C14 and C15 morphology are present. Their absence could be related to lack of short chains that act as fillers in the B-rich matrix and long molecules that encourage the assembly of micelles with large volume asymmetries. The former would also explain why the width of the $\mathrm{S_{cp}}$-region was found to be roughly the same as what is predicted in monodisperse diblock copolymers.

In the current chapter, we examined how the formation of spherical phases is influenced by the shape of a MWD in diblock copolymers. In particular, we focused on the relationship between the dispersity index and skewness based on the discrete FJC model, which was selected for the computational advantages offered over continuous Gaussian chains. We began by looking at the differences in the phase behavior between the two chain models for monodisperse and disperse systems. For monodisperse FJCs, a lower degree of conformational asymmetry was necessary to trigger the formation of the FK σ phase. We found that the appearance of the complex phases due to dispersity can be attributed to the chain segregation effects. The relative stability of the spherical phases was subsequently examined for a variety of MWD shapes. We found that the predicted spherical packings can vary between distributions with different skewness and equal dispersity indices. In particular, more positively-skewed distributions would favor the C14 and C15 phases, while less positive values of skewness would lead to the A15 and σ phases. Similar to Chapter 4, the presented results highlight the importance of the MWD shape on the phase behavior of disperse block copolymers.

Chapter 6

Conclusion

The aim of the thesis was to examine how dispersity influences the phase behavior of diblock copolymers. In particular, we focused on the shape of the molecular weight distribution characterized by the dispersity index and skewness. The role of dispersity in the formation of complex Frank-Kasper phases was first examined in the conformationally asymmetric diblock copolymers. We found that A-block dispersity described either by the SZ or Poisson distributions would lower the critical degree of conformational asymmetry required for the formation of the σ phase. Our results on the dispersity effects reconcile the theoretical predictions and the experimental observations of Schulz *et al.* [2]. By examining the spatial distribution of polymers within the self-assembled structures, we detected the presence of inter- and intra-domain segregation of the polymers. Similar segregation effects were previously identified by Liu *et al.* [47] as the mechanisms for the appearance of non-classical spherical phases in binary blends of diblock copolymers.

We next presented a general procedure of treating molecular weight distributions specified by a set of molecular weights and mass fractions commonly found in samples of synthetic polymers. The method was subsequently applied to the MWDs of three samples used in the experiments by the Fors group [43] to examine how the distribution shape affects the self-assembly of disperse diblock copolymers. Apart from the domain spacing, we found that the morphology of the equilibrium phase itself could vary between the samples with different skewness and similar dispersity indices. The predicted phase behaviors for the positively- and negatively-skewed samples agree qualitatively with experimental observations. Given that fine-control over the distribution shape for synthetic polymers is possible presently [41, 42, 46], we expect that our proposed procedure could be valuable for future studies.

We lastly investigated how the shape of a MWD characterized by the dispersity index and skewness influences the relative stability of complex FK phases. The skewness was identified to be a key parameter regulating the formation of spherical packings. At equal dispersity indices, we found that the array of predicted spherical phases may differ drastically depending on the skewness. For moderately positively-skewed distributions of A-block lengths, the formation of the A15 morphology was enabled, while access to the C14 and C15 was possible at the largest values of skewness explored. Overall, the results underline the importance of looking beyond the width of the distribution, and the need of other statistical measures such as the skewness to complement the dispersity index when studying the phase behavior of disperse block copolymers.

Cooke and Shi [26] examined the phase behavior of disperse diblock copolymers by carrying out a perturbative expansion about the mean chain length to second order, which corresponds to the dispersity index. In light of the current work, alongside other recent studies [43, 4, 41, 45], highlighting the impact of skewness, a natural extension would be to conduct a similar calculation to the third-order term. The third-order term is related to the skewness, and would therefore allow its general effects to be more fully explored. Experiments indicate that the FK phases [83, 51, 52] often appear along with dodecagonal quasicrystalline structures, featuring twelve-fold rotational symmetry along one plane and periodicity in the direction normal to that plane. While in principle quasicrystalline phases can be incorporated into the SCFT framework [84, 85], the numerical calculations are by no means trivial. It would be of interest to examine how the relative stability of the quasicrystalline phases changes when introducing dispersity. We have shown that larger positive skewness generally enhanced the stability of the complex FK phases, leading to a greater variety that could be accessed. It remains to be seen if the propensity to form dodecagonal quasicrystalline structures would also be increased by varying the shape of the MWD. Lastly, our study of dispersity effects was mainly restricted to the sphere-forming regime of diblock copolymers. It would be interesting to study the roles played by the dispersity index and skewness in the context of novel packings of cylinders [86], as well as in the formation of exotic bicontinuous phases [87, 88, 89, 90, 91, 92].

Appendix A

Initial ansatz of numerical SCFT

In this appendix, we present analytic expressions used as an initial ansatz of $\phi_{\mathrm{A}}(\boldsymbol{r})$ for a number of ordered phases. The volume fraction of B-monomers $\phi_{\mathrm{B}}(\boldsymbol{r})$ should be initialized using the incompressibility condition $\phi_{\mathrm{A}}(\boldsymbol{r}) + \phi_{\mathrm{B}}(\boldsymbol{r}) = 1$. From the volume fractions, one can obtain the the initial ansatz of the auxiliary fields using Eq. (2.21) with $\xi(\boldsymbol{r})$ set to 0.

Starting with the homogeneous disordered phase, its initial ansatz is trivially given by a constant,

$$\phi_{\mathrm{A}}(\boldsymbol{r}) = \Phi_{\mathrm{A}}, \tag{A.1}$$

where Φ_{A} is the expected average A-volume fraction.

For the lamellar phase with layers perpendicular to the z-direction, we have,

$$\phi_{\mathrm{A}}(\boldsymbol{r}) = \Phi_{\mathrm{A}} + (1 - \Phi_{\mathrm{A}})\cos(qz), \tag{A.2}$$

where $q = 2\pi/L$ and L specifies the period.

The initial ansatz for the hexagonally-packed cylindrical phase with its axis parallel to the x-direction in a non-primitive tetragonal unit cell is,

$$\phi_{\mathrm{A}}(\boldsymbol{r}) = \cos\left(q\frac{2y}{\sqrt{3}}\right) + \cos\left[q\left(z+\frac{y}{\sqrt{3}}\right)\right] + \cos\left[q\left(z-\frac{y}{\sqrt{3}}\right)\right], \tag{A.3}$$

where we assume that $L_y = \sqrt{3}L_z = \sqrt{3}L$.

For the body-centered cubic spherical phase belonging to space group ($Im\bar{3}m$), we initialize the A-volume fraction in a cubic unit cell by,

$$\phi_{\mathrm{A}}(\boldsymbol{r}) = \frac{1}{2}\left(1+\sum_{i=0}^{2}\cos\left[q\left(x_i - x_{\overline{i+1}}\right)\right]\right), \tag{A.4}$$

where $x = x_0$, $y = x_1$, $z = x_2$ and the line above the subscripts denotes the modulo operation with modulus 3, $\bar{i} = i\,(\mathrm{mod}\,3)$.

The initial ansatz for $\phi_{\mathrm{A}}(\boldsymbol{r})$ of the face-centered cubic spherical phase in the conventional cubic unit cell is given by,

$$\phi_{\mathrm{A}}(\boldsymbol{r}) = \frac{1}{2} + \frac{1}{8}\left(\cos\left[q\left(x_0+x_1+x_2\right)\right] + \sum_{i=0}^{2}\cos\left[q\left(x_i + x_{\overline{i+1}} + x_{\overline{i+2}}\right)\right]\right). \tag{A.5}$$

For the double-gyroid phase, we construct the initial ansatz from its space group ($Ia\bar{3}d$) as,

$$\begin{aligned}\phi_{\mathrm{A}}(\boldsymbol{r}) =& \frac{1}{6} + \frac{1}{10}\Bigg\{\sum_{i=0}^{2}\cos\left[q\left(2x_i + x_{\overline{i+1}} + x_{\overline{i+2}}\right)\right] - \cos\left[q\left(-2x_i + x_{\overline{i+1}} + x_{\overline{i+2}}\right)\right] \\ & - \cos\left[q\left(2x_i + x_{\overline{i+1}} - x_{\overline{i+2}}\right)\right] + \cos\left[q\left(2x_i - x_{\overline{i+1}} + x_{\overline{i+2}}\right)\right]\Bigg\}.\end{aligned} \tag{A.6}$$

Appendix B

Pseudo-spectral method

We detail below the procedure to numerically solve the modified diffusion equation,

$$\frac{\partial q(\boldsymbol{r},s)}{\partial s} = \nabla^2 q(\boldsymbol{r},s) - \omega(\boldsymbol{r})q(\boldsymbol{r},s), \quad q(\boldsymbol{r},0) = 1, \tag{B.7}$$

via the pseudo-spectral method [7]. Here, $q(\boldsymbol{r},s)$ is the propagator of interest and $\omega(\boldsymbol{r})$ is a periodic potential.

We begin by assuming that space has been discretized into $M_x \times M_y \times M_z$ points such that the spatial step size in the γ-direction for $\gamma \in \{x, y, z\}$, is given by $\Delta\gamma = L_\gamma/M_\gamma$, where L_γ is the length in the same direction. We further suppose that the contour length N_c is discretized into $M_s + 1$ points, so that the contour step size is given by $\Delta s = N_c/M_s$. The extra contour step is needed so that $s_0 = 0\Delta s = 0$ and $s_{M_s} = M_s\Delta s = N_c$. Under the above assumptions, the propagator at contour step $s_n = n\Delta s$ for $n \in \{0 \le n \le M_s | n \in \mathbb{N}\}$ can now represented by an $M_x \times M_y \times M_z$

array, denoted $\boldsymbol{q}^n$, with elements,

$$\boldsymbol{q}^n_{uvw} = q(\boldsymbol{r}_{uvw}, s_n), \tag{B.8}$$

where $\boldsymbol{r}_{uvw} = (u\Delta x, v\Delta y, w\Delta z)$ for $u \in \{0 \leq u < M_x | u \in \mathbb{N}\}$, $v \in \{0 \leq v < M_y | v \in \mathbb{N}\}$, and $w \in \{0 \leq w < M_z | w \in \mathbb{N}\}$.

From $\boldsymbol{q}^n$, we can obtain the propagator at the next contour step $\boldsymbol{q}^{n+1}$ as follows:

1. We first apply the contribution due to the potential $\omega(\boldsymbol{r})$ to $\boldsymbol{q}^n$ which results in,
$$\boldsymbol{q}^n_{uvw}\Big|^{\frac{1}{3}} = \exp\left(-\omega(\boldsymbol{r}_{uvw})\frac{\Delta s}{2}\right)\boldsymbol{q}^n_{uvw}. \tag{B.9}$$
2. Next, we perform a fast Fourier transform (FFT) to $\boldsymbol{q}^n_{uvw}\Big|^{\frac{1}{3}}$ to obtain its Fourier representation,
$$\hat{\boldsymbol{p}}^n_{uvw}\Big|^{\frac{1}{3}} = \frac{1}{M_x M_y M_z}\sum_{l=0}^{M_x-1}\sum_{m=0}^{M_y-1}\sum_{n=0}^{M_z-1}\boldsymbol{q}^n_{lmn}\Big|^{\frac{1}{3}}\exp\left[-2\pi i\left(\frac{ul}{M_x}+\frac{vm}{M_y}+\frac{wn}{M_z}\right)\right]. \tag{B.10}$$
3. The diffusion contribution, ∇^2, is now accounted for via,
$$\hat{\boldsymbol{p}}^n_{uvw}\Big|^{\frac{2}{3}} = \exp\left[-4\pi^2\Delta s\left(\frac{K_x(u)^2}{M_x^2}+\frac{K_y(v)^2}{M_y^2}+\frac{K_z(w)^2}{M_z^2}\right)\right]\hat{\boldsymbol{p}}^n_{uvw}\Big|^{\frac{1}{3}}, \tag{B.11}$$
where
$$K_\gamma(t) = \begin{cases} t & 0 \leq t < \frac{M_\gamma}{2}+1 \\ M_\gamma - t & \frac{M_\gamma}{2} \leq t < M_\gamma \end{cases}. \tag{B.12}$$
We introduce the function $K_\gamma(t)$ here in order to conform with the standard form used by the FFT package, FFTW3 [93].

4. Next, a backward FFT is performed to $\hat{\boldsymbol{p}}^n_{uvw}\big|^{\frac{2}{3}}$, yielding,

$$\boldsymbol{q}^n_{uvw}\big|^{\frac{2}{3}} = \sum_{l=0}^{M_x-1}\sum_{m=0}^{M_y-1}\sum_{n=0}^{M_z-1} \hat{\boldsymbol{p}}^n_{lmn}\big|^{\frac{2}{3}} \exp\left[+2\pi i\left(\frac{ul}{M_x}+\frac{vm}{M_y}+\frac{wn}{M_z}\right)\right]. \tag{B.13}$$

5. Lastly, we obtain $\boldsymbol{q}^{n+1}$ by applying the potential contribution once more as in Step 1,

$$\boldsymbol{q}^{n+1}_{uvw} = \exp\left(-\omega(\boldsymbol{r}_{uvw})\frac{\Delta s}{2}\right)\boldsymbol{q}^n_{uvw}\big|^{\frac{2}{3}}. \tag{B.14}$$

By applying the potential and diffusion contributions separately as opposed to jointly, we have succeeded in solving $q(\boldsymbol{r}, s)$ to second order accuracy in s, i.e. the associated corrections to $q(\boldsymbol{r}, s)$ are of order $O(\Delta s^3)$ [7].

Appendix C

Simpsons Rule

The numerical integration method employed throughout SCFT calculations is the Simpsons Rule for both even and odd number of intervals [69]. Given $M+1 > 6$ data points, $\{(x_i, y_i = y(x_i))\}_{i=0}^{M}$, assumed to be equally spaced in x, the integration rule reads,

$$\int_{x_0}^{x_M} \mathrm{d}x\, y(x) \approx \Delta x \left(\frac{9}{24} y_0 + \frac{28}{24} y_1 + \frac{23}{24} y_1 + \sum_{i=3}^{M-3} y_i + \frac{23}{24} y_{M-2} + \frac{28}{24} y_{M-1} + \frac{9}{24} y_M \right), \tag{C.15}$$

where $\Delta x = x_i - x_{i-1}$. One small computational advantage offered by Eq. (C.15) over the even Simpsons Rule is that the integration weights are all equal to 1, except for the first and last three points.

When the data is periodic such that $y_M = y(x_M) = y(x_0) = y_0$, Eq. (C.15) can be re-written as,

$$\int_{x_0}^{x_M} \mathrm{d}x\, y(x) \approx \Delta x \left(\frac{18}{24} y_0 + \frac{28}{24} y_1 + \frac{23}{24} y_1 + \sum_{i=3}^{M-2} y_i + \frac{23}{24} y_{M-2} + \frac{28}{24} y_{M-1} \right), \tag{C.16}$$

where it is no longer necessary for y_M to appear on the right-hand side of the above equation since $y_0 = y_M$.

Appendix D

Variable-cell Anderson Mixing

In the following, we discuss our implementation of variable-cell Anderson mixing. This numerical technique was pioneered by Anderson [94]. Schmid first applied Anderson mixing in the context of SCFT in a study of liqid monolayers [95]. The technique was then further developed for polymeric systems by Thompson [96]. Recently, Arora *et al.* extended the usage of Anderson mixing to simultaneously solve the SCFT equations and optimize the lattice parameters, which the authors called variable-cell Anderson-mixing [68]. The benefit offered by Anderson mixing is a faster rate of convergence than the simple mixing scheme introduced in Section 2.1.2 for minimal computational costs, both in terms of memory and number of operations.

Simple mixing uses only the information from the current iteration, the inputs $\{\omega_{\mathrm{A}}(\boldsymbol{r}), \boldsymbol{\theta}\}|_m$ and outputs $\omega_\alpha^{(\mathrm{out})}(\boldsymbol{r})|_m$ to construct the inputs for the next iteration $\{\omega_{\mathrm{A}}(\boldsymbol{r}), \boldsymbol{\theta}\}|_{m+1}$. However, Anderson mixing determines $\{\omega_{\mathrm{A}}(\boldsymbol{r}), \boldsymbol{\theta}\}|_{m+1}$ using an optimal combination of inputs and outputs spanning a number of previous iterations. Thus, when the history of inputs show steady signs of convergence, the convergence process is readily expedited through Anderson mixing. Conversely, when the deviations of the fields from one iteration in the past from the next is large, Anderson mixing performs rather poorly, frequently yielding new inputs that are farther away from the desired solutions than before. For these reasons, simple mixing is often first used to ensure a history of well-behaved input fields for numerical stability, before switching to Anderson mixing for a faster rate of convergence.

Given the inputs $\{\omega_{\mathrm{A}}(\boldsymbol{r}), \boldsymbol{\theta}\}|_{m+1}$ belonging to the m^{th} iteration, the deviation functions or residuals for the auxiliary fields reads,

$$d_\alpha^{(m)} = d\left(\boldsymbol{r}; \omega_\alpha\right)|_m = \omega_\alpha^{(\mathrm{out})}|_m - \omega_\alpha|_m, \tag{D.17}$$

where $\omega_\alpha|_m = \omega_\alpha(\boldsymbol{r})|_m$ and $\omega_\alpha^{(\mathrm{out})}|_m = \omega_\alpha(\boldsymbol{r})|_m$. For the lattice parameters $\boldsymbol{\theta}|_m = \{\theta_p|_m\}_{p=1}^{P}$, the residuals are,

$$d\left(\theta_p\right)^{(m)} = \frac{d}{d\theta_p}\left(\frac{v_0}{V}\beta F\right)\Bigg|_m. \tag{D.18}$$

The auxiliary fields serving as inputs for the next iteration takes the form,

$$\begin{aligned}
\omega_\alpha|_{n+1} =& \Lambda^l \omega_\alpha|_m + (1-\Lambda^l)\omega_\alpha^{(\mathrm{out})}|_m \\
& - \sum_{j=1}^{l} A_j \left[\Lambda^l\left(\omega_\alpha|_m - \omega_\alpha|_{n-j}\right) + (1-\Lambda^l)\left(\omega_\alpha^{(\mathrm{out})}|_m - \omega_\alpha^{(\mathrm{out})}|_{n-j}\right)\right] \\
=& \left(1 - \sum_{j=1}^{l} A_j\right)\left(\omega_\alpha|_m + (1-\Lambda^l) d_\alpha^{(m)}\right) + \sum_{j=1}^{l}\left(\omega_\alpha|_{m-j} + (1-\Lambda^l) d_\alpha^{(m-j)}\right)
\end{aligned}, \tag{D.19}$$

where $l = \min\left(m, M_l\right)$ is the current number, of previous iterations to consider, whereas M_l is the maximum number to consider. The parameter Λ governs the relative contribution of input fields to $\omega_\alpha|_{n+1}$, while A_j are the elements of the vector $\boldsymbol{A}$ that satisfies,

$$\mathbb{U}\boldsymbol{A} = \boldsymbol{D}. \tag{D.20}$$

Here, $\mathbb{U}$ is $l \times l$ symmetric matrix,

$$\begin{aligned}(\mathbb{U})_{jk} =& \sum_\alpha \int d\boldsymbol{r}\ \left(d_\alpha^{(m)} - d_\alpha^{(m-j)}\right)\left(d_\alpha^{(m)} - d_\alpha^{(m-k)}\right) \\ &+ \sum_p^P \left(d\left(\theta_p\right)^{(m)} - d\left(\theta_p\right)^{(m-j)}\right)\left(d\left(\theta_p\right)^{(m)} - d\left(\theta_p\right)^{(m-k)}\right)\end{aligned}, \tag{D.21}$$

and $\boldsymbol{D}$ is a vector of length l,

$$(\boldsymbol{D})_j = \sum_\alpha \int d\boldsymbol{r}\, d_\alpha^{(m)}\left(d_\alpha^{(m)} - d_\alpha^{(m-j)}\right) + \sum_p^P d\left(\theta_p\right)^{(m)}\left(d\left(\theta_p\right)^{(m)} - d\left(\theta_p\right)^{(m-j)}\right), \tag{D.22}$$

with $1 \leq j, k \leq l$. Similarly, the lattice parameters for the next iteration $\boldsymbol{\theta}|_{m+1}$ is given by,

$$\theta_p|_{m+1} = \left(1 - \sum_{j=1}^l A_j\right)\left(\theta_p|_m + (1-\Lambda^l)d_\alpha^{(m)}\right) + \sum_{j=1}^l \left(\theta_p|_{m-j} + (1-\Lambda^l)d_\alpha^{(m-j)}\right). \tag{D.23}$$

We use $\Lambda = 0.9$ and $M_l = 30$ in our implementation of Anderson mixing. Furthermore, $\boldsymbol{A}$ is obtained via LU factorization [97]. We can see from Eq. (2.34) that $\omega_\alpha|_n$ and $\omega_\alpha^{(\text{out})}|_n$ contributes to $\omega_\alpha|_{n+1}$ in an identical manner in every iteration when simple mixing is used. For Anderson mixing however, the contributions of the input and output fields from one particular past iteration to $\omega_\alpha|_{n+1}$ can differ from one iteration to another, being governed by the magnitude of A_j. Thus, Anderson mixing is able to correct for the occasional misbehaved or "bad" step [96], whereas simple mixing cannot.

As noted earlier, when the history of inputs and outputs are poorly behaved, $\mathbb{U}$ may not be invertible, meaning an optimal combination of the inputs/outputs cannot be found. To prevent such a situation, it is recommended that simple mixing is first used until the total deviations or residue errors associated with the auxiliary fields,

$$\Delta\omega_\alpha|_m = \sqrt{\frac{\int d\boldsymbol{r}\ \left(d_\alpha^{(m)}\right)^2}{\int d\boldsymbol{r}\ \left(\omega_\alpha|_m\right)^2}}, \tag{D.24}$$

and associated with the lattice parameters,

$$\Delta\theta_p|_m = \sqrt{\frac{\sum_p^P \left(d\left(\theta_p\right)^{(m)}\right)^2}{\sum_p^P \left(\theta_p|_m\right)^2}}, \tag{D.25}$$

are less than 10^{-2} before Anderson mixing is employed.

Appendix E

Approximation for the Poisson Distribution

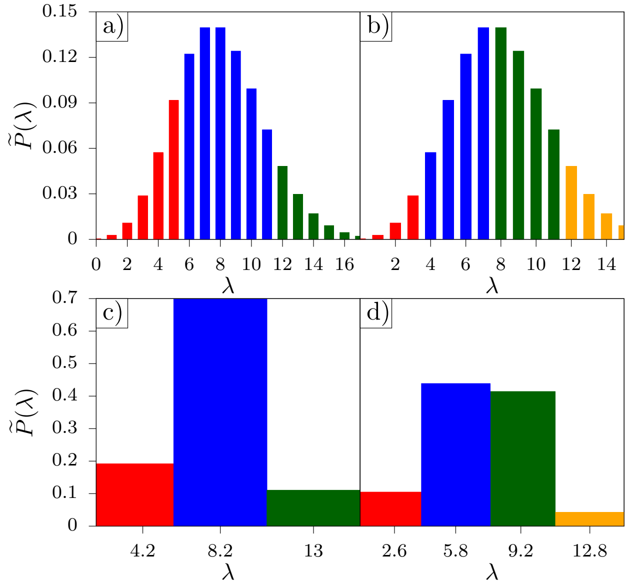

Figure E.1: Approximation of the Poisson distribution a) after the first step (truncation), and c) after the second step (coarse-graining) for $\lambda_0 = 0$, $\lambda_f = 16$, and $M_\lambda = 4$. The same is shown in b), and d) for $\lambda_f = 18$, and $M_\lambda = 3$.

We begin with the Poisson distribution,

$$\mathrm{Pois}\left(\lambda;\mu\right)=\frac{\mu^{\lambda}\mathrm{e}^{-\mu}}{\lambda!},\quad \lambda=0,1,2,... \tag{E.26}$$

which is non-zero for an infinite number of λ values. The goal of our approximation scheme is to construct an approximation that is non-zero for a finite M_λ values of λ. The first step is to choose two values, λ_0, and λ_f, such that the change in $P(\lambda)$ is greater within than outside the interval $[\lambda_0,\lambda_f]$. The choice is arbitrary, subject to the constraint that $\Delta\lambda=(\lambda_f-\lambda_0)/M_\lambda$ is an integer, and simply amounts to truncating the distribution at either ends. The second step is to reduce the $\lambda_f-\lambda_0$ points to M_λ points via coarse-graining:

$$\lambda_i=\frac{\sum_{j=0}^{\Delta\lambda-1}\left(\lambda_0+i\Delta\lambda+j\right)P\left(\lambda_0+i\Delta\lambda+j\right)}{\sum_{j=0}^{\Delta\lambda-1}P\left(\lambda_0+i\Delta\lambda+j\right)}. \tag{E.27}$$

The approximate distribution, which is non-zero for $\lambda=\lambda_i$, is given by,

$$\tilde{P}(\lambda_i)=\frac{\sum_{j=0}^{\Delta\lambda-1}\left(\lambda_0+i\Delta\lambda+j\right)}{\sum_{k=0}^{M_\lambda-1}\sum_{j=0}^{\Delta\lambda-1}P\left(\lambda_0+k\Delta\lambda+j\right)}. \tag{E.28}$$

For our work, we choose $\lambda_0=0$, and $\lambda_f=16$ for $M_\lambda=4$, 8, and 16, while $\lambda_f=18$ for $M_\lambda=3$ to ensure that $\Delta\lambda$ is an integer. This procedure is shown schematically in Figure E.1 for two different degrees of coarse-graining.

Appendix F

Supplementary information for Chapter 4

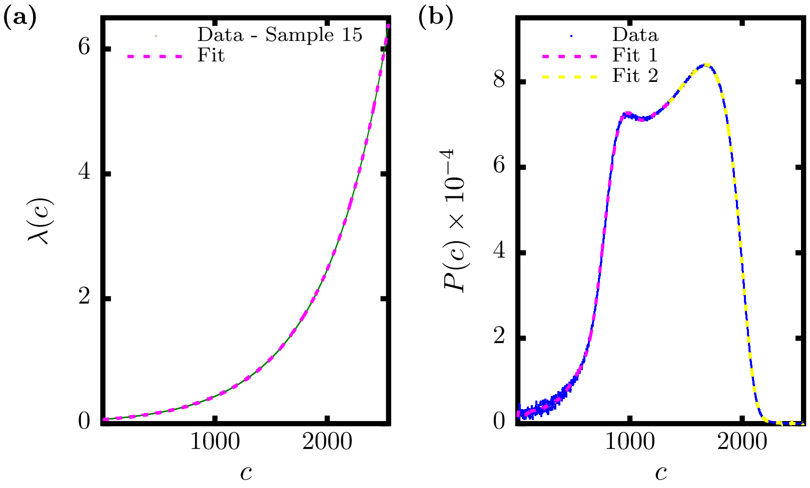

Figure F.2: Polynomial fits for the data of Sample 15: (a) $\lambda\left(c\right)$ using $\left\{c, \lambda_c^{(\mathrm{src})}\right\}_{c=1}^{M^{(\mathrm{src})}}$ and (b) $P^{(\mathrm{src})}\left(c\right)$ using $\left\{c, P_c^{(\mathrm{src})}\right\}_{c=1}^{M^{(\mathrm{src})}}$

Sample 15	$\langle\lambda_c\rangle$	$\langle\lambda_c^2\rangle$	$\langle\lambda_c^3\rangle$
1) Data	1.	1.4263	2.521
2) Integral	0.9997	1.4244	2.5119
3) Quadrature Rule	0.9982	1.4233	2.5163

Table F.1: The first three moments of Sample 15 (1) calculated directly from the data $\left\{\lambda_c^{(\mathrm{src})}, P_c^{(\mathrm{src})}\right\}_{c=1}^{M^{(\mathrm{src})}}$, as well as from integrating the polynomial fits $\lambda(c)^n P(c)$ (2) exactly and (3) using the Gauss-Legendre quadrature.

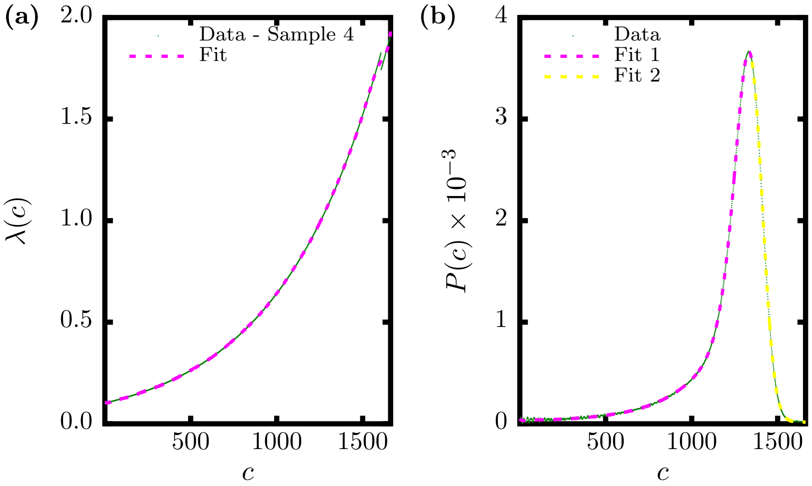

Figure F.3: Polynomial fits for the data of Sample 4: (a) $\lambda(c)$ using $\left\{c, \lambda_c^{(\mathrm{src})}\right\}_{c=1}^{M^{(\mathrm{src})}}$ and (b) $P^{(\mathrm{src})}(c)$ using $\left\{c, P_c^{(\mathrm{src})}\right\}_{c=1}^{M^{(\mathrm{src})}}$

Sample 4	$\langle\lambda_c\rangle$	$\langle\lambda_c^2\rangle$	$\langle\lambda_c^3\rangle$
1) Data	1.	1.085	1.233
2) Integral	1.	1.085	1.233
3) Quadrature Rule	1.003	1.09	1.24

Table F.2: The first three moments of Sample 4 (1) calculated directly from the data $\left\{\lambda_c^{(\mathrm{src})}, P_c^{(\mathrm{src})}\right\}_{c=1}^{M^{(\mathrm{src})}}$, as well as from integrating the polynomial fits $\lambda(c)^n P(c)$ (2) exactly and (3) using the Gauss-Legendre quadrature.

$\lambda_c^{(\mathrm{gl})}$	$P_c^{(\mathrm{gl})}$
8.0416324	9.3171584×10^{-6}
7.1624019	2.9372502×10^{-5}
5.8515582	0.000369386094
4.4270944	0.0059176728
3.13880433	0.0282233699
2.11242293	0.07742264
1.36681614	0.176635128
0.86082552	0.38639963
0.5342314	0.198716017
0.33098385	0.046300866
0.20773068	0.0177815545
0.134298560	0.010000831
0.091108596	0.0078676980
0.066112300	0.0068341697
0.052239564	0.0050164162
0.0455953884	0.00249803124

Table F.3: Relative chain length and corresponding number fractions $\left\{\lambda_c^{(\mathrm{gl})}, P_c^{(\mathrm{gl})}\right\}$ from a 16-point Gauss-Legendre quadrature for Sample 7.

Bibliography

[1] Nan Xie, Weihua Li, Feng Qiu, and An-Chang Shi. σ Phase Formed in Conformationally Asymmetric AB-Type Block Copolymers. *ACS Macro Letters*, 3(9): 906–910, 2014.

[2] Morgan W. Schulze, Ronald M. Lewis III, James H. Lettow, Robert J. Hickey, Timothy M. Gillard, Marc A. Hillmyer, and Frank S. Bates. Conformational Asymmetry and Quasicrystal Approximants in Linear Diblock Copolymers. *Physical Review Letters*, 118(20):207801, 2017.

[3] Ishan Prasad, Youngmi Seo, Lisa M. Hall, and Gregory M. Grason. Intradomain Textures in Block Copolymers: Multizone Alignment and Biaxiality. *Physical Review Letters*, 118(24):247801, 2017.

[4] Dillon T. Gentekos and Brett P. Fors. Molecular Weight Distribution Shape as a Versatile Approach to Tailoring Block Copolymer Phase Behavior. *ACS Macro Letters*, 7(6):677–682, 2018.

[5] Michael Rubinstein and Ralph H. Colby. *Polymer Physics*, volume 23. Oxford University Press New York, 2003.

[6] Mark W. Matsen. The Standard Gaussian Model for Block Copolymer Melts. *Journal of Physics: Condensed Matter*, 14(2):R21, 2001.

[7] Glenn H. Fredrickson. *The Equilibrium Theory of Inhomogeneous Polymers*, volume 134. Oxford University Press on Demand, 2006.

[8] An-Chang Shi. Frustration in Block Copolymer Assemblies. *Journal of Physics: Condensed Matter*, 33(25):253001, 2021.

[9] Christopher A. Tyler and David C. Morse. Orthorhombic *Fddd* Network in Triblock and Diblock Copolymer Melts. *Physical Review Letters*, 94(20):208302, 2005.

[10] Mark W. Matsen and Frank S. Bates. Origins of Complex Self-assembly in Block Copolymers. *Macromolecules*, 29(23):7641–7644, 1996.

[11] Mark W. Matsen and Frank S. Bates. Conformationally Asymmetric Block Copolymers. *Journal of Polymer Science Part B: Polymer Physics*, 35(6):945–952, 1997.

[12] Mark W. Matsen and Frank S. Bates. Block Copolymer Microstructures in the Intermediate-Segregation Regime. *The Journal of Chemical Physics*, 106(6): 2436–2448, 1997.

[13] Sangwoo Lee, Michael J. Bluemle, and Frank S. Bates. Discovery of a Frank-Kasper σ Phase in Sphere-Forming Block Copolymer Melts. *Science*, 330(6002): 349–353, 2010.

[14] Frederick C. Frank and John S. Kasper. Complex Alloy Structures Regarded as

Sphere Packings. I. Definitions and Basic Principles. *Acta Crystallographica*, 11 (3):184–190, 1958.

[15] Frederick C. Frank and John S. Kasper. Complex Alloy Structures Regarded as Sphere Packings. II. Analysis and Classification of Representative Structures. *Acta Crystallographica*, 12(7):483–499, 1959.

[16] Marc De Graef and Michael E. McHenry. *Structure of Materials: An Introduction to Crystallography, Diffraction and Symmetry.* Cambridge University Press, 2012.

[17] Gregory M. Grason. The Packing of Soft Materials: Molecular Asymmetry, Geometric Frustration and Optimal Lattices in Block Copolymer Melts. *Physics Reports*, 433(1):1–64, 2006.

[18] Sangwoo Lee, Chris Leighton, and Frank S. Bates. Sphericity and Symmetry Breaking in the Formation of Frank–Kasper Phases from One Component Materials. *Proceedings of the National Academy of Sciences*, 111(50):17723–17731, 2014.

[19] Nathaniel A. Lynd, Adam J. Meuler, and Marc A. Hillmyer. Polydispersity and Block Copolymer Self-Assembly. *Progress in Polymer Science*, 33(9):875–893, 2008.

[20] Ludwik Leibler and Henri Benoit. Theory of Correlations in Partly Labelled Homopolymer Melts. *Polymer*, 22(2):195–201, 1981.

[21] Kin M. Hong and Jaan Noolandi. The Effect of Polydispersity on the Microphase

Separation of a Block Copolymer System. *Polymer communications (Guildford)*, 25(9):265–268, 1984.

[22] Christian Burger, Wilhelm Ruland, and Alexander N. Semenov. Polydispersity Effects on the Microphase-Separation Transition in Block Copolymers. *Macromolecules*, 23(13):3339–3346, 1990.

[23] Glenn H. Fredrickson and Eugene Helfand. Fluctuation Effects in the Theory of Microphase Separation in Block Copolymers. *The Journal of Chemical Physics*, 87(1):697–705, 1987.

[24] Glenn H. Fredrickson and Scott W. Sides. Theory of Polydisperse Inhomogeneous Polymers. *Macromolecules*, 36(14):5415–5423, 2003.

[25] Scott W. Sides and Glenn H. Fredrickson. Continuous Polydispersity in a Self-Consistent Field Theory for Diblock Copolymers. *The Journal of Chemical Physics*, 121(10):4974–4986, 2004.

[26] David M. Cooke and An-Chang Shi. Effects of Polydispersity on Phase Behavior of Diblock Copolymers. *Macromolecules*, 39(19):6661–6671, 2006.

[27] Mark W. Matsen. Polydispersity-Induced Macrophase Separation in Diblock Copolymer Melts. *Physical Review Letters*, 99(14):148304, 2007.

[28] Mark W. Matsen. Comparison of A-Block Polydispersity Effects on BAB Triblock and AB Diblock Copolymer Melts. *The European Physical Journal E*, 36 (4):1–7, 2013.

[29] Nathaniel A. Lynd, Marc A. Hillmyer, and Mark W. Matsen. Theory of Polydisperse Block Copolymer Melts: Beyond the Schulz-Zimm Distribution. *Macromolecules*, 41(12):4531–4533, 2008.

[30] Frank S. Bates and Mark A. Hartney. Block Copolymers near the Microphase Separation Transition. 3. Small-Angle Neutron Scattering Study of the Homogeneous Melt State. *Macromolecules*, 18(12):2478–2486, 1985.

[31] Keiji Mori, Hideaki Tanaka, Hirokazu Hasegawa, and Takeji Hashimoto. Small-Angle X-ray Scattering from Block Copolymers in Disordered State: 2. Effect of Molecular Weight Distribution. *Polymer*, 30(8):1389–1398, 1989.

[32] Shinichi Sakurai, Keiji Mori, Atsuo Okawara, Kohtaro Kimishima, and Takeji Hashimoto. Evaluation of Segmental Interaction by Small-Angle X-ray Scattering Based on the Random-Phase Approximation for Asymmetric, Polydisperse Triblock Copolymers. *Macromolecules*, 25(10):2679–2691, 1992.

[33] Thomas Wolff, Christian Burger, and Wilhelm Ruland. Synchrotron SAXS study of the Microphase Separation Transition in Diblock Copolymers. *Macromolecules*, 26(7):1707–1711, 1993.

[34] Takeji Hashimoto, Hideaki Tanaka, and Hirokazu Hasegawa. Uniformity of Microdomain Size of Block Polymers as Compared with Uniformity of their Molecular Weights. *Macromolecules*, 18(10):1864–1868, 1985.

[35] Denis Bendejacq, Virginie Ponsinet, Mathieu Joanicot, Yueh-Lin Loo, and Richard Alan Register. Well-Ordered Microdomain Structures in Polydisperse

Poly (styrene)-Poly(acrylic acid) Diblock Copolymers from Controlled Radical Polymerization. *Macromolecules*, 35(17):6645–6649, 2002.

[36] Nathaniel A. Lynd and Marc A. Hillmyer. Influence of Polydispersity on the Self-Assembly of Diblock Copolymers. *Macromolecules*, 38(21):8803–8810, 2005.

[37] Nathaniel A. Lynd, Benjamin D. Hamilton, and Marc A. Hillmyer. The Role of Polydispersity in the Lamellar Mesophase of Model Diblock Copolymers. *Journal of Polymer Science Part B: Polymer Physics*, 45(24):3386–3393, 2007.

[38] Nathaniel A. Lynd and Marc A. Hillmyer. Effects of Polydispersity on the Order-Disorder Transition in Block Copolymer Melts. *Macromolecules*, 40(22):8050–8055, 2007.

[39] Thomas M. Beardsley and Mark W. Matsen. Effects of Polydispersity on the Order-Disorder Transition of Diblock Copolymer Melts. *The European Physical Journal E*, 27(3):323–333, 2008.

[40] Thomas M. Beardsley and Mark W. Matsen. Monte Carlo Phase Diagram for Diblock Copolymer Melts. *The European Physical Journal E*, 32(3):255–264, 2010.

[41] Dillon T. Gentekos, Renee J. Sifri, and Brett P. Fors. Controlling Polymer Properties Through the Shape of the Molecular-Weight Distribution. *Nature Reviews Materials*, 4(12):761–774, 2019.

[42] Dylan J. Walsh, Devin A. Schinski, Robert A. Schneider, and Damien Guironnet. General Route to Design Polymer Molecular Weight Distributions Through Flow Chemistry. *Nature Communications*, 11(1):1–9, 2020.

[43] Dillon T. Gentekos, Junteng Jia, Erika S. Tirado, Katherine P. Barteau, Detlef-M. Smilgies, Robert A. DiStasio Jr, and Brett P. Fors. Exploiting Molecular Weight Distribution Shape to Tune Domain Spacing in Block Copolymer Thin Films. *Journal of the American Chemical Society*, 140(13):4639–4648, 2018.

[44] Vijay K. Rohatgi and AK Md Ehsanes Saleh. *An Introduction to Probability and Statistics*. John Wiley & Sons, 2015.

[45] Yanxiao Sun, Rui Tan, Zhuang Ma, Dongdong Zhou, Jinbin Li, Deyu Kong, and Xue-Hui Dong. Quantify the Contribution of Chain Length Heterogeneity on Block Copolymer Self-Assembly. *Giant*, 4:100037, 2020.

[46] Cheng Zhang, Morgan W. Bates, Zhishuai Geng, Adam E. Levi, Daniel Vigil, Stephanie M. Barbon, Tessa Loman, Kris T. Delaney, Glenn H. Fredrickson, Christopher M. Bates, et al. Rapid Generation of Block Copolymer Libraries using Automated Chromatographic Separation. *Journal of the American Chemical Society*, 142(21):9843–9849, 2020.

[47] Meijiao Liu, Yicheng Qiang, Weihua Li, Feng Qiu, and An-Chang Shi. Stabilizing the Frank-Kasper Phases via Binary Blends of AB Diblock Copolymers. *ACS Macro Letters*, 5(10):1167–1171, 2016.

[48] Guo K. Cheong, Frank S. Bates, and Kevin D. Dorfman. Symmetry Breaking in Particle-Forming Diblock Polymer/Homopolymer Blends. *Proceedings of the National Academy of Sciences*, 117(29):16764–16769, 2020.

[49] Jiayu Xie and An-Chang Shi. Formation of Complex Spherical Packing Phases in Diblock Copolymer/Homopolymer Blends. *Giant*, 5:100043, 2021.

[50] Kyungtae Kim, Akash Arora, Ronald M. Lewis, Meijiao Liu, Weihua Li, An-Chang Shi, Kevin D. Dorfman, and Frank S. Bates. Origins of Low-Symmetry Phases in Asymmetric Diblock Copolymer Melts. *Proceedings of the National Academy of Sciences*, 115(5):847–854, 2018.

[51] Aaron P. Lindsay, Ronald M. Lewis III, Bongjoon Lee, Austin J. Peterson, Timothy P. Lodge, and Frank S. Bates. A15, σ, and a Quasicrystal: Access to Complex Particle Packings via Bidisperse Diblock Copolymer Blends. *ACS Macro Letters*, 9(2):197–203, 2020.

[52] Andreas J. Mueller, Aaron P. Lindsay, Ashish Jayaraman, Timothy P. Lodge, Mahesh K. Mahanthappa, and Frank S. Bates. Emergence of a C15 Laves Phase in Diblock Polymer/Homopolymer Blends. *ACS Macro Letters*, 9(4):576–582, 2020.

[53] Daan Frenkel and Berend Smit. *Understanding Molecular Simulation: From Algorithms to Applications*, volume 1. Elsevier, 2001.

[54] Sam F. Edwards. The Statistical Mechanics of Polymers with Excluded Volume. *Proceedings of the Physical Society*, 85(4):613, 1965.

[55] Eugene Helfand. Theory of Inhomogeneous Polymers: Fundamentals of the Gaussian Random-Walk Model. *The Journal of Chemical Physics*, 62(3):999–1005, 1975.

[56] Ludwik Leibler. Theory of Microphase Separation in Block Copolymers. *Macromolecules*, 13(6):1602–1617, 1980.

[57] Kin M. Hong and Jaan Noolandi. Theory of Inhomogeneous Multicomponent Polymer Systems. *Macromolecules*, 14(3):727–736, 1981.

[58] An-Chang Shi and Jaan Noolandi. Theory of Inhomogeneous Weakly Charged Polyelectrolytes. *Macromolecular Theory and Simulations*, 8:214–229, 1999.

[59] Mark W. Matsen. Gyroid versus Double-Diamond in ABC Triblock Copolymer Melts. *The Journal of Chemical Physics*, 108(2):785–796, 1998.

[60] Samuel J. Dalsin, Thomas G. Rions-Maehren, Marissa D. Beam, Frank S. Bates, Marc A. Hillmyer, and Mark W. Matsen. Bottlebrush Block Polymers: Quantitative Theory and Experiments. *ACS Nano*, 9(12):12233–12245, 2015.

[61] Mark W. Matsen. Effect of Architecture on the Phase Behavior of AB-Type Block Copolymer Melts. *Macromolecules*, 45(4):2161–2165, 2012.

[62] Guojie Zhang, Feng Qiu, Hongdong Zhang, Yuliang Yang, and An-Chang Shi. SCFT Study of Tiling Patterns in ABC Star Terpolymers. *Macromolecules*, 43 (6):2981–2989, 2010.

[63] Meijiao Liu, Weihua Li, Feng Qiu, and An-Chang Shi. Theoretical Study of Phase Behavior of Frustrated ABC Linear Triblock Copolymers. *Macromolecules*, 45 (23):9522–9530, 2012.

[64] Alexander N. Semenov. Contribution to the Theory of Microphase Layering in Block-Copolymer Melts. *Zh. Eksp. Teor. Fiz*, 88(4):1242–1256, 1985.

[65] Hagen Kleinert. *Path Integrals in Quantum Mechanics, Statistics, Polymer Physics, and Financial Markets*. World Scientific, 2009.

[66] Kim Ø.. Rasmussen and George Kalosakas. Improved Numerical Algorithm for Exploring Block Copolymer Mesophases. *Journal of Polymer Science Part B: Polymer Physics*, 40(16):1777–1783, 2002.

[67] G. Tzeremes, Kim Ø. Rasmussen, Turab Lookman, and Avadh Saxena. Efficient Computation of the Structural Phase Behavior of Block Copolymers. *Physical Review E*, 65(4):041806, 2002.

[68] Akash Arora, David C. Morse, Frank S. Bates, and Kevin D. Dorfman. Accelerating Self-Sonsistent Field Theory of Block Polymers in a Variable Unit Cell. *The Journal of Chemical Physics*, 146(24):244902, 2017.

[69] Jock W. Hollingsworth and Henry F. Hunter. Simpson's Rule for an Odd Number of Intervals. In *Preprints of Papers Presented at the 14th National Meeting of the Association for Computing Machinery*, ACM '59, pages 1–2, New York, NY, USA, 1959. ACM.

[70] Yicheng Qiang and Weihua Li. Accelerated Pseudo-Spectral Method of Self-Consistent Field Theory via Crystallographic Fast Fourier Transform. *Macromolecules*, 53(22):9943–9952, 2020.

[71] Mark W. Matsen. Self-Consistent Field Theory for Melts of Low-Molecular-Weight Diblock Copolymer. *Macromolecules*, 45(20):8502–8509, 2012.

[72] So Jung Park, Daeseong Yong, Yeongyoon Kim, and Jaeup U. Kim. Numerical Implementation of Pseudo-Spectral Method in Self-Consistent Mean Field Theory for Discrete Polymer Chains. *The Journal of Chemical Physics*, 150(23): 234901, 2019.

[73] Clare D. McGillem and George R. Cooper. *Continuous and Discrete Signal and System Analysis*. Harcourt School, 1991.

[74] Paul C. Hiemenz and Timothy P. Lodge. *Polymer Chemistry*. CRC Press, 2007.

[75] Milton Abramowitz and Irene A. Stegun. *Handbook of Mathematical Function With Formulas, Graphs and Mathematical Tables*, volume 55. US Government printing office, 1964.

[76] Morgan W. Bates, Joshua Lequieu, Stephanie M. Barbon, Ronald M. Lewis, Kris T. Delaney, Athina Anastasaki, Craig J. Hawker, Glenn H. Fredrickson, and Christopher M. Bates. Stability of the A15 Phase in Diblock Copolymer Melts. *Proceedings of the National Academy of Sciences*, 116(27):13194–13199, 2019.

[77] Damian A. Hajduk, Hiroshi Takenouchi, Marc A. Hillmyer, Frank S. Bates, Martin E. Vigild, and Kristoffer Almdal. Stability of the Perforated Layer (PL) Phase in Diblock Copolymer Melts. *Macromolecules*, 30(13):3788–3795, 1997.

[78] Mark W. Matsen. Effect of Large Degrees of Polydispersity on Strongly Segregated Block Copolymers. *The European Physical Journal E*, 21(3):199–207, 2006.

[79] Scott T. Milner, Thomas A. Witten, and Michael E. Cates. Effects of Polydispersity in the End-Grafted Polymer Brush. *Macromolecules*, 22(2):853–861, 1989.

[80] Mark W. Matsen. Phase Behavior of Block Copolymer/Homopolymer Blends. *Macromolecules*, 28(17):5765–5773, 1995.

[81] Abhiram Reddy, Michael B. Buckley, Akash Arora, Frank S. Bates, Kevin D. Dorfman, and Gregory M. Grason. Stable Frank–Kasper Phases of Self-Assembled, Soft Matter Spheres. *Proceedings of the National Academy of Sciences*, 115(41):10233–10238, 2018.

[82] Yicheng Qiang, Weihua Li, and An-Chang Shi. Stabilizing Phases of Block Copolymers with Gigantic Spheres via Designed Chain Architectures. *ACS Macro Letters*, 9(5):668–673, 2020.

[83] Timothy M. Gillard, Sangwoo Lee, and Frank S. Bates. Dodecagonal Quasicrystalline Order in a Diblock Copolymer Melt. *Proceedings of the National Academy of Sciences*, 113(19):5167–5172, 2016.

[84] Kai Jiang, Jiajun Tong, Pingwen Zhang, and An-Chang Shi. Stability of Two-Dimensional Soft Quasicrystals in Systems with Two Length Scales. *Physical Review E*, 92(4):042159, 2015.

[85] Kai Jiang, Pingwen Zhang, and An-Chang Shi. Stability of Icosahedral Quasicrystals in a Simple Model with Two-Length Scales. *Journal of Physics: Condensed Matter*, 29(12):124003, 2017.

[86] Weihua Li, Feng Qiu, and An-Chang Shi. Emergence and Stability of Helical Superstructures in ABC Triblock Copolymers. *Macromolecules*, 45(1):503–509, 2012.

[87] Mark W. Matsen. Stabilizing New Morphologies by Blending Homopolymer with Block Copolymer. *Physical Review Letters*, 74:4225, 1995.

[88] Francisco J. Martínez-Veracoechea and Fernando A. Escobedo. Monte Carlo Study of the Stabilization of Complex Bicontinuous Phases in Diblock Copolymer Systems. *Macromolecules*, 40(20):7354–7365, 2007.

[89] Francisco J. Martínez-Veracoechea and Fernando A. Escobedo. Bicontinuous Phases in Diblock Copolymer/Homopolymer Blends: Simulation and Self-Consistent Field Theory. *Macromolecules*, 42(5):1775–1784, 2009.

[90] Francisco J. Martínez-Veracoechea and Fernando A. Escobedo. The Plumber's Nightmare Phase in Diblock Copolymer/Homopolymer Blends. A Self-Consistent Field Theory Study. *Macromolecules*, 42(22):9058–9062, 2009.

[91] Poornima Padmanabhan, Francisco J. Martínez-Veracoechea, and Fernando A. Escobedo. Computation of Free Energies of Cubic Bicontinuous Phases for Blends of Diblock Copolymer and Selective Homopolymer. *Macromolecules*, 49 (14):5232–5243, 2016.

[92] Chi To Lai and An-Chang Shi. Binary Blends of Diblock Copolymers: An Effective Route to Novel Bicontinuous Phases. *Macromolecular Theory and Simulations*, 30(3):2100019, 2021.

[93] Matteo Frigo. A Fast Fourier Transform Compiler. In *Proceedings of the 1999 ACM SIGPLAN Conference on Programming Language Design and Implementation*, PLDI '99, Altanta, Georgia, 1999.

[94] Donald G. Anderson. Iterative Procedures for Nonlinear Integral Equations. *Journal of the ACM*, 12(4):547–560, 1965.

[95] Friederike Schmid. Self-Consistent-Field Theories for Complex Fluids. *Journal of Physics: Condensed Matter*, 10(37):8105, 1998.

[96] Russell B. Thompson, Kim Ø. Rasmussen, and Turab Lookman. Improved Convergence in Block Copolymer Self-Consistent Field Theory by Anderson Mixing. *Journal of Chemical Physics*, 120(1):31–34, 2004.

[97] Alex Schwarzenberg-Czerny. On Matrix Factorization and Efficient Least Squares Solution. *Astronomy and Astrophysics Supplement Series*, 110:405, 1995.